An Insight into the Origin of Fluidal Obsidian Pyroclasts from a Basaltic Fissure Eruption, Ascension Island, South Atlantic

ANNABELLE FOSTER

How to cite:

FOSTER, ANNABELLE (2020) An Insight into the Origin of Fluidal Obsidian Pyroclasts from a Basaltic Fissure Eruption, Ascension Island, South Atlantic. Masters thesis, Durham University.

A thesis submitted for the degree of Masters of Science (by research)

An Insight into the Origin of Fluidal Obsidian Pyroclasts from a Basaltic Fissure Eruption, Ascension Island, South Atlantic

Annabelle Foster

Primary Supervisor: Richard Brown

Secondary Supervisors: Katy Chamberlain, Fabian Wadsworth and Kate Dobson

Contents

List of Figures

Abstract

Basaltic eruptions are the most common manifestations of volcanism on Earth. Pyroclast textures can provide insight into the nature of fragmentation, storage and ascent of magma. Progressing our understanding of eruption dynamics by investigating textural, field and geochemical data of pyroclasts will significantly contribute to hazard mitigation models. Unusual, dense obsidian pyroclasts co-erupted with scoria from a small-volume monogenetic fissure eruption on Ascension Island, South Atlantic. The obsidian pyroclasts vary from spherical/sub-spherical glass beads (<1-5 mm in diameter), resembling Pele's tears and spheres, to larger spatter-like bombs (>40 cm in diameter) found within scoria ramparts built up either side of the fissure. They account for <<0.005 vol.% of the total ejected material. Fluidal morphologies imply that the clasts had unusually low melt viscosities on eruption and were therefore capable of flowing upon impact. Field relationships indicate separate magmas underwent no mixing during ascent but agglutinated post-eruption to form an agglomerate of obsidian, scoria and lithic clasts. In-situ quantitative geochemical analyses reveals two distinct magmas; the obsidian is rhyolitic (74 wt.% SiO_2), while the scoria is trachy-andesite (54-58.8 wt.% SiO_2). Magmatic compositions are distinctly bimodal, with clear separation between obsidian and scoria components exemplified in macrocryst species present; the obsidian contains anorthoclase, while the scoria contains a continuum between andesine to labradorite. It also implies that magma mixing did not occur within the crust/conduit. This is comparable in the wider Ascension Island magmatic suite where there is no evidence for magma mixing. The storage, fragmentation and genesis of the obsidian clasts remains unclear. One possibility is that a shallow pocket of degassed rhyolitic magma was intersected by ascending mafic magma in a dike. However, this does not account for the low erupted volume of obsidian clasts and absence of mingling textures. Currently, the preferred hypothesis for their origin is assimilation of water-/gas-poor felsic country rock. Reheating of pre-erupted, felsic country rock to basaltic temperatures would exceed the glass-transition temperature, remobilising glassy clasts, thus invoking highly fluidal textures. Similar pyroclasts elsewhere that co-erupted with basalt have examples of large rhyolitic inclusions which show no evidence of re-melting. Ascension lacks any texturally intermediate clast-type, which highlights the unusual nature of these pyroclasts.

Declaration

I declare that this thesis is my own work and not substantially the same as any which has previously been submitted at this or any other university. The copyright of this thesis rests with the author. No quotation from it should be published without the prior written consent and information derived from it should be acknowledged.

Work for this thesis was supervised under the primary supervision of Dr. Richard Brown.

Annabelle Foster

Durham University

October 2019

Acknowledgements

I would like to thank my supervisors, Rich Brown, Katy Chamberlain, Fabian Wadsworth and Kate Dobson, for their endless support, help and encouragement throughout the year. A huge thank you to Rich Brown for light-hearted, fun discussions, and for consistently asking if I was happy at the end of meetings, which never went unnoticed. Thank you to my family for their words of encouragement, love and support throughout all my decisions. Thank you to my wonderful friends who I met along the way, I have wrinkles under my eyes now from laughing. A special thank you to the inimitable Riona for all the adventures, love and craziness. Last, but certainly not least, thank you to Isaac for limitless love, comfort, fun and especially for cycling 30 minutes in the rain to bring me some dinner during the run up to completion.

Project Aims

This study investigates the formation of unique obsidian pyroclasts erupted during a Late Pleistocene, small-volume fissure eruption on Ascension Island, South Atlantic. I provide the first comprehensive description of these unusual obsidian pyroclasts that were co-erupted with less evolved scoria.

The main objectives of this project are:

- **Objective 1:** To undertake a macroscopic physical and textural qualitative analysis of the pyroclasts.
- **Objective 2:** To undertake a microscopic 2D physical and textural qualitative and quantitative analysis using optical and scanning electron microscopy.
- **Objective 3:** In-situ geochemical analysis of glass and crystal phases.
- **Objective 4:** Use these datasets to comprehensively place constraints on the formation of the obsidian pyroclasts.

The scoria and obsidian pyroclasts appear to represent an end-member behaviour of magma mixing/mingling, although the magmas have co-erupted, they have remained isolated. Using the above outlined analyses, a suite of questions are raised, which include:

1. Why do the obsidian pyroclasts exhibit fluidal textures? Did they exhibit unusually low viscosities upon deposition?
2. Were the eruptive temperatures of the obsidian higher than usual?
3. How were the obsidian pyroclasts entrained into the lava fountain erupting alongside basaltic scoria?
4. Why do the obsidian pyroclasts only account for a small volume of the erupted ejecta?

1 Introduction

Pyroclasts help to dissect subsurface plumbing systems and vent processes which influence the eruptive behaviour. The unique, co-erupted pyroclasts described in this thesis are attributed to basaltic and rhyolitic volcanism, therefore understanding the dynamics of these eruption types, alongside triggers of volcanism, magma fragmentation, role of volatiles and magma mixing helps to constrain their formation and origin. Within this study, the pyroclasts are placed and compared in the context of the volcanism observed on Ascension Island.

1.1 Ascension Island

Ascension Island (7° 56'; 14° 22') is a $\leq$7 million year old (Myr) ocean island volcano which lies on $\sim$ 7 Myr oceanic crust (Klingelhöfer et al., 2001; Paulick et al., 2010). It is located 90 km west of the Mid Atlantic Ridge (MAR) and 50 km south of the Ascension Fracture Zone (AFZ), one of a number of oceanic islands in the South Atlantic Ocean (figure 1a) (Chamberlain et al., 2016; Preece et al., 2018). Ascension Island covers 98 km^2 and is entirely volcanic in origin, with the exception of sedimentary deposits on beaches (figure 1b). There is no historical record of volcanic activity on Ascension Island. Desert climates leads to no soil or vegetation development, preserving original surface flow features of lava, which gives the deposits a youthful appearance and led to hypothesise that the island should be considered as active (Daly, 1925; Atkins et al., 1964; Preece et al., 2018). The youngest eruption on Ascension Island is dated to 0.51 ± 0.18 ka (Preece et al., 2018) using ^{40}Ar/^{39}Ar dating.

Research into the origin of the magmatism on Ascension Island has been focused on its relationship to an undefined mantle anomaly, and its proximity to the MAR due to its ocean island basalt (OIB) affinity (Chamberlain et al., 2019). The OIB-like trace element data led to the inference that magmatism is the product of a shallow mantle plume which has been diverted along the AFZ (Harris, 1983; Weaver et al., 1996). However, seismic evidence suggests that Ascensions crustal structure cannot be related with a hot spot origin (Klingelhöfer et al., 2001) despite erupting a wide range of compositions (Daly, 1925; Weaver et al., 1996; Kar et al., 1998; Jicha et al., 2013; Chamberlain et al.,

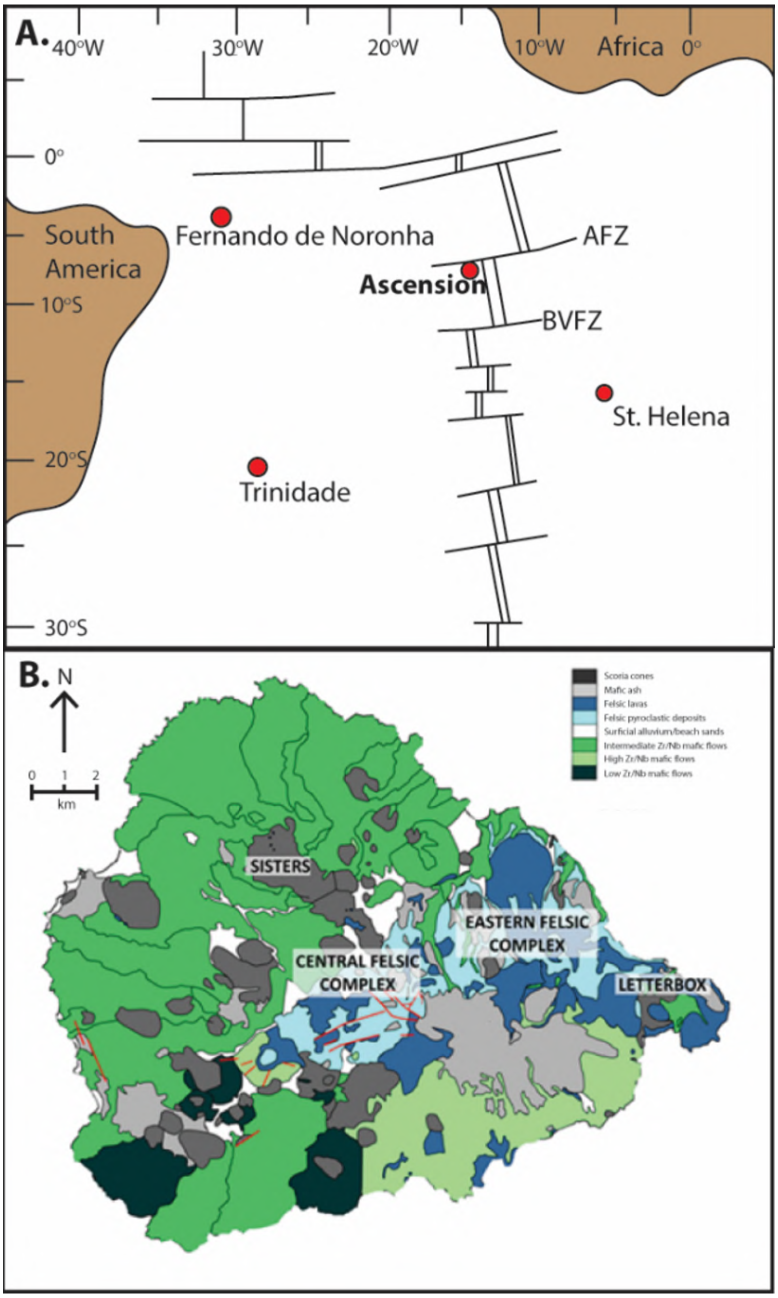

Figure 1: Modified from Chamberlain et al., (2016); Paulick et al., (2010); Weaver et al., (1996). (A) Location map of Ascension Island in relation to the Mid Atlantic Ridge (MAR) and the Ascension Fracture Zone (AFZ) and Bode Verde Zone (BVFZ). (B) Geological map of Ascension Island, showing a felsic centre (Central Felsic Complex) surrounded by mafic volcanic rocks. Faults are marked as red lines.

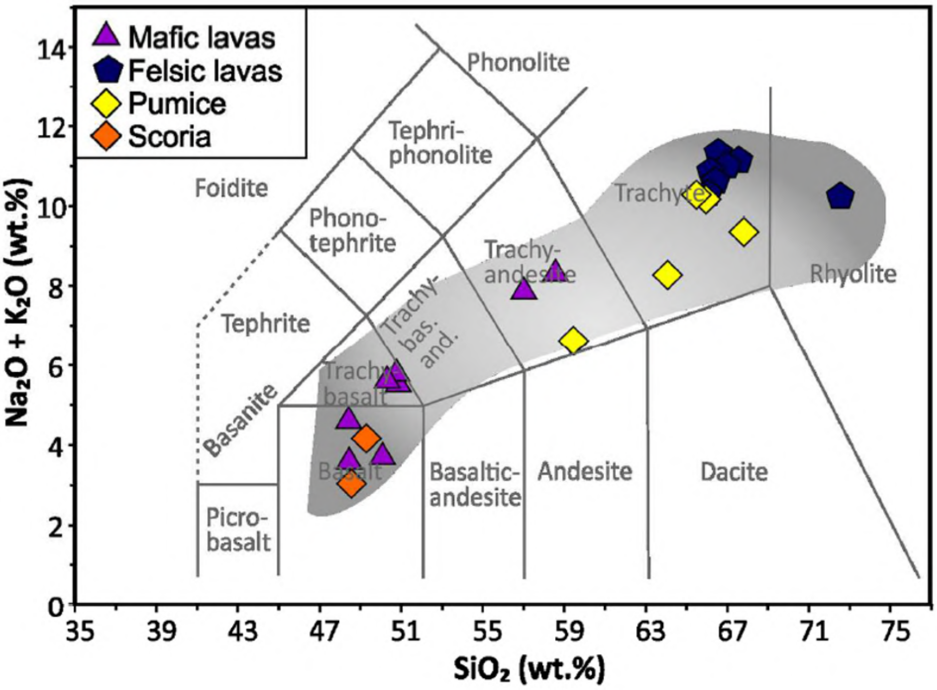

Figure 2: Total alkali vs. silica plot of whole rock data from Ascension samples compared to all known Ascension whole rock compositions represented by grey field (data from Weaver et al., 1996, Kar et al., 1998, Jicha et al., 2013). Taken from Chamberlain et al., (2019).

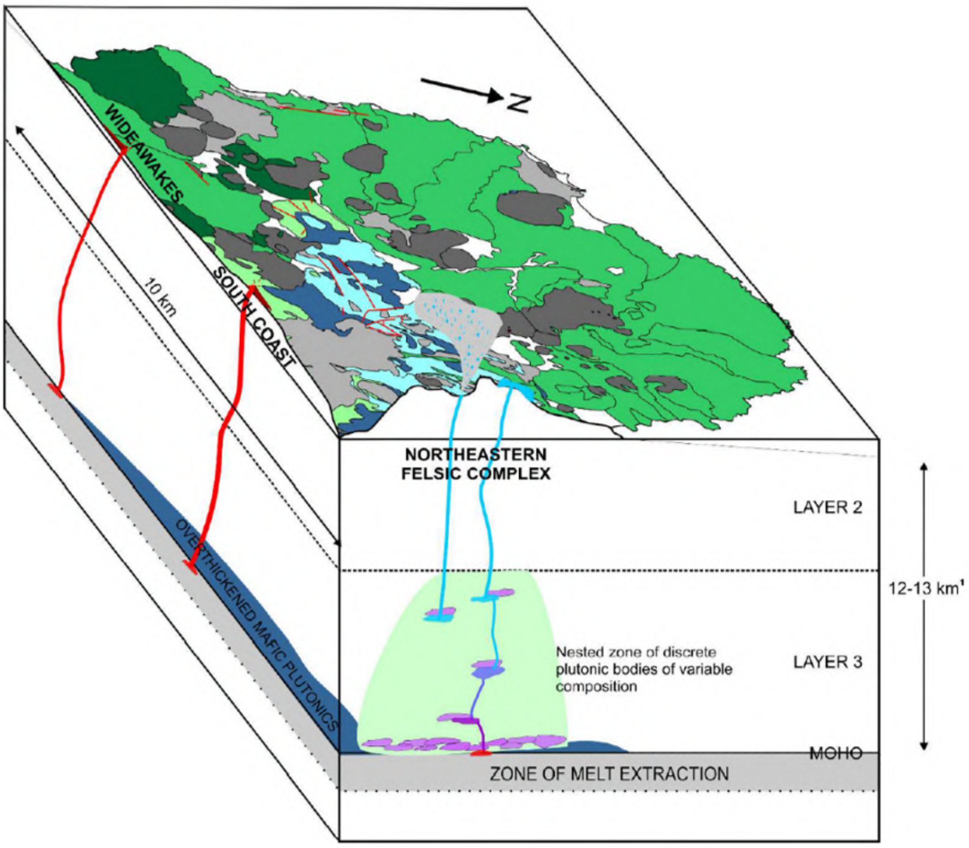

Figure 3: Schematic magma plumbing system model for Ascension Island by Chamberlain et al., (2019). The model shows the geographical distinction between the mafic and felsic products in relation to their magmatic sources. Mafic plutons are blue, felsic plutons are purple and green.

2019). Additionally, topographic seismic studies failed to find evidence for magmatic underplating beneath the Island, further suggesting no hot spot origin, therefore the origins of Ascension Island remain not fully resolved.

Felsic volcanic products are suggested to be derived from the fractional crystallisation of the high Zr/Nb basalt (Weaver et al., 1996; Kar et al., 1998) due to limited field evidence for mixing between the magma batches (Kar et al., 1998; Chamberlain et al., 2016). This is further supported by whole rock major and trace element data of crystals and glass from mafic and felsic pyroclastic and effusive deposits, which span an entire range of eruptive ages and compositions (figure 2) and show that fractional crystallisation is the main driver for the production of felsic melt (Chamberlain et al., 2019). This suggests that magma storage regions in the lower crust is transient and material is not recycled (Chamberlain et al., 2019).

Basaltic magmas have been categorised into three distinct groups according to Zr/Nb rations (Weaver et al., 1996; Kar, 1997) that result from varying degrees of partial melting of a consistent source or products of different mantle regions with varying compositions (Weaver et al., 1996; Kar, 1997; Jicha et al., 2013). However, the variations in Ti, Ta and Nb in isotopic data seems unlikely to be the result of fractional crystallisation. Instead, varying degrees of partial melting or differing magma source compositions are more credible (Jicha et al., 2013).

Ascension Islands' origin and plumbing system remain somewhat ambiguous, despite its volcanic products being widely studied (Weis, 1983; Weaver et al., 1996; Harris et al., 1983; Kar et al., 1998; Paulick et al., 2010; Chamberlain et al., 2019). Sr and Nd data show minimal variations between the submarine and subaerial erupted products, (Weaver et al., 1996; Kar, 1997; Paulick et al., 2010). Hf isotopic data shows distinct characteristics of the subaerial products, suggesting that the mantle source supply for the submarine volcanism is no longer available (Paulick et al., 2010; Chamberlain et al., 2016). Across the island, there is no evidence for magma mixing in the volcanic deposits, suggesting felsic melts bypass any mafic sources, resulting in a spatial control on the evolution of the felsic melts. This is shown in a recent model (figure 3), where the localised sectors of the felsic complexes are fed by discrete plutonic bodies of varying composition (Chamberlain et al., 2019).

A simplified chronology of the island divides the volcanic activity of the island into an earlier felsic stage and a later mafic stage (Harris 1983). Subaerial volcanism has occurred for the last ∼1 Mya, erupting lavas of a silica-undersaturated, subalkaline evolutionary series: olivine basalt - hawaiite - mugearite - benmoreite - trachyte - rhyolite (figure 2) (Daly, 1925; Weaver et al., 1996; Jicha et al., 2013; Preece et al., 2018). This portion only represents 1% vol. of the 3800 km^3 edifice (Harris, 1983). Mafic lavas and scoria cones dominate the north, west and south of the Island, these are basaltic to benmoreite lavas associated with intermediate Zr/Nb magma type which are inferred as the most recent volcanic activity, but also date back to 705 ka (Jicha et al., 2013). The oldest mafic lava flows yield ^{40}Ar/^{39}Ar ages of 791-705 ka. The volcanic rocks resulted from a range of volcanic activity, including Hawaiian, Strombolian, Vulcanian, Plinian, and Phreatomagmatic eruption-styles (Chamberlain et al., 2019). Trachyte and rhyolite lava flows, domes and pyroclastic deposits are the oldest dated volcanic products and are concentrated in two areas: Central Felsic Complex including Green Mountain, Middleton Ridge and the Eastern Felsic Complex (Nielson and Sibbett, 1996; Kar et al., 1998; Chamberlain et al., 2016). Lavas from the Eastern Felsic Complex are 517 to 52 ka old (Jicha et al., 2013), and thus the youngest felsic products. The Middleton Ridge Complex is the oldest of the felsic lavas, which obtained an age of 1094 ka, using ^{40}Ar/^{39}Ar dating (Jicha et al., 2013).

1.2 Triggers for volcanic eruptions

Magmatic eruptions are primarily driven by the expansion of dissolved volatiles (Valentine and Gregg, 2008; Valentine and Connor, 2015). As the magma ascends in the conduit, volatiles become less soluble and therefore exsolve, forming bubbles that grow through a combination of decompression and coalescence (Valentine and Connor, 2015). Additional internal factors which influence eruptions (highlighted in figure 4) include magma production rate, density buoyancy, magma composition, volatile contents and viscosity (Cassity et al., 2018). An increase in the production of magma into a reservoir can promote heating, vesiculation and convection, mobilising crystal-rich magmas. The injection of magma will also increase the volume within the chamber, increasing magma overpressure of the system. In some cases, the injections of new magma can a produce effusive eruptions by decreasing the viscosity (Ruprecht and Bachmann, 2010) of the magma and reducing water content (Cassidy et al., 2016).

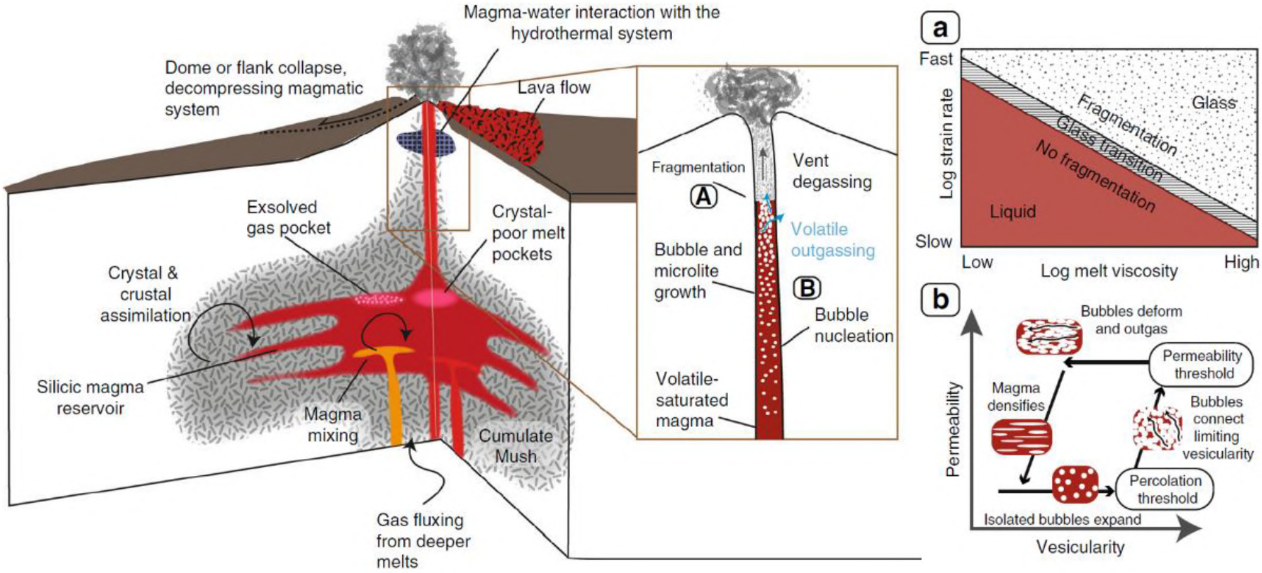

Figure 4: Schematic diagram summarising the range of processes which influence the eruptive style from the magma chamber to surface. Taken from Cassidy et al., (2018). (A) Fragmentation is a function of the melt viscosity and strain rates. At slow strain rates there is no fragmentation and the melt behaves as a liquid. At fast strain rates, brittle fragmentation occurs as it transitions through a glass phase for a given viscosity. (B) Cycle of outgassing; bubbles nucleate as pressures decrease, they coalesce and form a permeable network through which gas can move freely (Cashman and Sparks, 2013).

1.2.1 Role of volatiles

Magma is a mobile mixture which generally consists of solid (crystals), liquid (melt) and gaseous (volatiles) phases (Best, 2013). At high pressures, volatiles are dissolved in the melt. The most abundant volatiles are H_2O, CO_2, S, Cl and F, however H_2O is the most dominant and has the greatest effect on eruption dynamics (Cashman, 2004). Solubility refers to the maximum quantity of a volatile or component that can be dissolved within a set of conditions (pressure, temperature and composition) (Wallace et al., 2015). The H_2O solubility is greater in rhyolitic melts than in basaltic melts, however this difference is mostly due to the temperature differences rather than compositional effects (figure 5) (Burgisser and Degruyter 2015).

In a rhyolitic melt, bubble growth increases with temperature and initial total H_2O (Liu and Zhang, 2000). Water occurs in two different species; OH^- groups and H_2O molecules. The proportions of these vary systemically with the total water concentration. If the total dissolved water concentrations are low, almost all the water is present as OH^- groups. Further speciation is dependent on temperature and quench rate of a magma, forming the basis of a geospeedometer, from which cooling rates of hydrous rhyolitic glasses can be calculated using measurements of OH^- groups and H_2O molecules (Burgisser and Degruyter 2015). As magma ascends, certain gas species are no longer soluble and exsolve to form bubbles, which are present as vesicles in pyroclasts (Browne and Szramek., 2015). Crystallisation during cooling and decompression during ascent induces exsolution of volatiles from initially undersaturated melts (Best, 2013). Degassing can transform the magma into a foam as bubbles accumulate, and can promote crystal growth, resulting in a viscosity increase. Typically, a higher crystal fraction results in higher viscosities (Paritt and Wilson, 2009). The expansion of volatiles near the surface of a conduit provides the driving force for volcanic eruptions (Wallace et al., 2015). Magmas that are mostly degassed erupt effusively, oozing from the vent if the gas is able to escape from interconnected bubbles in a foamy magma (Eichelberger et al., 1986). The rate at which gas is lost is dependent on the permeability, melt viscosity and differential stress of the foam. Outgassing is open-system degassing of volatiles in a conduit, where the gas phase is segregated from a magma (Burgisser and Degruyter 2015). It occurs due to (1) buoyant bubble rise, (2) development of a permeable network (Eichelberger et al., 1986; Westrich and Eichelberger, 1994) and/or (3) fragmentation through fractures (Stasiuk et al., 1996; Tuffen et al., 2003) (figure 4b). Gas can dissolve back into the melt and the bubbles disappear if the magma undergoes a significant amount of pressure increase (Wallace et al., 2015).

In higher viscosity magmas, such as rhyolites, bubbles do no move relative to each other and coalescence occurs because of rupture of the melt films (Burgisser and Degruyter 2015). The nucleation of bubbles may be either heterogeneous or homogeneous (Cashman, 2004). Homogeneous nucleation is where a magma is devoid of crystals and bubbles grow in a pure melt, whereas heterogeneous is the nucleation of bubbles on the sides of crystals (a tendency depending on the mineral species and surface tension). Nucleation of bubbles controls bubble number density, growth changes, bubble size and magma vesicularity (Cashman, 2004).

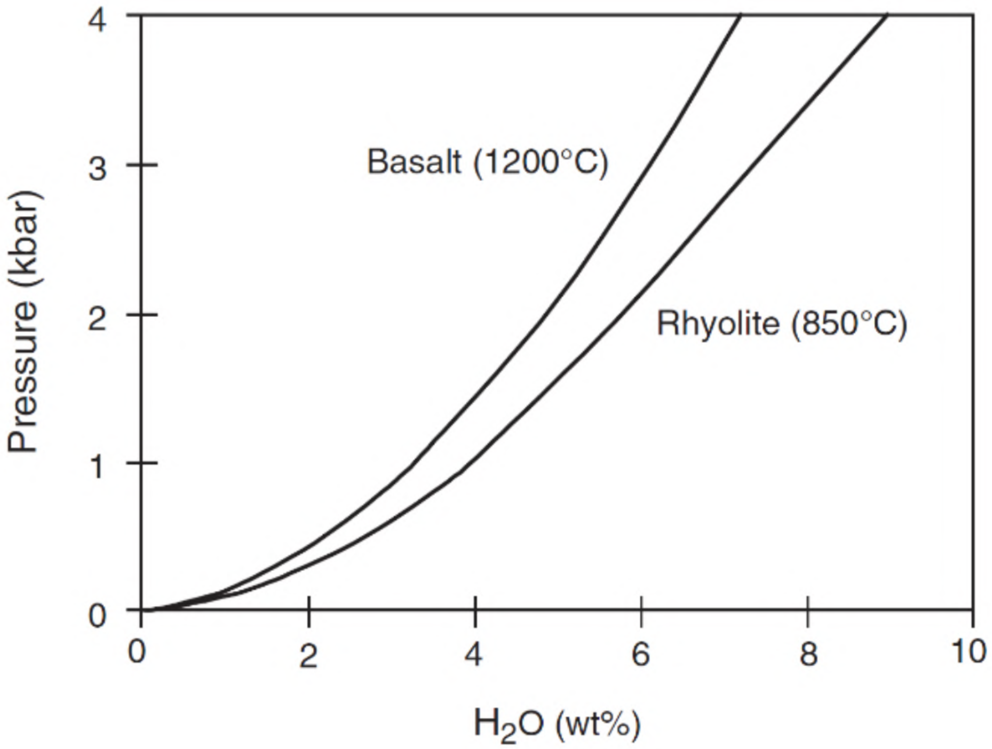

Figure 5: H_2O solubility in basalt and rhyolite at typical magmatic temperatures. Pre-eruptive H_2O concentrations in rhyolites are often relatively high and remarkably similar to basalts. Taken from Wallace et al., (2015); Baker and Alletti, (2014).

1.2.2 Magma viscosity

The viscosity of magma is controlled by a number of interconnected factors, which include: silica content (hence composition), temperature, crystal content, and gas bubble content (Parfitt and Wilson, 2009). Due to these parameters, the viscosity of silicate magmas can range from 10^{-1} to 10^{14} Pa.s (15 orders of magnitude) (Giordano et al., 2015). High silica content and low temperatures result in a magma with higher viscosities (figure 6). Viscosity is also a function of the volume fraction of crystals, and to a lesser extent, the size and shape of crystals. Gas bubbles can increase the viscosity of a magma, depending on the shear rates. A high silica magma with a high bubble fraction (which has the aforementioned characteristics leading to high viscosities) will have low shear rates, ultimately increasing the viscosity futher (Parfitt and Wilson, 2009).

A small amount of water (a few wt.%) can have dramatic effects on lowering the viscosity of silicate liquids (figure 7) as water is composed of 89% oxygen (by mass) (Lesher and Spera, 2015). Although these effects can also be seen in more mafic composition, it is not as significant as fewer bridging oxygen molecules exist in anhydrous, mafic melts (Lesher and Spera, 2015). These effects are important in volcanology as they can determine eruptive behaviour (Dingwell, 1996; Papale, 1999; Giorando et al., 2008).

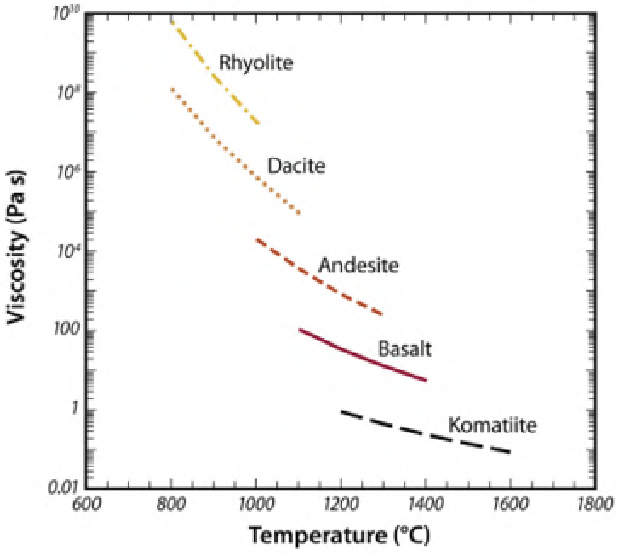

Figure 6: Viscosities of common magmatic compositions as a function of temperature. The viscosity for more evolved, silica-rich magmas is typically higher. Taken from Lesher and Spera (2015), reproduced from Spera (2000).

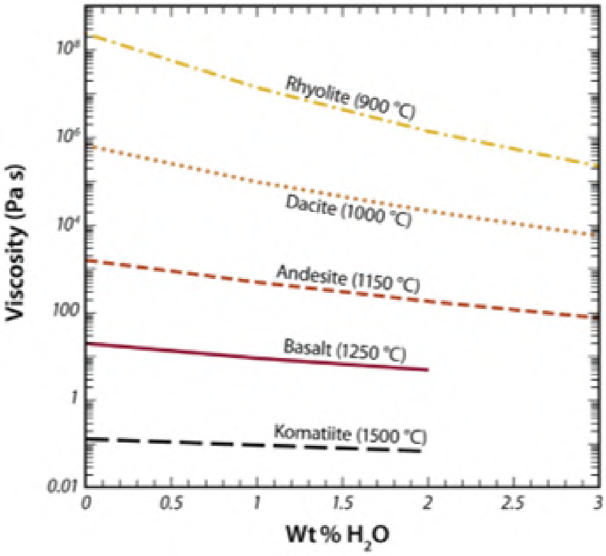

Figure 7: Viscosities of common magmatic compositions as a function of water concentrations. The graph shows that water concentrations within a silicic magma has a more significant impact on the viscosity than mafic compositions. Taken from Lesher and Spera (2015).

1.2.3 Fragmentation of magma

The fragmentation of magma transforms magma from a liquid phase with dispersed gas bubbles (and/or crystals) to a gas phase with dispersed magma fragments (pyroclasts). Processes that cause magma to fragment start deep within the volcanic system, at pressures of typically 100-200 MPa where volatiles are dissolved (Cashman and Scheu, 2015).

Primary fragmentation occurs due to (1) rapidly ascending magma during explosive eruptions, (2) rapid decompression caused by collapse of volcanic edifices or lava domes, (3) shearing of magma at the conduit walls, or (4) by impact-induced explosion of hot solid blocks during dome collapse. Secondary fragmentation can occur by shearing and extension of fluids, or collision and abrasion of solids (Cashman and Scheu, 2015). Secondary fragmentation of primary pyroclasts reduces the particle size of the pyroclasts during transport within the conduit and after pyroclast ejection from the vent. Fragmentation by rapid acceleration occurs the bottom-up of the conduit, where bubbles rapidly grow during decompression. A reduction in the viscosity can alter the nature of fragmentation, inhibiting brittle failure and promoting non-explosive loss of volatiles (Cassidy et al., 2018). Fragmentation by rapid decompression operates from top-down, when bubbly magma is suddenly exposed to a lower pressure; fragmentation is usually brittle (Cashman and Scheu, 2015).

Physical characteristics of the eruptive products provide details of both fragmentation and post-fragmentation evolution. Large erupted pyroclasts can continue to expand after fragmentation. Mafic bombs often have highly inflated interiors and dense, poorly vesiculated outer rims that indicate rapid quenching of the exterior. In mafic eruptions where expansion is rapid and the melt viscosities are low, the outer surface may be smooth and very thin. In silicic eruptions, where the expansion is slower, the outer rind is commonly thick and fractured to form 'breadcrust' patterns. In Hawaiian high fountaining, post-fragmentation expansion can produce highly porous, vesiculated pyroclasts termed 'reticulite'. During these same eruptions, relatively dense pyroclasts (30% vesicles) can form as droplets that slow limited expansion (Cashman and Scheu, 2015).

1.3 Basaltic volcanism

Basaltic eruptions are the most common volcanic manifestations found on Earth, occurring in all geodynamic and volcanological settings; monogentic centres (scoria cones within volcanic fields), large shield or stratovolcanoes and caldera complexes (Sigurdsson, 2000; Valentine and Gregg, 2008; Taddeucci et al., 2015). Basaltic volcanoes can be effusive eruptions with a total erupted volume of typically <1 km^3 (Valentine and Connor, 2015) or explosive, which is largely limited to Hawaiian and Strombolian activity, although Plinian basaltic eruptions have been recorded (Walker et al., 1984; Coltelli et al., 1998; Houghton et al., 2004; Sable et al., 2006; Wehrmann et al., 2006).

1.3.1 Hawaiian and Strombolian eruptions

Hawaiian and Strombolian eruptions characteristically produce low viscosity (10-10^4 Pa.s), silica-poor magmas (basaltic to basaltic-andesite) and erupt at high temperatures of 1000°C to 1200°C (Taddeucci et al., 2015). Ejected pyroclasts erupted from Hawaiian-style explosions are a result of sustained jets, where the material is episodically transported by ballistic trajectories. This distinctive fountain of erupted material can reach elevations of hundreds of metres within the duration of an eruption (hours to days) (Taddeucci, 2015).

Hawaiian fountaining is typically associated with fissure eruptions, where magma has ponded to, or above, the level of the vent (Head and Wilson, 1989). Fountains consist of a hot, incandescent inner portion where the fluid magma flux is greatest, which is surrounded by a dull red/brown (or non-incandescent) portion (Head and Wilson, 1989; Sumner et al., 2005). The start and end of high fountaining can exhibit transitional behaviour to more Strombolian-style activity (Taddeucci et al., 2015). Strombolian eruptions are weak, short-lived explosions resulting from the fragmentation of magma as pressurised gas pockets are released at the free surface of an open vent or lava lake (Taddeucci et al., 2015). If magma ascends relatively slowly, bubbles are able to coalesce and form gas-rich slugs that drive Strombolian eruptions (Valentine and Connor, 2015). Rapid ascent of magma preludes bubble coalescence and can produce sustained jets or lapilli and ash, which are considered as violent Strombolian eruptions (Valentine and Connor, 2015). The explosive bursts are, on average, at velocities between 50-100 ms^{-1} for volcanic bombs but smaller sized pyroclasts and ash can exceed 400 ms^{-1}. Molten magma clots and lithic debris from the vent are ejected into jets typically only reaching a few hundred meters in height (Patrick et al., 2007; Taddeucci et al., 2015). Volcanic eruptions can commonly show characteristics of both Hawaiian and Strombolian behaviour, transitioning from each style at the beginning or end of an eruptive episode (Taddeucci et al., 2015).

Eruptions of basaltic magma produce pyroclasts that vary in shape, size, vesicularity and temperature. Hawaiian fountaining produces a range of pyroclasts defined by the degree of cooling that they undergo in the fire-fountain and their position within the fountain. (Head and Wilson, 1989; Sumner et al., 2005). Pyroclasts range from brittle scoria, spindle bombs and ash to fluidal clasts; breadcrust bombs, poorly-welded cowpat bombs, spatter and Pele's hair and tears. Bombs and spatter are commonly found in proximal settings, displaying fluidal shapes and some degree of agglutination of multiple bombs (Taddeucci et al., 2015). Hawaiian and Strombolian volcanic activity produce relatively coarse, well-sorted and locally dispersed deposits relative to all other pyroclastic deposits. If the vent is elongate, in the case of fissures, the pyroclasts result in the build of spatter and scoria ramparts (Valentine and Connor, 2015). Pyroclasts are usually 10^{-2} to 10^{-1} m in size but can range from 10^{-6} to 100 m (Taddeceui et al., 2015).

Scoria is the most common pyroclast, and shows a moderately vesicular texture (millimetre to centimetre-sized vesicles) which is often glassy. Scoria and rigid bombs that are typically too cold to agglutinate on deposition are generally products from the outer parts of a fountain, but they may adhere if their fluid interior bursts upon impact. As the inner part of a fountain can retain heat, entrained clasts do not typically develop a chilled, brittle rind (Sumner et al., 2005). Viscosity is a key factor in a range of mechanisms that produce pyroclasts during Hawaiian eruptions (Sumner et al., 2005). Low viscosities promote compactional welding and joining clasts together by point contacts.

Spatter is a common pyroclastic product of Hawaiian fountaining, which forms vent-proximal cones or ramparts (figure 8) (Jones et al., 2018; Head and Wilson, 1989; Sumner, 1998; Sumner et al., 2005). Spatter is an accumulation of originally hot, fluid pyroclasts, which agglutinate upon landing (Sumner et al., 2005) as they primarily remain above the glass transition temperature (Jones et al., 2018) Low viscosity spatter is flattened by the agglutination of clasts as they adhere and accumulate as the hot fluid gradually cools (Sumner et al., 2005). The least viscous pyroclasts form fluidal droplets form a homogeneous liquid in which the remnant particles outlines are obliterated.

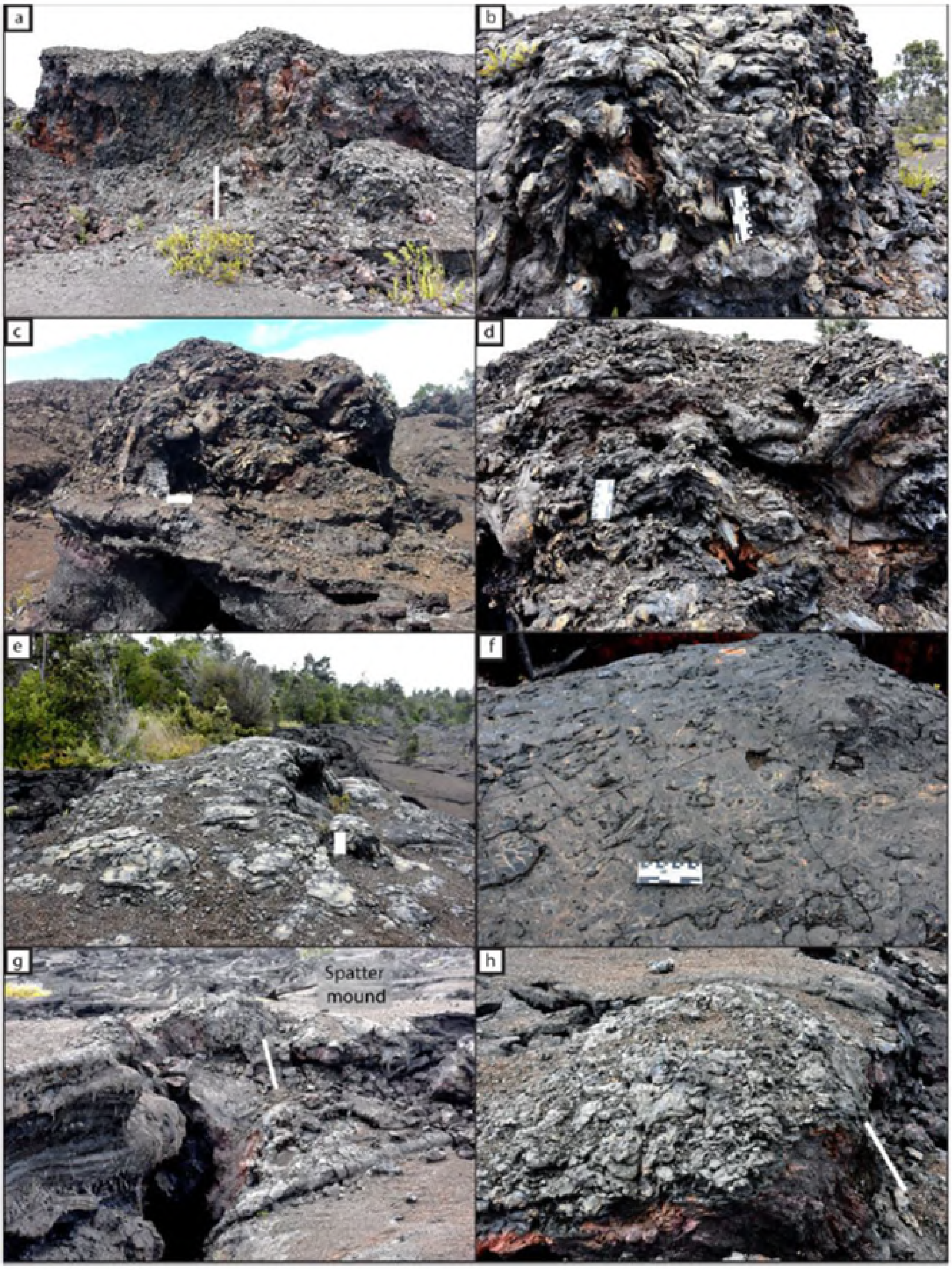

Figure 8: Field photographs of spatter found as ramparts (A-D) and mounds (E-H). Scales measure 16 cm for all images, except in a, g and h where the scale is 1.2 m. Taken from Jones et al., (2018).

Pele's hair is an unusual, delicate type of pyroclast with highly elongate and intricate morphologies, commonly associated with subaerial explosive activity of low viscosity basaltic magma (Heiken and Wohletz, 1985). They also occur in conjunction with passive outgassing of lava lakes, littoral explosions, Strombolian activity and submarine activity (Cannata et al., 2019). Pele's tears are glassy, fluidal, tear-drop shapes (figure 9) with a smooth exterior and vesiculated interior (Porritt et al., 2012). Peles hair, tears and spheres are hypothesised to be a result of the primary fragmentation, or disruption, of magma ponding at the surface of a vent (Porritt et al., 2012). Experiments by Shi-mozuru (1994) led to the suggestion that Pele's hairs are produced when the spurting velocity of erupting magmas is high and Pele's tears when it is relatively low. The morphology of Pele's tears is a result of surface tension, air friction and acceleration of the droplet after eruption (Heiken, 1972). The size of the droplet also influences their shape; as Pele's tears decrease in size (∼1-2 mm), they tend towards spheres and lose their elongate pendant (figure 9). Their shape and internal bubble density is highly dependent on surface tension (Porritt et al., 2012). Further, the cooling rate of the droplet must be rapid enough to form but not slow enough to promote further vesiculation (Porritt et al., 2012).

Figure 9: Photograph taken from Cashman and Scheu (2015). Exhibits the variations of the external morphologies of Pele's tears and spheres. The shapes trend from a near perfect sphere to tears with streamlined pendants.

1.4 Rhyolitic volcanism

Rhyolitic volcanism is associated with some of the most explosive eruptions on Earth. It occurs in a range of tectonic settings such as arc and intraplate settings (Wallace et al., 2015) and in some cases Mid-Ocean-Ridges (e.g. Iceland and Ascension Island) (Wallace et al., 2015). Rhyolitic volcanism is highly silicic (70-75 wt.% SiO_2), cooler (700-1000°C) and gas-rich (Lesher and Spera, 2015). Rhyolitic eruptions are significantly less common than basaltic eruptions, with less than a cubic kilometer of rhyolitic magma erupted annually, despite a significant amount being stored within the crust (Lesher and Spera, 2015). A significant amount of volatiles can remain in rhyolitic melts even at moderate pressures, which are released during explosive eruptions (Schmincke, 2004). Silicic magmas typically have high pre-eruptive H_2O concentrations ranging from 4-6 wt.% (Wallace et al., 2015). This pre-eruptive range is remarkably similar to the eruptive viscosities of basaltic magma , however as rhyolites ascent, they degas as the water forms bubbles and the melt can become very viscous (10^6-10^{11} Pa.s) (Schmincke, 2004). Silicic eruptions are primarily characterised by abundant fine ash and variable amounts and sizes of larger pumice clasts, which are typically highly vesicular.

1.4.1 The glass transition temperature

The glass transition (Tg) is the relaxation temperature range of glass that represents a kinetic barrier, separating the behaviour of silicate melts into two states; (1) viscous liquid and (2) brittle glass (from liquid- to solid-like behaviour) (Dingwell, 1998; Gottsmann and Dingwell, 2001a; Cashman and Scheu, 2015). The transition between the behaviours of silicate melt can play an important role in volcanic eruptions (Dingwell and Webb; 1990; Dingwell, 1996; Papale, 1999). The Tg depends upon magma composition (including volatile content) and cooling rate. The Tg is sensitive to small variations in H_2O and SiO_2 content of the melt (figure 10), emphasising the role of crystallisation and degassing during a magmas ascent and eruption. During the formation of volcanic glass, the Tg may be crossed several times. The first crossing may correspond to primary fragmentation in explosive volcanism (Dingwell, 1996).

Silicate liquids well above the Tg behave as Newtonian fluids (linear relationship between shear rate and shear stress at fixed temperatures and pressures). However this is not the case for magmatic multiphase liquids (contain bubbles and crystals) such as natural glasses, which are described as visco-elastic materials (Lesher and Spera, 2015) and mostly behave as non-Newtonian fluids.

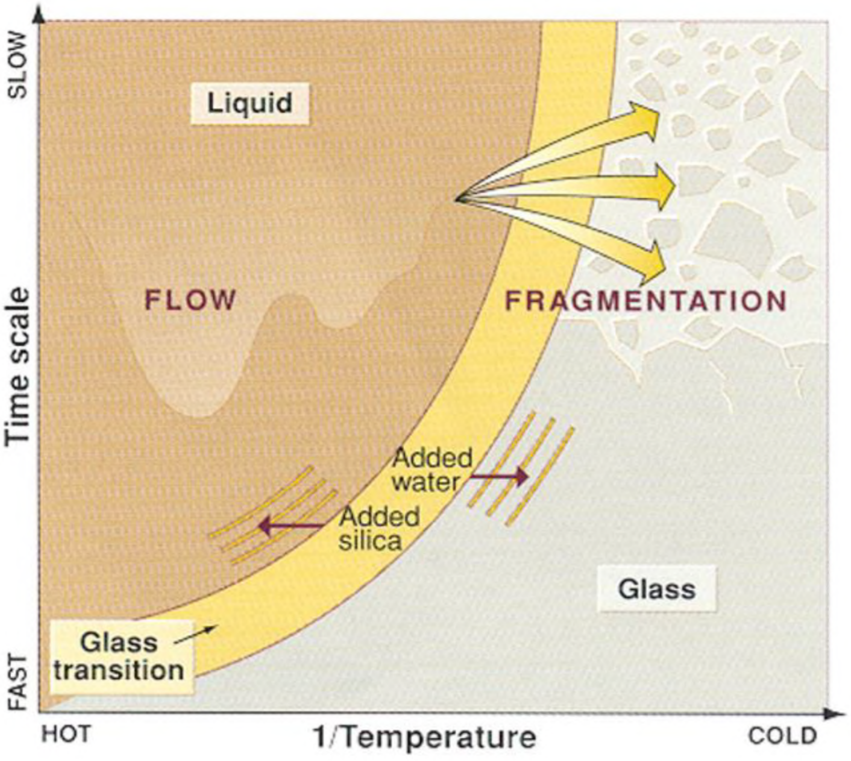

Figure 10: The glass transition in time-reciprocal temperature space. Taken from Dingwell (1996).

1.5 Magma mixing

Felsic and mafic magmas are known to erupt simultaneously from the same vent (Turner and Campbell, 1986). Mixing of mafic and felsic magma is common at many volcanoes, which is evidenced by zoned deposits of distinct magma compositions. Compositional variations are caused by processes such as fractional crystallisation, partial melting, contamination through assimilation and some minor thermal effects (Sparks et al., 1984). Compositionally dissimilar magmas are usually also dissimilar in temperatures and physical properties (i.e. viscosity and density) (Best, 2013). Magmas of different compositions can mix shortly before or during an eruption. Popular views on how long-lived magma chambers can host mixing are by either the dynamics of replenishment (Campbell and Turner 1985, 1986; Huppert et al., 1986), convective overturn (Eichelberger 1980; Huppert et al., 1982, 1984; Huppert and Sparks 1984), and chamber evacuation (Koyaguchi 1985; Blake and Ivey 1986a, b; Spera et al., 1986; Blake and Campbell 1986; Freundt and Tait, 1986; Blake and Fink 1987).

Layered magma chambers form due to differences in physical parameters. Less dense, evolved (e.g. andesite, dacite and rhyolite) magmas which are more enriched in silica and water are buoyant relative to the parent magma, so reside at the top of density stratified chambers. Basaltic magma tends to be more iron-rich and denser (Best, 2013). The stratified chamber can undergo convective overturning due to density differences which may lead to mixing (Turner and Campbell, 1984). Convection can cause detachment of less viscous, buoyant blobs which may become mingled mafic inclusions in felsic magma if the solidification is rapid (Best, 2013). Additionally, overturning of a gas-rich mafic layer into cooler silicic magma can cause sudden quenching, releasing significant quantities of gas, and therefore triggering a volcanic eruption (Turner and Campbell, 1986). During an eruption, both magmas can be tapped and have the potential to be erupted in one episode if the strength of the outflow is sufficient to overcome the buoyancy force acting as a horizon between the two miscible layers (Blake and Ivey, 1986). Mixing can occur during an eruption as two layers are simultaneously drawn out of a chamber and subsequently mix on ascent (Turner and Campbell, 1986).

Replenishment of new, hotter, less evolved magma in more evolved (silicic) magma chambers are nearly always less viscous than the resident magma. This can lead to mixing and in some cases eventual homogenisation of the magmas, producing an intermediate-type magma (Best, 2013). Less evolved magma from a mantle source rises into sialic rocks in the crust. The rising magma reacts with the surroundings to attempt to attain chemical and thermal equilibrium (Best, 2013). Crustal rocks are assimilated into the magma resulting in contamination. Volatiles released from heated country rock may contaminate volatile-poor magma.

Evidence for magma mixing includes:

1. Complex resorption and overgrowths in phenocrysts in quickly cooled volcanic systems (i.e. spongey zones in plagioclase).
2. Rapakivi overgrowth of plagioclase on alkali feldspar.
3. Disequilibrium phases such as xenoliths and xenocrysts.
4. Distinctive patterns in variation diagrams, rather than continuous trends.

Magmas can rise as a solitary magma batch (Scott and Stevenson., 1986; Ida and Kumazawa 1986; Koyaguchi and Blake 1989) or in magma-filled fractures originated from deep reservoirs (Duncan and Guest 1982). A rising magma batch can contain a single homogeneous magma or two of magma compositions, in which case the magmas can mingle and mix (Koyaguchi and Blake 1989). Results from fluid dynamic experiments carried out by Koyaguchi and Blake (1989) suggest that silicic to intermediate magmas overlying mafic magmas will be prone to mixing as the batch rises through the volcanic system, explaining some occurrences of small-volume mixed lava flows.

2 Methods

A total of 41 pyroclasts were collected in the field. Samples were washed by hand to remove any adhering dust or matrix. To provide a full analyses and representation of the pyroclasts, it was necessary to cut and polish sections to investigate internal structures.

A representative sub-sample were selected to be made into polished slabs and thin sections. The majority of the pyroclasts were not cut to due to their unique morphologies. Samples ACAF32, ACAF33, ACAF34 and ACAF35 were cut previously and ACAF5, ACAF11, ACAF17 and ACAF18 were extensively cut and polished into multiple slabs longitudinally. These samples were scanned on a flatbed scanner to a high resolution to determine internal flow textures and heterogeneities. Samples ACAF32 and ACAF11 were chosen to drill 5 mm cores for analyses (optical microscopy and scanning election microscopy) due to the presence of flow banding and ease of maintaining the scoria/glass contact through drilling. Of the seven cores drilled, five were made into thin sections and a further five sections from whole pyroclasts. These ten thin sections were analysed under an optical microscope for the purpose of textural and mineralogical descriptions. Photos were obtained in plane and cross polars (PPL and XPL, respectively).

2.1 Scanning Electron Microscopy

Polished thin sections were analysed using a Hitachi SU-70 high resolution Scanning Electron Microscope (SEM) equipped with a 24 Oxford Instruments energy dispersive X-ray spectroscopy (EDS) microanalysis system at the G.F Russell Electron Microscopy Facility (Department of Physics), Durham University. The pyroclasts were analysed for phenocryst textures, glass and scoria textures, and the contact between glass and entrained scoria clasts. Backscattered electron (BSE) images were obtained with low and high magnification settings.

2.2 Electron Microprobe Analysis

Plagioclase crystals were chosen for analyses as they provide insight into shallow crustal processes as melts ascend and plagioclase crystals are sensitive to changes in melt composition. Composition and morphology of plagioclase is controlled by changes in temperature, pressure, melt composition (including water content), growth, dissolution and nucleation kinetics (Bennett et al., 2019). Plagioclase has slow diffusion of CaAl and NaSi cations (Morse 1984; Grove et al., 1984) preserving textures within a magmatic system (Bennett et al., 2019).

Whole scans of thin sections (scoria and obsidian) were obtained using a flatbed scanner which enabled phenocrysts to be identified, providing maps for EPMA analyses. In-situ major and minor element analyses of obsidian, glass in scoria, phenocrysts, microlites and iron-titanium oxides were performed at the University of Edinburgh using a Cameca SX100 Electron Microprobe, equipped with 5 wavelength-dispersive spectrometers. Data was collected with a 15 kV accelerating potential, a static beam, kα emissions and a beam current of 8 nA. Spatial resolution on the EMPA is as high as one micron and has good analytical precision. Glass analyses were chosen in areas with no microlites to avoid mis-readings.

Totals between 98 wt. % 102 wt.% were accepted for glass and feldspar data. Totals between 93 and 98 wt. % were accepted for iron-titanium oxides. Any negative value has been recorded as BDL (below detection limit). Primary glass data was normalised to a volatile-free basis of 100 wt. % to facilitate comparisons. All standards are within less than 5 % of the published values. Representative EPMA data of 2σ analytical errors are presented with data on corresponding graphs. Data for all geochemical analysis is found in the Appendix. Normalised data of obsidian and scoria glass was first sorted by aluminium oxide content. Data points which contained over 16.5 wt.% Al_2O_3 were removed, as these are likely mixed glass and feldspar (glass typically does not have high Al_2O_3 concentrations). The data was then sorted by calcium oxide. Those which had CaO wt.% over 5 were removed. Finally, the glass was sorted by iron and magnesium oxide concentrations. In the obsidian data, data points higher than 6.5 wt.% of FeO were removed, and 2.5 wt.% for MgO. Feldspar phenocryst data points were sorted by CaO, MgO and FeO concentrations. Two feldspar data points were removed due to containing >67 wt.% CaO, particularly as the next highest CaO concentrations were ∼11 wt.%. FeO and MgO concentrations over 1.2 wt.% and 0.2 wt.% respectively were removed. Raw data is available to observe rationale of disregarded totals.

Eruptive water concentrations of the obsidian clasts have been collected using Fourier-transform infrared spectroscopy (FTIR), however this is not presented in this thesis as the data belongs to person which collected it within the collabrative Ascension group.

3 Results

This chapter provides the first comprehensive textural and physical description of the pyroclasts on a macro- and microscopic scale. Glass and mineral (phenocrysts, microlites and oxides) major and minor element data are presented on the glass and scoria.

3.1 Field description

The obsidian pyroclasts occur amongst scoria and spatter lapilli and bombs in pyroclastic ramparts constructed by a small-volume basaltic fissure eruption on the east side of Ascension Island (figure 11) The fissure eruption is approximately 40 to 50 Kyr old (pers comm R. J. Brown). The fissure is ∼0.7 km long, 3040 m wide (rampart crest to rampart crest) and lined by pyroclastic ramparts up to 12 m thick (figure 12). The eruption occurred through a sequence of thick rhyolite and trachyte lavas. The scoria ramparts overlie a whitish flow-banded rhyolite lava in which a thin, orange weathered surface has formed. The eruptive stratigraphy consists of:

1. A lower ∼50 cm-thick explosion breccia composed of yellow/white tephra and rhyolite lithic clasts.
2. 6-12 m of scoria and spatter within scattered obsidian pyroclasts throughout (see figure 13).

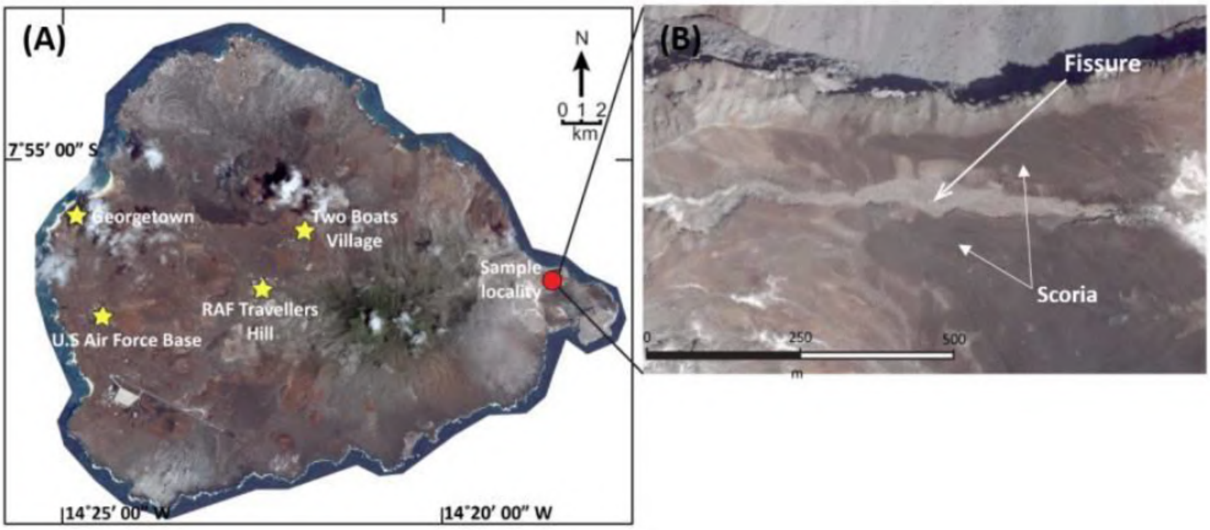

Figure 11: (A) Google Earth image of Ascension Island showing sample locality (red circle). (B) Google Earth image of the fissure where the agglutinated scoria and obsidian pyroclasts were uncovered.

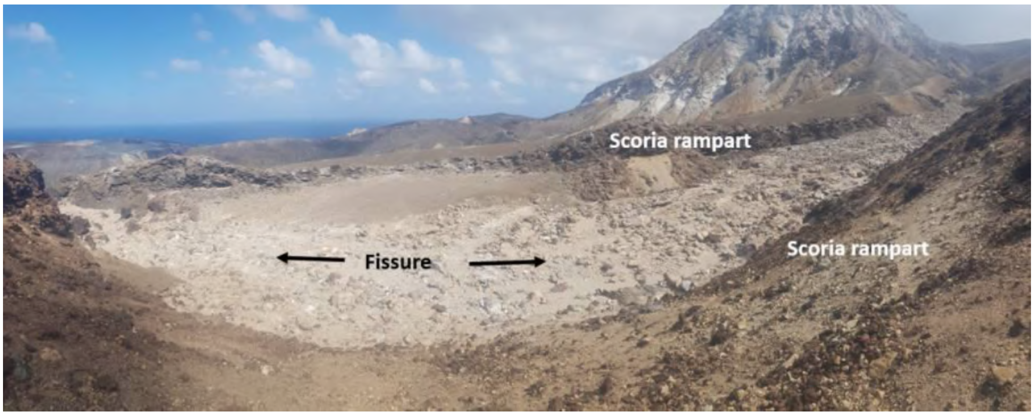

Figure 12: Photograph of the fissure. Scoria ramparts are built up on the margins of the fissure.

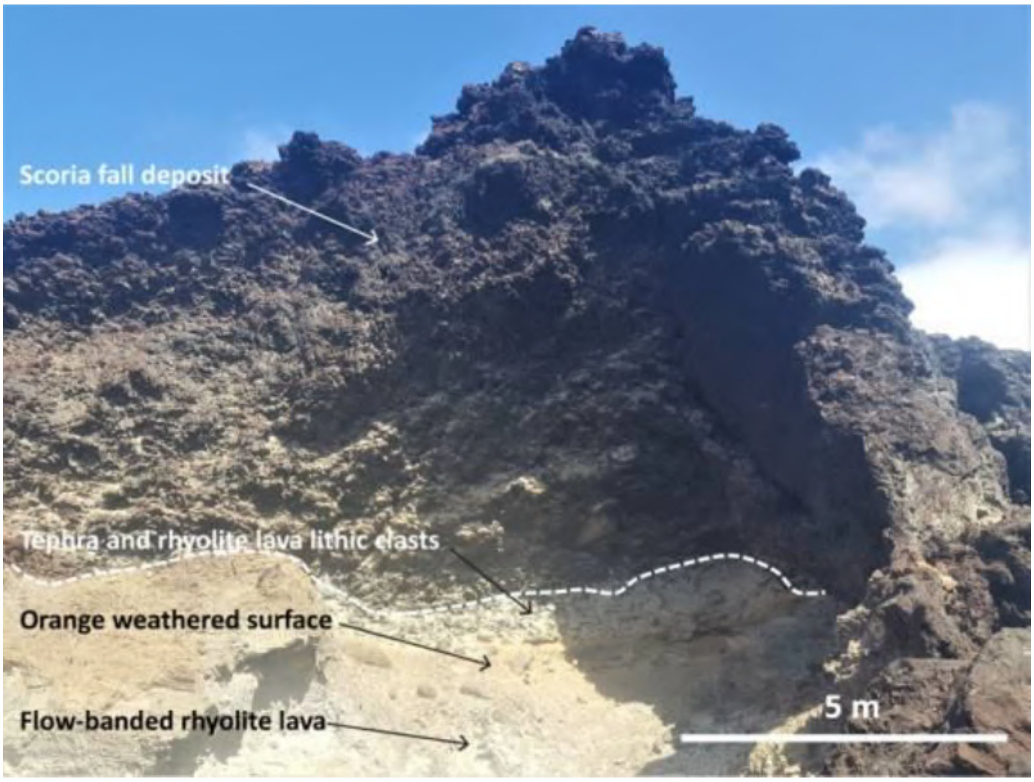

Figure 13: Photograph of eruption sequence. White dashed line distinguishes pre-erupted deposits and the scoria fall deposit, in which obsidian pyroclasts are scattered.

3.2 Pyroclast description

3.2.1 Scoria

The scoria accounts for the largest volume of erupted products (as visible in figure 13), forming largely non-welded ramparts. The scoria is moderately vesicular and appears brown to orange-brown (due to oxidation of iron). The vesicles are ellipsoidal to irregular and often coalesced. The largest vesicles are up to ∼1 cm, typically found in the core of the clasts. Scoria clasts commonly have chilled rinds, in which vesicles are smaller (<2 mm). Pale white/yellow-coloured lithic clasts of trachyte and rhyolite are often stuck to the surface of the scoria as well as entrained within them (figure 14).

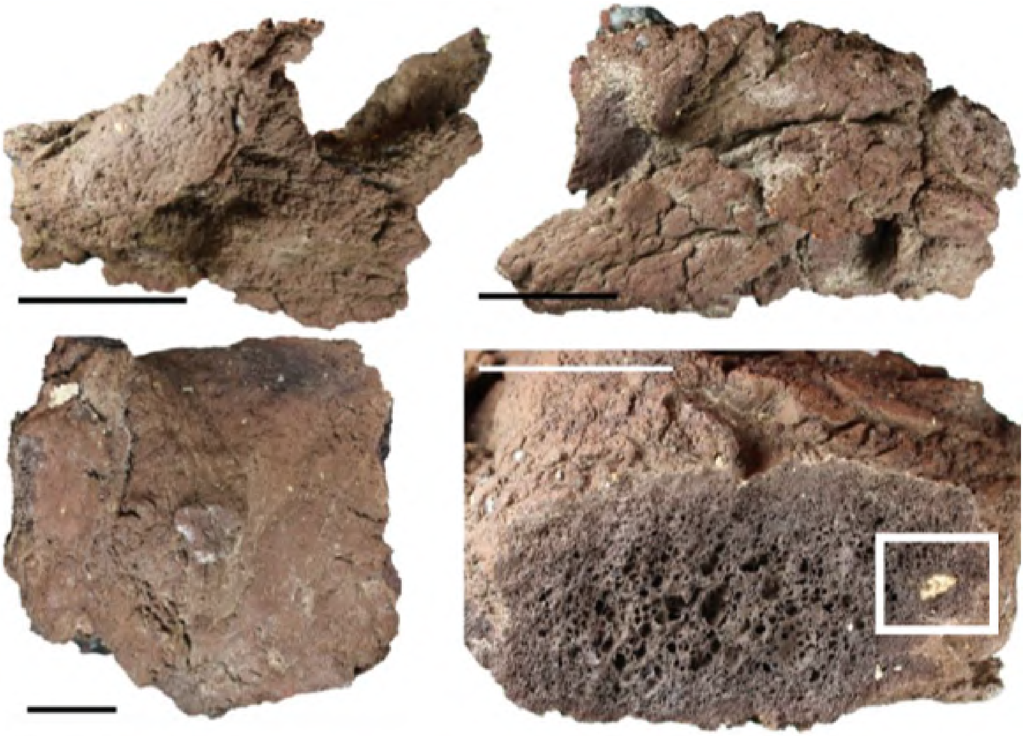

Figure 14: Photograph of co-erupted scoria clasts (all scale bars are 3 cm). White box indicates lithic clast found within the scoria.

In thin section, scoria clasts vary from highly vesicular (figure 15d) to vesicle-poor (figures 15a). The scoria has a finely-crystalline groundmass and in some samples is glassy. There is a red/brownish oxidation (visible in cross polarised light) around the edges (figure 15b & d). Back scatter images (BSE) show sub-spherical to highly contorted vesicles in the scoria (figure 16). In some samples the vesicles in the scoria appear angular with margins defined by crystals (figure 16c). Phenocrysts in

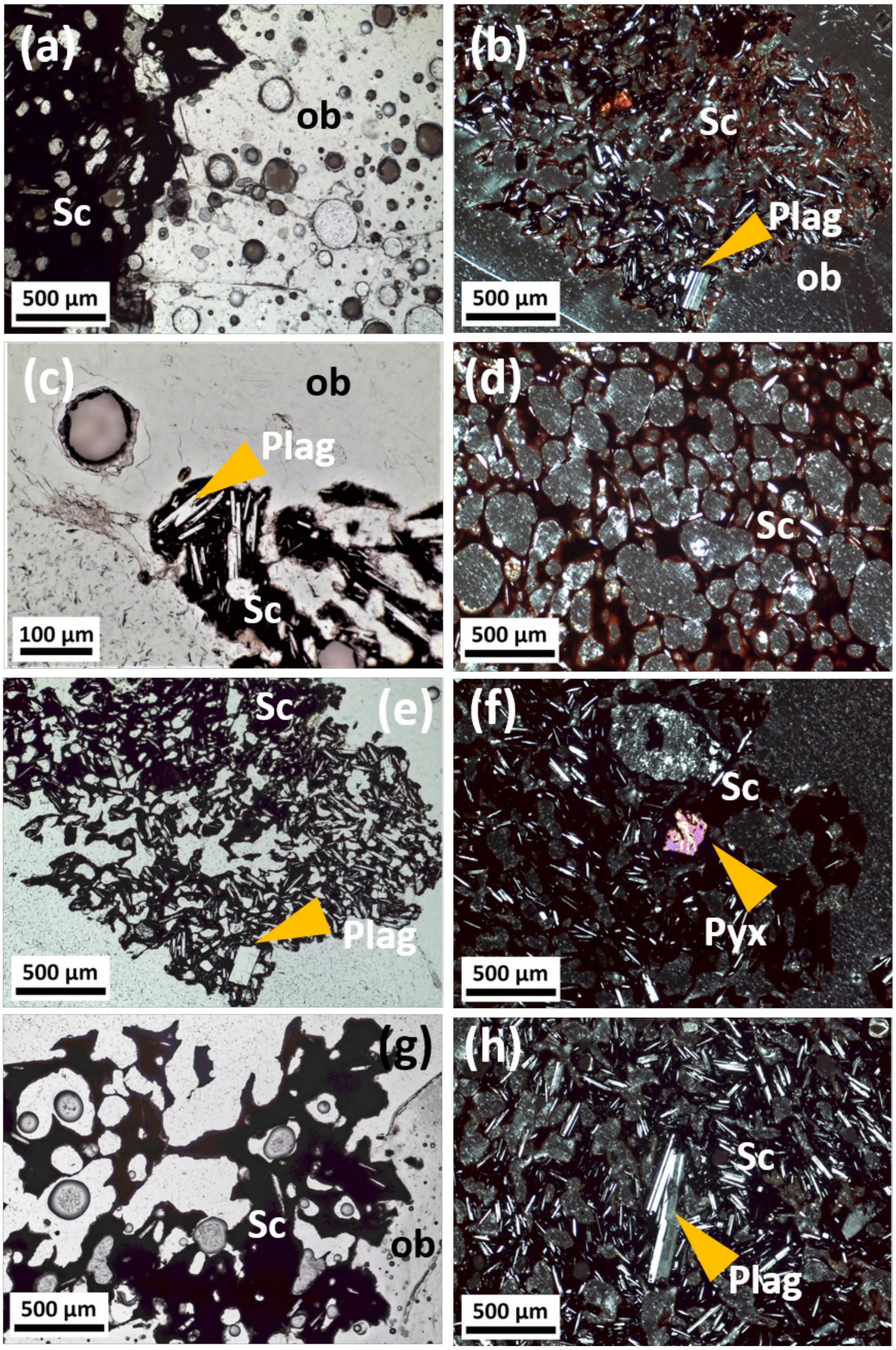

Figure 15: Microphotograph of scoria (A,C,E,G taken in plane polarised light, PPL, B,D,F,H taken in cross polarised light, XPL). (A) Scoria (brown/black) in contact with obsidian (obsidian appears translucent - pale yellow in PPL) with moderate to poor vesicularity. (B) Moderately vesicular scoria, with plagioclase and pyroxene macrocrysts present. (C) Scoria with acicular plagioclase crystals. (D) Highly vesicular scoria (E) Same as B, in PPL. (F) Pyroxene microphenocryst with exsolution lamellae in scoria with fine groundmass. (G) Moderately vesicular scoria. (H) Skeletal plagioclase phenocryst in scoria with fine groundmass. Sc: Scoria. Ob: Obsidian. Pyx: Pyroxene. Plag: Plagioclase.

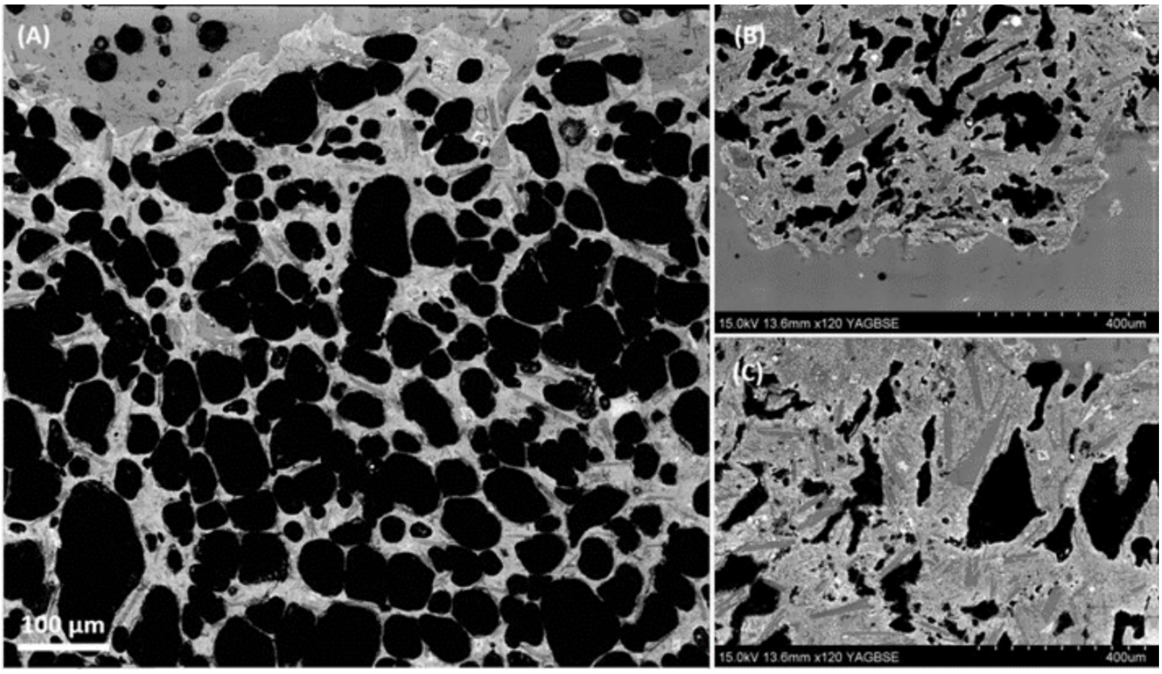

Figure 16: BSE images of scoria. (A) Montage of scoria BSE images. (B C) BSE images of scoria.

the scoria which occur as euhedral to subhedral laths are either acicular or skeletal in morphology and have multiple twinned lamellae indicative of plagioclase feldspar. There are no phenocrysts which appear zoned or resorbed. Crystallites in the groundmass appear to be the same feldspar species and can be as large as 200 μm (figure 15h).

3.2.2 Obsidian pyroclasts

The obsidian pyroclasts are texturally distinct, dense and dark grey. They are scattered throughout the scoria ramparts, and account for $<<0.005$ % ($\sim$0.0007 m^3) of the total erupted pyroclastic material. Within the scoria rampart, the obsidian clasts are sparse and difficult to see, occurring in abundances of $\sim$5 cm^2 (figure 17).

The obsidian pyroclasts range from coarse ash-size (0.0332 mm), to lapilli-sized (2-64 mm) spatter bombs, >40 cm in diameter. The clasts exhibit a wide range of morphologies (figure 18;19), but the typical clast-type is an asymmetrical, oblate pyroclast of agglomerated glass, scoria and lithic fragments (figure 20) resembling cowpat bombs. The obsidian pyroclasts differ substantially from other typical volcanic bombs (e.g. bread-crust, cored, spindle), particularly due to the lack of a chilled exterior and a consistent morphology. Most of the clasts have a smooth exterior with surface folding

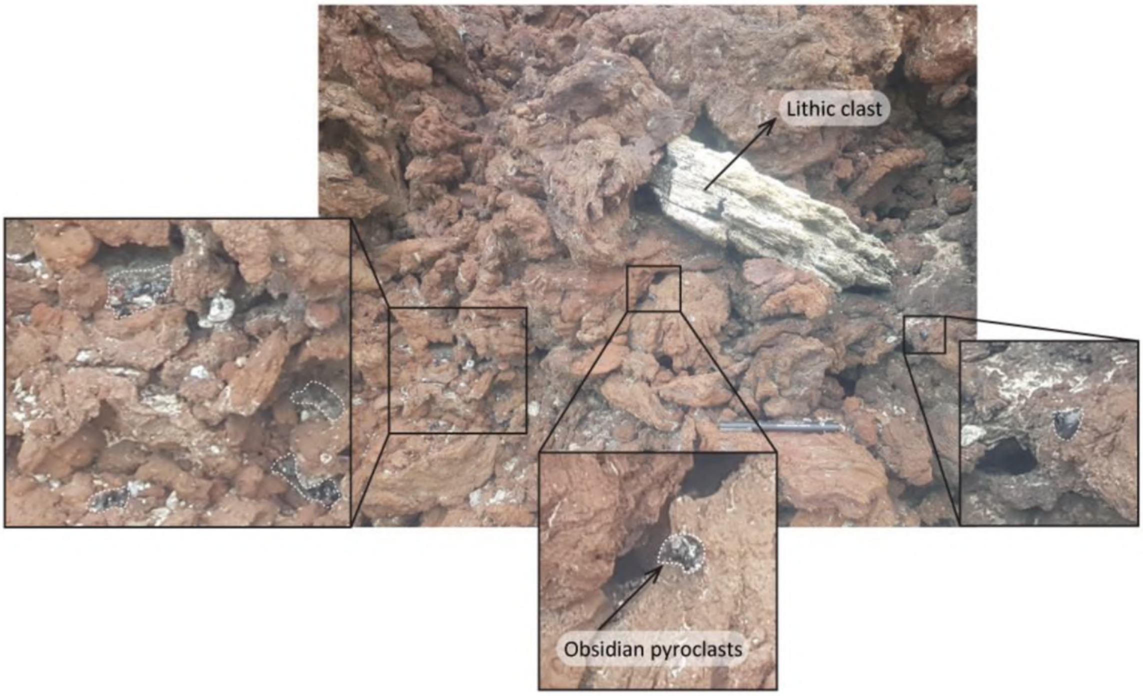

Figure 17: Photograph of ~1 m^2 area of the scoria rampart showing the outcrop relationship between the scoria and obsidian pyroclasts. Pen for scale (15 cm). The obsidian pyroclasts infill voids of the rampart.

Figure 18: Photographs of flat-topped obsidian. (A) Molten glass has landed within a cavity in the rampart and levelled out to a near-perfect flat top. Underneath, the glass has continued to flow (white box). The edges of the obsidian pyroclast have a higher vesicularity than the centre. (B) Small (<3 cm) scoria and lithic clasts are adhered to surface of levelled obsidian. Pen for scale (15 cm). (C) Near-perfect flat top of obsidian pyroclast indicates way up obsidian landed.

Figure 19: Photographs showing the outflow of obsidian clasts. (A) Large tongue-shaped outflow from obsidian which has pooled within a cavity. (B) Obsidian flowed vertically over scoria and has pooled in multiple places. (C) Obsidian has flowed down scoria clasts, entraining the scoria, and formed a pendant drop.

and fluidal-looking textures indicating they were capable of flowing upon impact. The obsidian is often found within voids of the subjacent scoria fall deposit, therefore on eruption, obsidian must have percolated through scoria, forming pendant-drop shapes or irregular tongue-like outflows (figure 19), and in some cases levelled out (figure 18). Some field examples show that the obsidian stretched into thin columns, which fed into an accumulation on top of scoria clasts and then continued to flow below, resulting in a small drop shape (figure 19). The suspended drops typically do not exceed a couple of centimetres in length (maximum length recorded ~3 cm) (figure 25b & c). Figure 25a shows a frozen drop which has reached underlying scoria and has begun to accumulate at the base. Within the drops, the flow banding reflects the morphology of the obsidian and phenocrysts appear to be orientated in the direction of flow.

The obsidian pyroclasts have a range of features which provide distinct indicators of way-up (i.e. how the obsidian impacted on the scoria). Typically the obsidian pyroclasts have larger scoria and lithic clasts on the base, which are then enveloped by the obsidian as it flowed post-impact (figure 26). The surface of the obsidian (in most examples, only seen on the top of the pyroclasts) is frequently covered by small lapilli to ash-sized particles of scoria and lithics (approximately <5 mm) (figure 20). Other way up indicators include ductile deformation features such as ductile fractures and stretched filaments.

Larger obsidian pyroclasts occur as oblate spheroids, which lack flow features or fractures (figure 21e). Those which differ are typically less dense, and lack features such as brittle, ductile and annealed fractures, glass filaments, indicative way-up textures and flow banding, which are mostly all seen within the pyroclasts. Some surfaces of the pyroclasts are almost entirely covered in fine particles of scoria and lithics, therefore are difficult to diagnose a way-up (figure 21e). In rare cases (figures 21a & c) some oblate clasts lacking flow features show larger scoria and lithic fragments on the base. A particularly unusual pyroclast is displayed in figure 21 f & g. It is cuboidal with near-parallel surfaces (roughly 2.7 x 1.5 x 1.5 cm in length) and has entrained scoriaceous ash particles (<<1 mm) on the top face of the glass. The surface has elongate, extruding ridges, which makes the clast rugged to the touch. This crinkled surface is also exhibited in other clasts that differ from the typical smooth exteriors. As seen in figure 21c & d, the obsidian has multiple protruding ridges. The glass has sunk in the centre of two adhered scoria clasts, compressing the quenching glass forming crinkled textures.

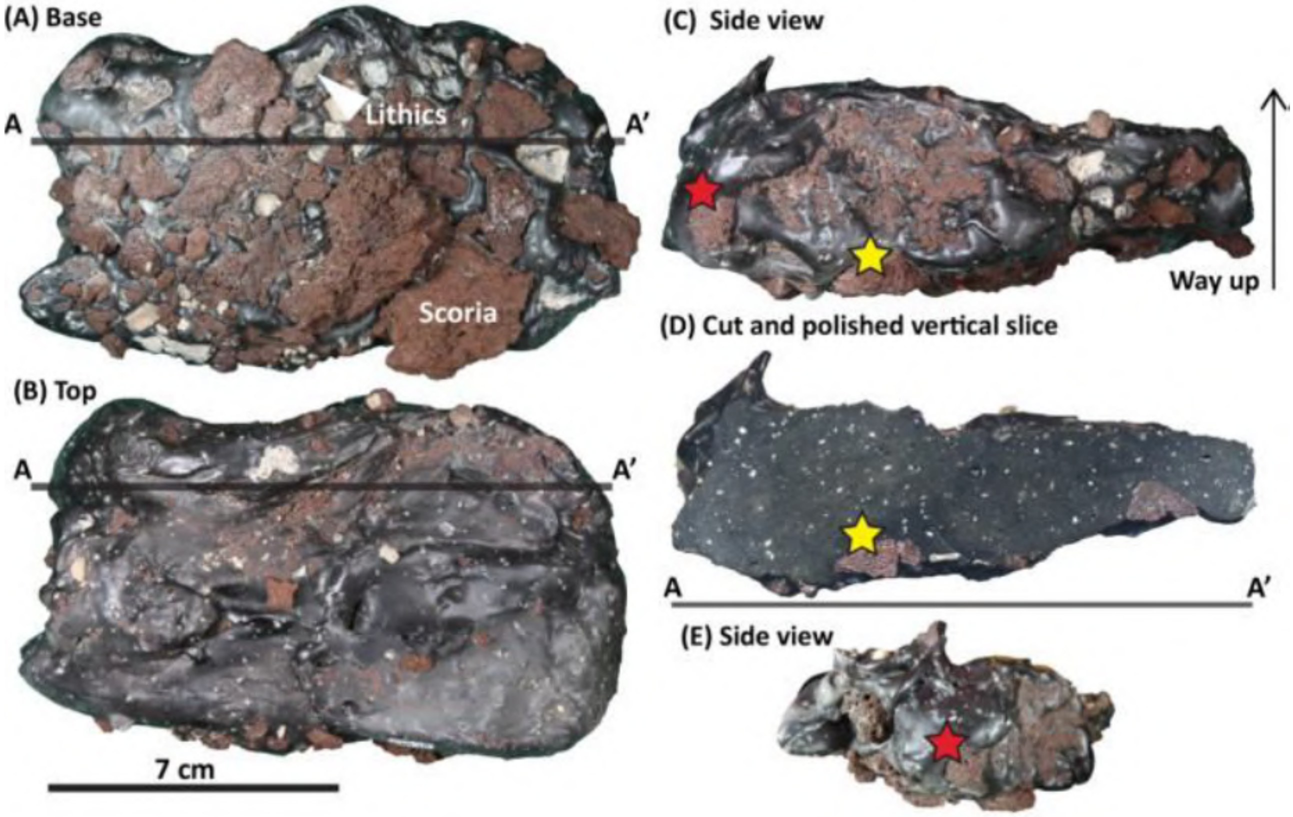

Figure 20: Photographs of ACAF5 hand sample in multiple orientations, representing a typical obsidian pyroclast. The top has fewer adhered scoria and lithic clasts and shows folding on the surface. Stars indicate same feature shown on different orientations.

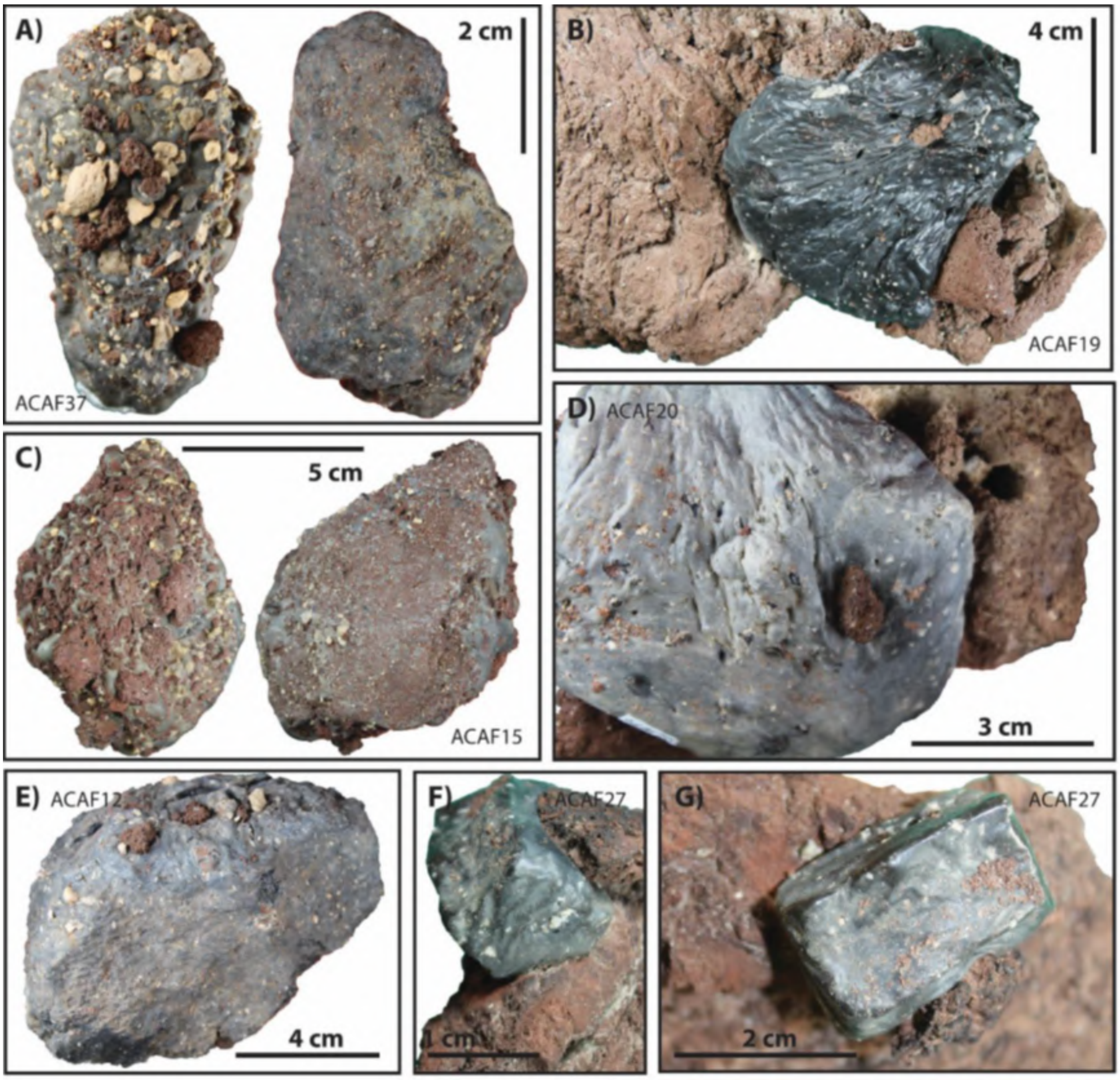

Figure 21: Photographs of non-idealised clast types. (A) Sub-rounded clast is less dense and lacks fractures of viscous flow features. (B) Scrunched, deflated texture on the surface of the glass between scoria clasts. (C) Sub-rounded clasts. The clast is covered in small particles of scoria/lithic fragments. (D) Scrunched glass texture. (E) Sub-rounded pyroclast only contains a few fragments of scoria and lithic clasts. (F & G) Cuboid-shaped pyroclast with sub-parallel edges.

Fractures and glass filaments

Three types of fractures occur within the obsidian: (1) brittle, (2) ductile and (3) annealed. Annealed fractures are the most common fracture type found in the obsidian, appearing on just under half (45%) of the samples. Annealed fractures are thermal fractures where recrystallisation occurs along the interface of the fracture. They are irregular, thin (∼1 mm) pale grey to yellow lineaments, millimetric to several centimetres in length, and form networks on the top of the samples. Annealed fractures are particularly clear on samples where the glass has levelled out to near-perfect flat tops (figure 22). In thin section, annealed fractures do not pass through phenocrysts, but penetrate through bubbles and entrained scoria clasts (figure 29).

Figure 22: Photograph of annealed fractures on the top of a pyroclast. Scale bar is 2 cm.

Brittle fractures are pervasive through glass and adhered scoria clasts. They formed post-eruption once the obsidian was quenched. The brittle fractures are up to several centimetres in length, but do not protrude deep into the glass (<1cm). Approximately one third of the 41 pyroclast hand samples have undergone brittle fracturing.

Ductile fractures mostly occur on the top of pyroclasts as subparallel cracks, several centimetres long and wide (seen on ACAF2 and ACAF7) (figure 23), but can occur on the side and base of the clasts. They are not as common as annealed or brittle fractures, and appear on ~10 % on the pyroclasts. There are no fractures present on smaller pyroclasts (ACAF14, ACAF15, and ACAF16). Glass filaments occur in conjunction with ductile fractures, where they frequently bridge ductile openings.

Glass filaments are intricate threads which occur on the top of the pyroclast are commonly retracted and relaxed onto the obsidian pyroclasts (figure 24d, e). Most filaments are <1 mm wide, and therefore frequently broken in the centre, where they would have reached their thinnest diameter. The filaments are several millimetres long and many may bridge one fracture (figure 24b). Figure 24a shows abundant stretched filaments bridging a ductile fracture as the glass has been stretched in multiple directions. Glass filaments are more common on larger clasts.

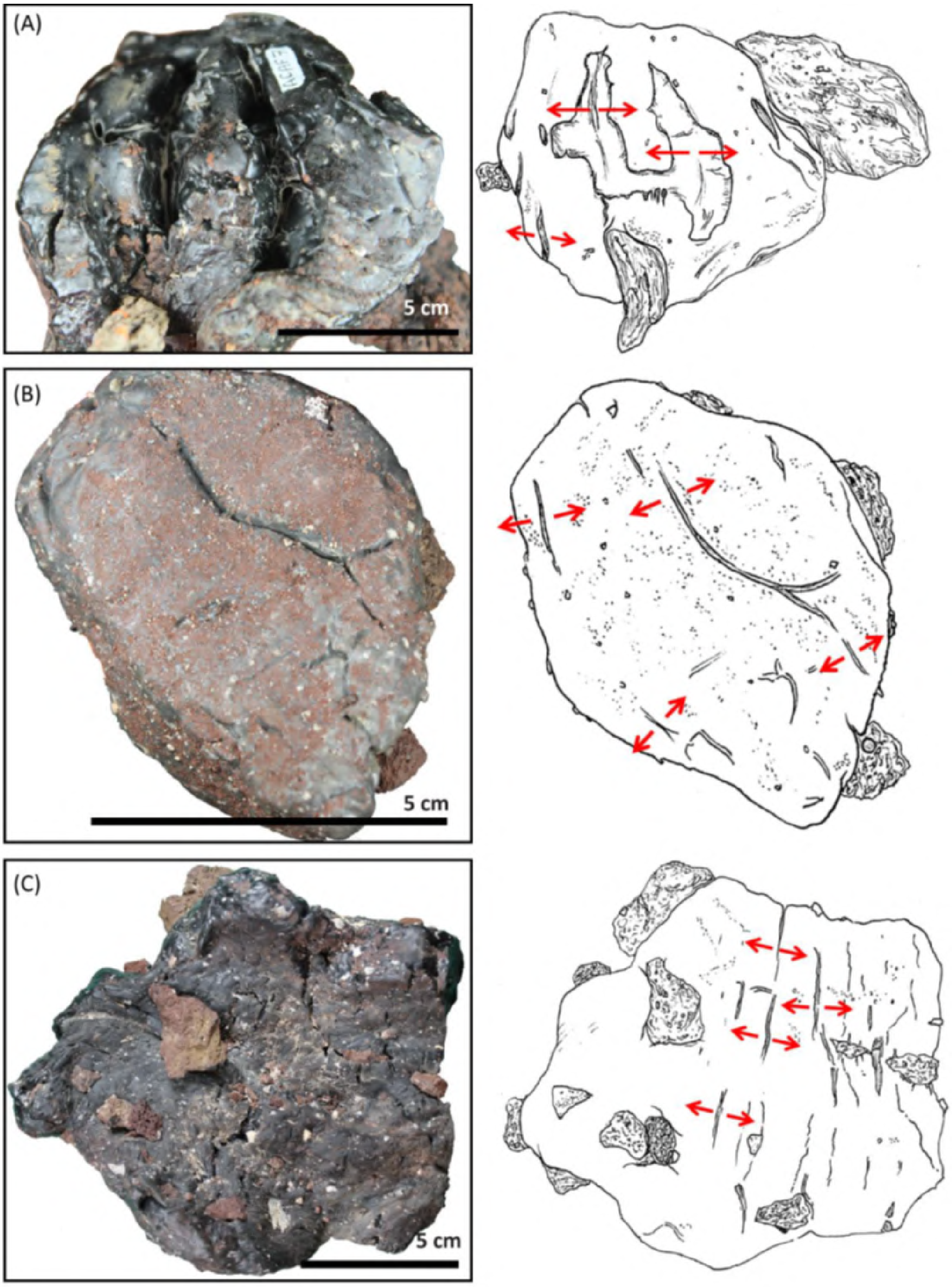

Figure 23: Photographs showing ductile openings on the top of the glassy pyroclasts with sketches. The fractures protrude into the glass by several centimetres at most but are usually <1 cm deep. (A) Sub-parallel fractures which are ~2 cm deep. (B) Small network of ductile fractures. (C) Small sub-parallel fractures ~1 cm in length.

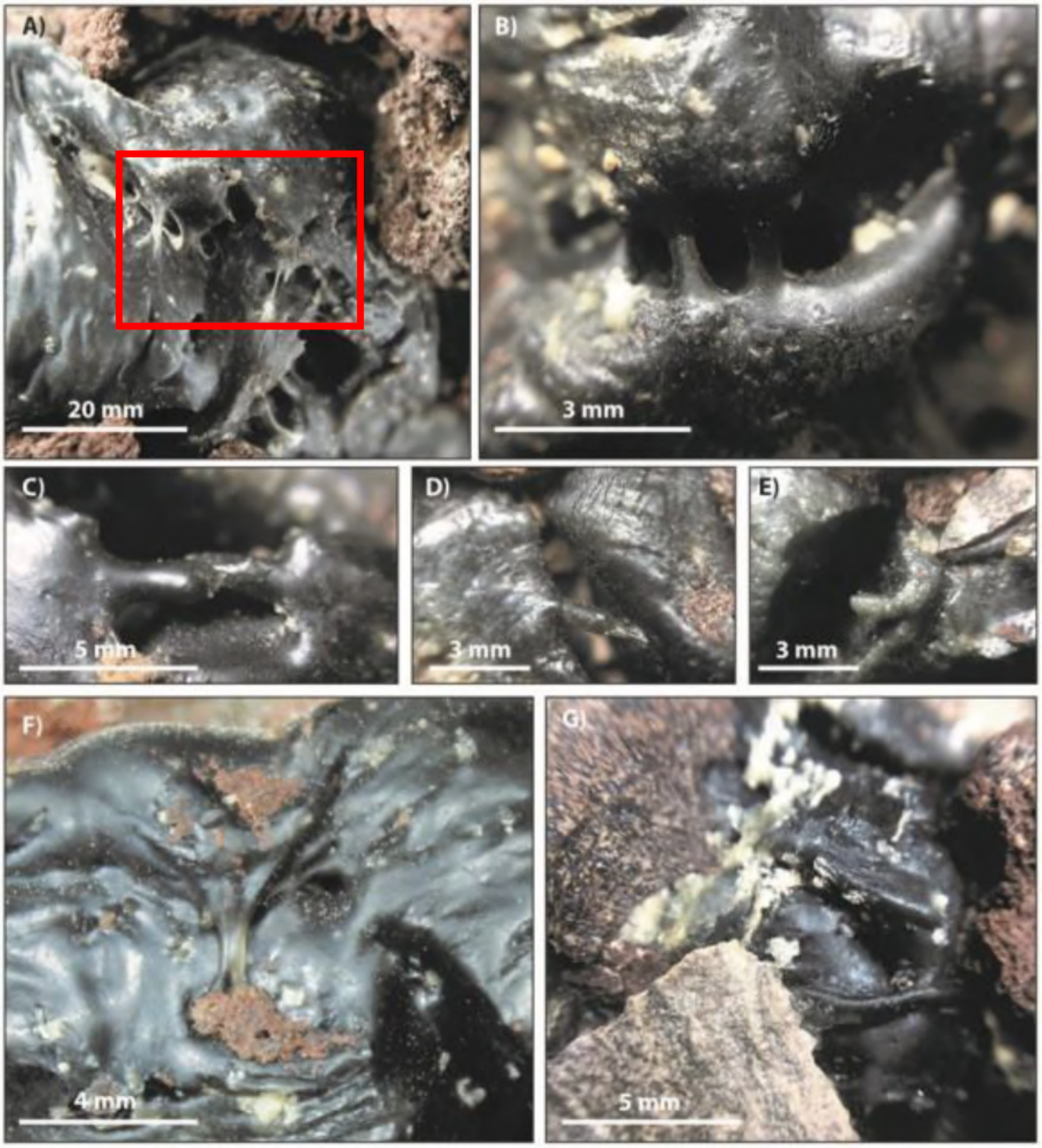

Figure 24: Photograph of stretched glass filaments. (A) Multiple glass filaments bridging ductile fractures. Some filaments have only extended several millimetres before they have fractured. (B) Stretched filaments bridging one ductile fracture found on the side of a pyroclast. (C) & (D) Filament stretched across a fracture found on the top of the pyroclast. (E) Retracted glass filament extended over a brittle fracture. (F) Relaxed glass filament. (G) Multiple relaxed glass filaments found on the top of the pyroclast.

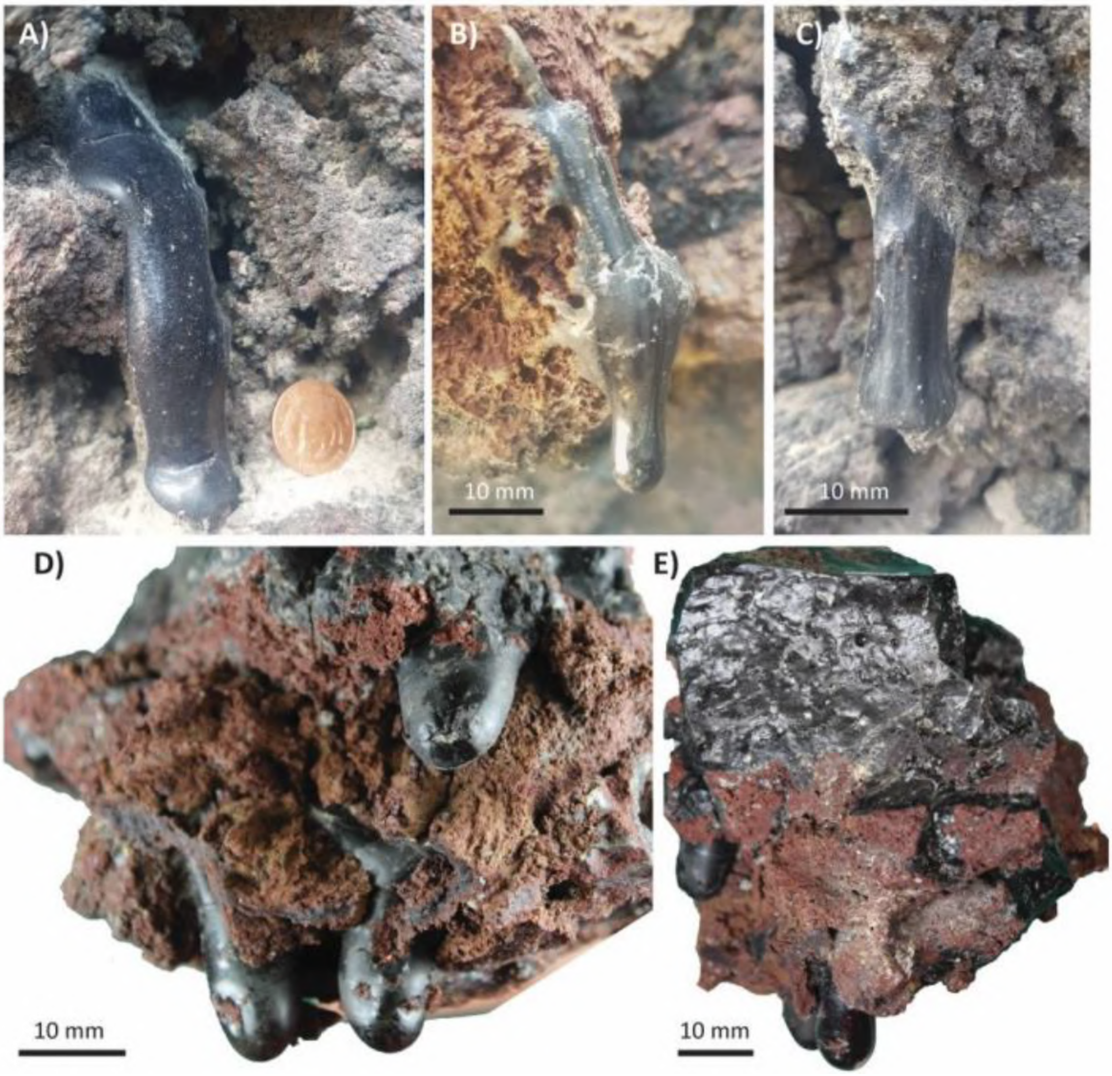

Figure 25: Photographs of obsidian pendant drops. (A) Glass has trickled down scoria clast and has begun to pool on underlying scoria (coin for scale, St Helena two pence, 25.91 mm diameter). (B & C) Suspended obsidian drops from scoria. (D & E) Three solidified drops which have flowed through scoria.

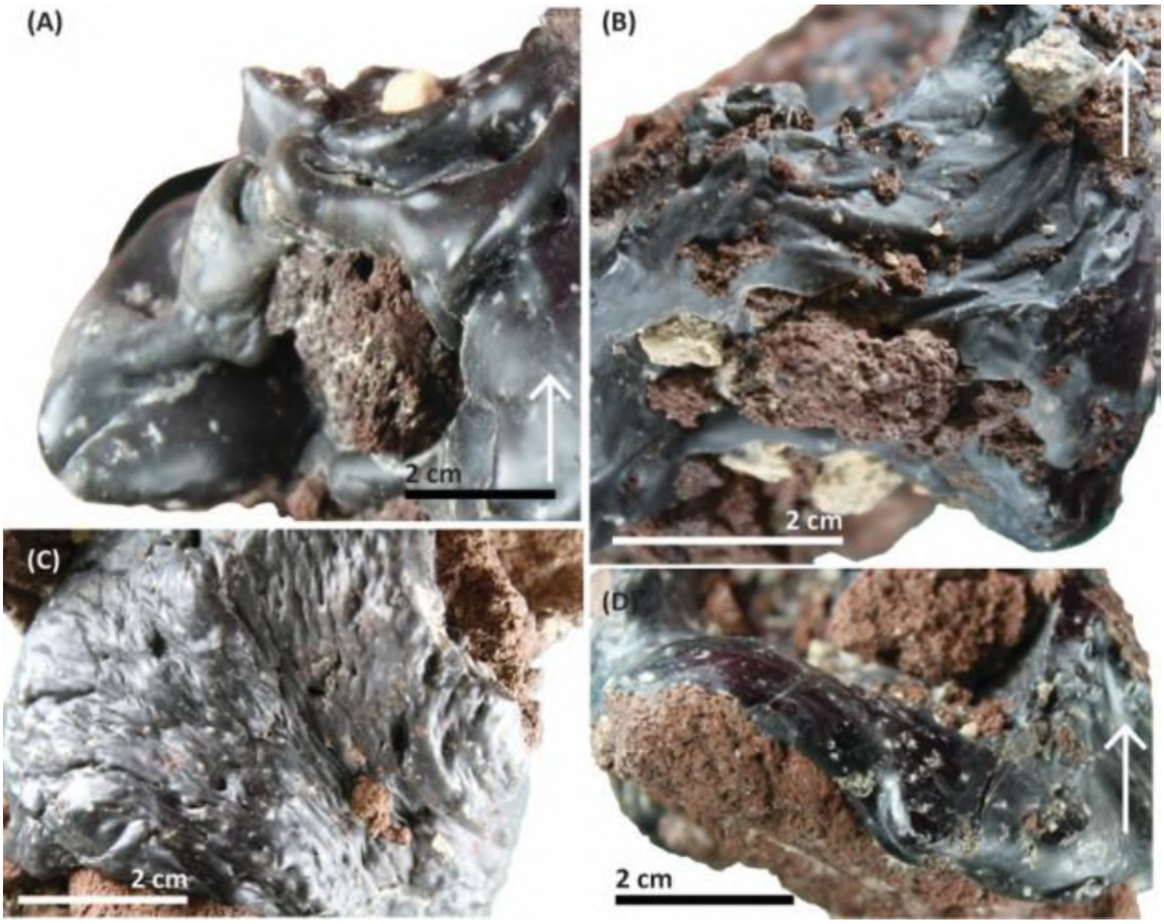

Figure 26: Photograph of flow textures in the obsidian. White arrow indicates way up. (A) Obsidian has repeated folding over the top of a scoria clast. (B) Obsidian has a rough texture. (C) Obsidian has collapse between scoria clasts creating a crinkled texture. (D) Obsidian has begun to lip around a scoria clast.

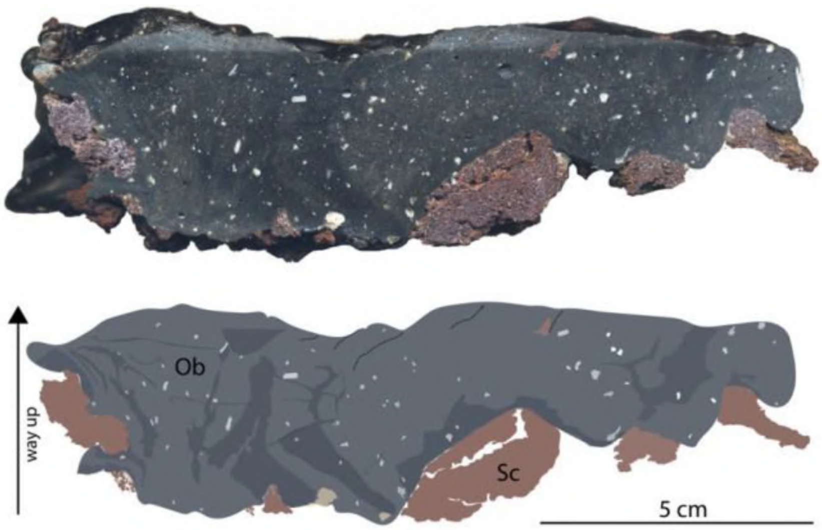

Figure 27: Flatbed scan of cut and polished section of pyroclast sample ACAF5. Sketch below emphasises flow banding in the obsidian by contrasting colours. The flow banding in randomly orientated but is approximately vertical relative to flow of the obsidian.

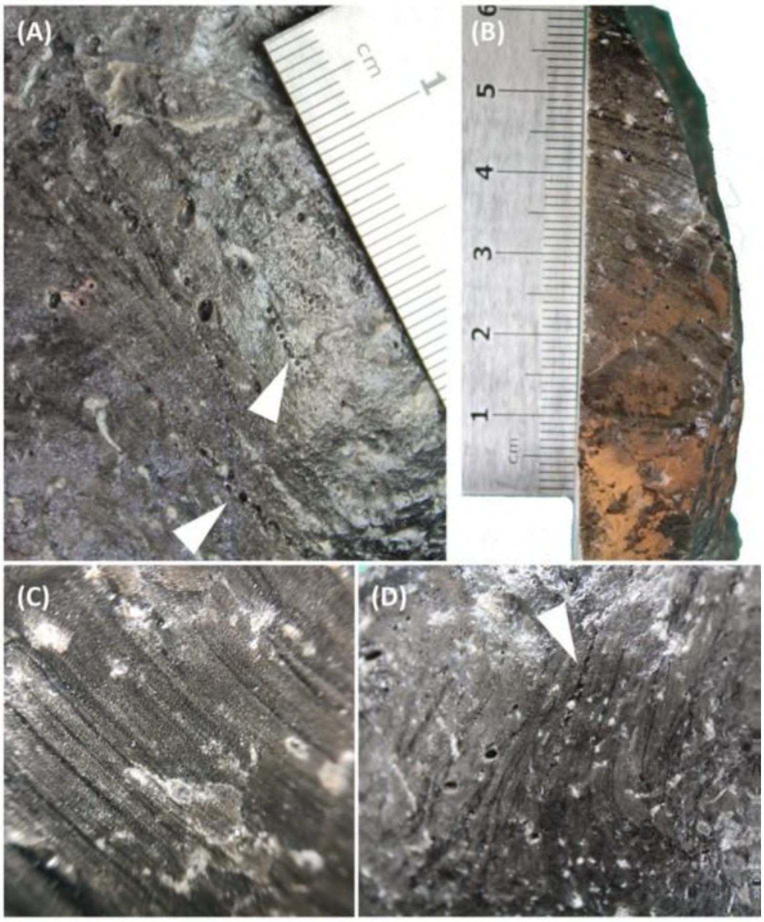

Figure 28: Photograph of flow banding in the obsidian. White arrows point to aligned bubbles to the same orientation of the flow banding.

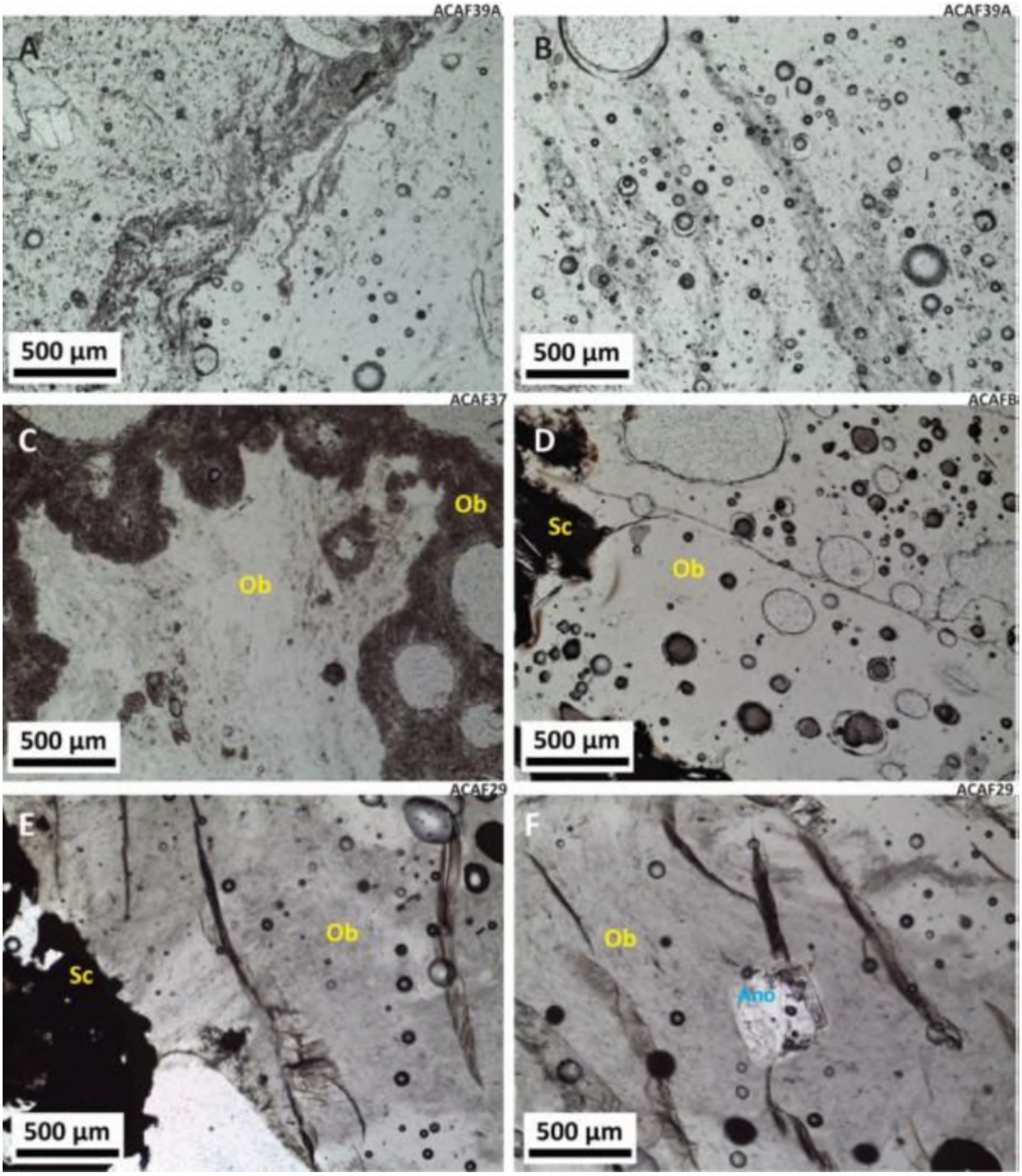

Figure 29: Microphotograph of obsidian textures taken in plane polarised light (PPL). Sample number can be found top right of each microphotograph. (A & B) Irregular flow banding in the obsidian (defined by the differences in glass colour). (C) Sharp contact between altered (dark brown) and unaltered (pale, translucent yellow) glass. (D) Fracture terminating at entrained scoria clast. (E & F) Annealed fractures.

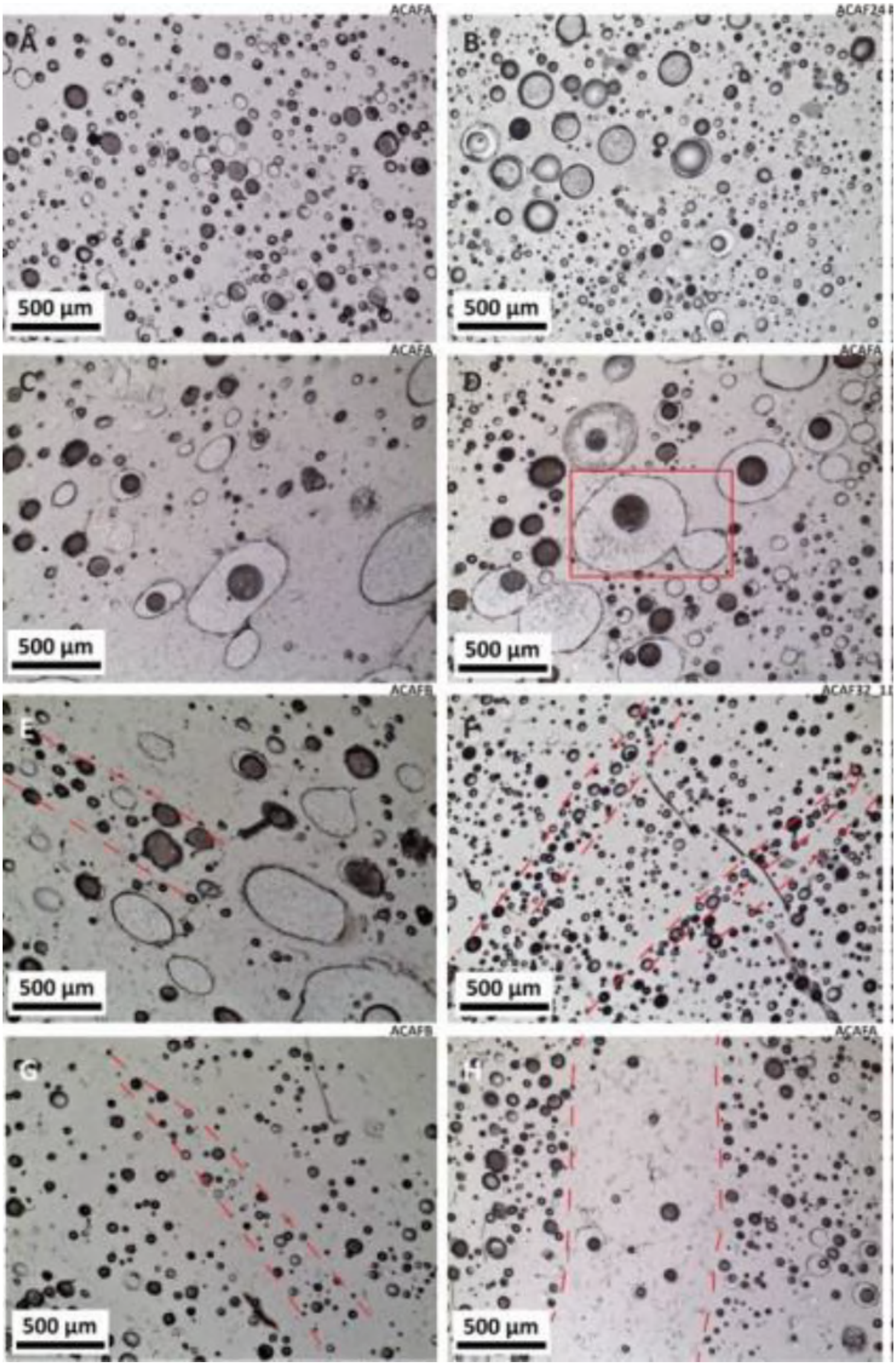

Figure 30: Microphotographs of bubbles in obsidian. Taken in PPL. Sample number can be found top right of each microphotograph. (A & B) Spherical bubbles with no preferential alignment. Larger bubble cluster in B. (C) Distorted sub-spherical bubbles. (D) Coalesced bubble (red box). (E) Band of aligned sub-spherical bubbles (shown by red dashed line). (F) Smaller, aligned groundmass bubbles. Fractures run perpendicular to bubble bands. (G) Aligned spherical bubbles. (H) Flow banding defined by differences in bubble number densities.

Flow banding

Flow banding is defined by colour differences in the glass and variations in bubble and microlite number densities (figure 29a, b). In regions where there are fewer bubbles, microlites are more abundant (figure 30). Figure 28 shows thin, parallel laminations which represents flow banding seen on the pyroclasts externally. Small (<1 mm diameter) bubbles are often aligned parallel to flow banding (figure 28). The flow banding is mostly irregular and mimics the overall flow direction of the obsidian (figures 27; 29).

Vesicles

Vesicles in the obsidian clasts range in size from ∼500 to 700 μm in diameter. Small groundmass bubbles are <100 μm and sometimes <<10 μm. The vesicles are spherical to sub-spherical, showing minimal to no distortion. Typically, the smaller vesicles show a higher sphericity (figure 30). Larger vesicles are slightly elongated and parallel to flow banding (figure 30). Vesicles appear concentrated in bands of similar sizes (figure 30f & g) or with the direction of the flow banding within the glass (figure 30e). Some examples show that the vesicles have no common trend (figure 30a) and appear static. Rarely, vesicles have coalesced (figure 30d), but typically are found isolated. Bubble number densities vary between samples, the glass is never completely bubble-free, but there are regions where bubble number densities are low, and microlite population is higher (figure 30h). In cut and polished slabs, phenocrysts are attached to vesicles (figure 31).

Figure 31: Cut and polished slab shows phenocrysts (∼2 mm) nucleated to vesicles.

3.2.3 Achneliths

Black to grey glassy spheroids which resemble achneliths are found scattered in the scoria ramparts. They vary in size from 0.1-10 mm. Achnelith morphologies trend towards spheres, however elongate examples are present and exhibit glass pendants extending 2 mm (figure 32), similar to Peles tears. Surface textures include smooth, fluidal morphologies with flow banding (figure 32e) and irregular surface depressions. Euhedral to subhedral feldspar phenocrysts are visible in larger achneliths (>5 mm) and small fractures (millimetric in size) are present in <25 % of the achneliths. The achneliths occur mostly are singular spheres, and rarely as coalesced clusters (figure 32f). Achneliths are found attached to the exterior of scoria and lithic fragments that are no larger than 1 cm (figure 32).

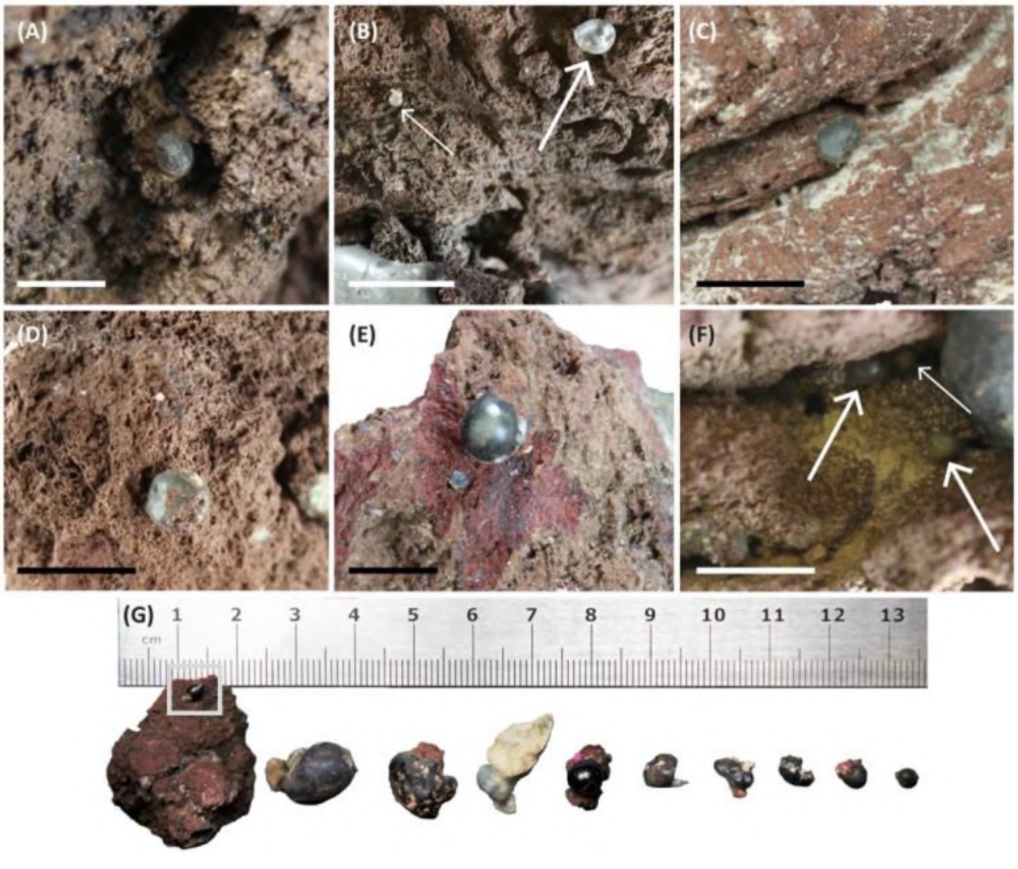

Figure 32: Photograph of achneliths (all scale bars are 5 mm). White arrows point directly to the achneliths. (A) Sub-spherical achnelith. (B) Sub-spherical adjacent achneliths (C) Sub-spherical achnelith within a scoria clast. (D) Entrained particles of scoria on sub-spherical achnelith. (E) Smooth, spherical achnelith. (F) Clustered achneliths within a cavity of a scoria clast. (G) Array of achneliths. Their morphologies range from almost perfect spheroids, to tear shapes (white box) the majority have smooth exteriors, however some are rough with adhered scoria and lithic fragments.

3.3 Contact relations

The contact between scoria clasts and obsidian pyroclasts is sharp (figure 33) and indicates two distinct components which have adhered together without mingling. Lithic clasts have adhered to the obsidian and scoria pyroclasts and occur within the clasts. The obsidian pyroclasts have flowed and infilled vesicles and surface irregularities in the scoria. Some scoria clasts are in contact with the obsidian by only a small percentage of surface area. Typically, the vesicles in the scoria are partially infilled on a microscopic scale (<2 mm) (figure 34). The exteriors of the obsidian are commonly vesicle-free suggesting they chilled before the core of the pyroclasts. Obsidian which is directly in contact with the scoria are often low vesicularity regions (figure 33). Immediately adjacent to this, vesicles in the glass are distorted and preferentially aligned to the margins of entrained scoria clasts.

The majority of the contacts between the two clast types shows no obvious differentiation in the obsidian to the rest of the pyroclast, with the exception of some which show a lighter grey, dull band of obsidian <1 cm wide around scoria clasts (figure 33).

Radial plagioclase growths are present in the scoria at the contact with obsidian clasts (figure 35a:f). Radial growths are the only prominent feature seen between the scoria and glass contact. Scoria edges appear to have disaggregated into the glass. Edges of the scoria clasts which are in contact with the obsidian are defined by a bright, white rim (chain of oxides, figure 36). Some of these surfaces have feathery crystals that appear to have nucleated from the scoria, or parts of scoria have disaggregated into the glass. This feathery texture is a variety of rapid overgrowth similar to spherulites or skeletal crystals.

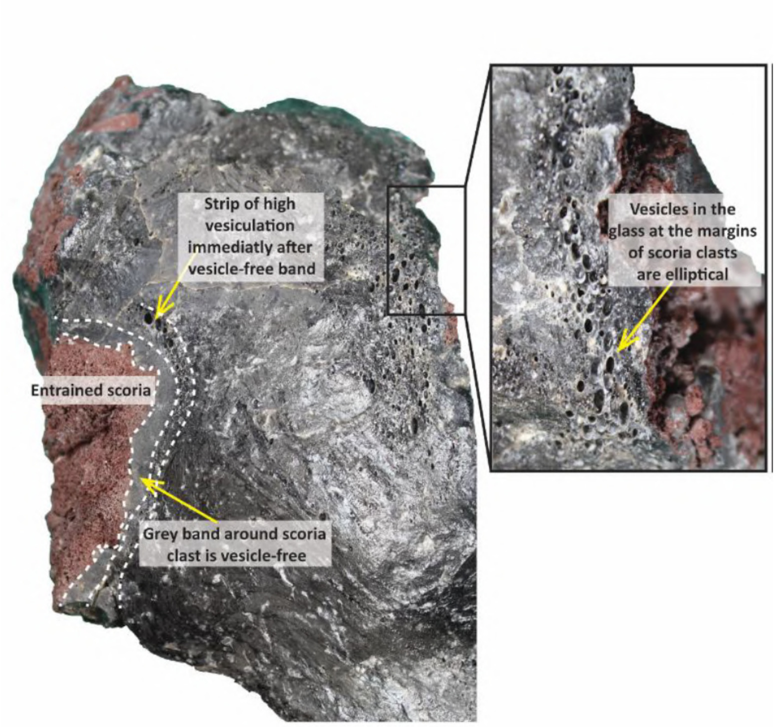

Figure 33: Photograph showing the contact between the obsidian and scoria. The obsidian has a low vesicularity region next to the adhered scoria clast and a strip of aligned ellipsoidal bubbles immediately after this.

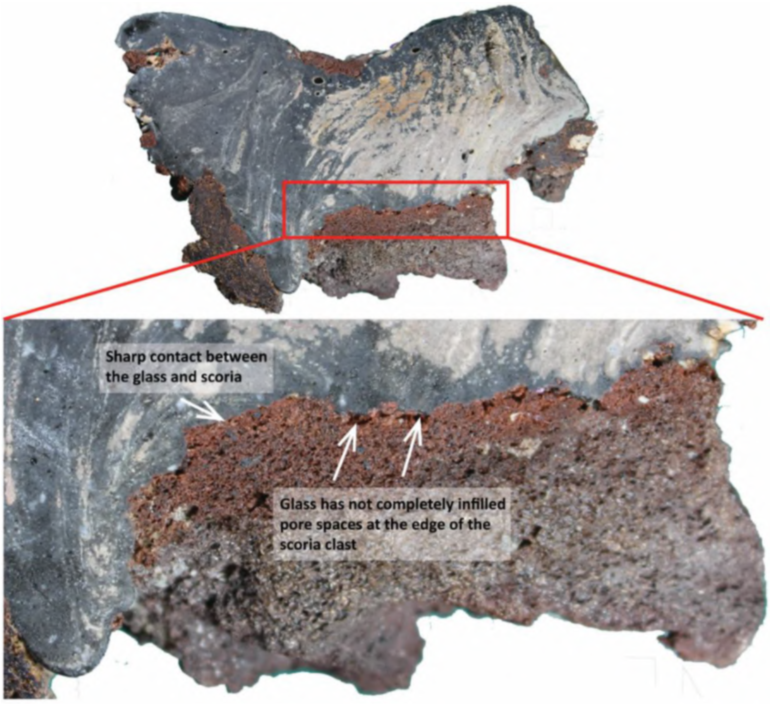

Figure 34: Contact between the obsidian and scoria. The scoria is a brighter red at the contact. Note the glass has not fully infilled the vesicles within the scoria.

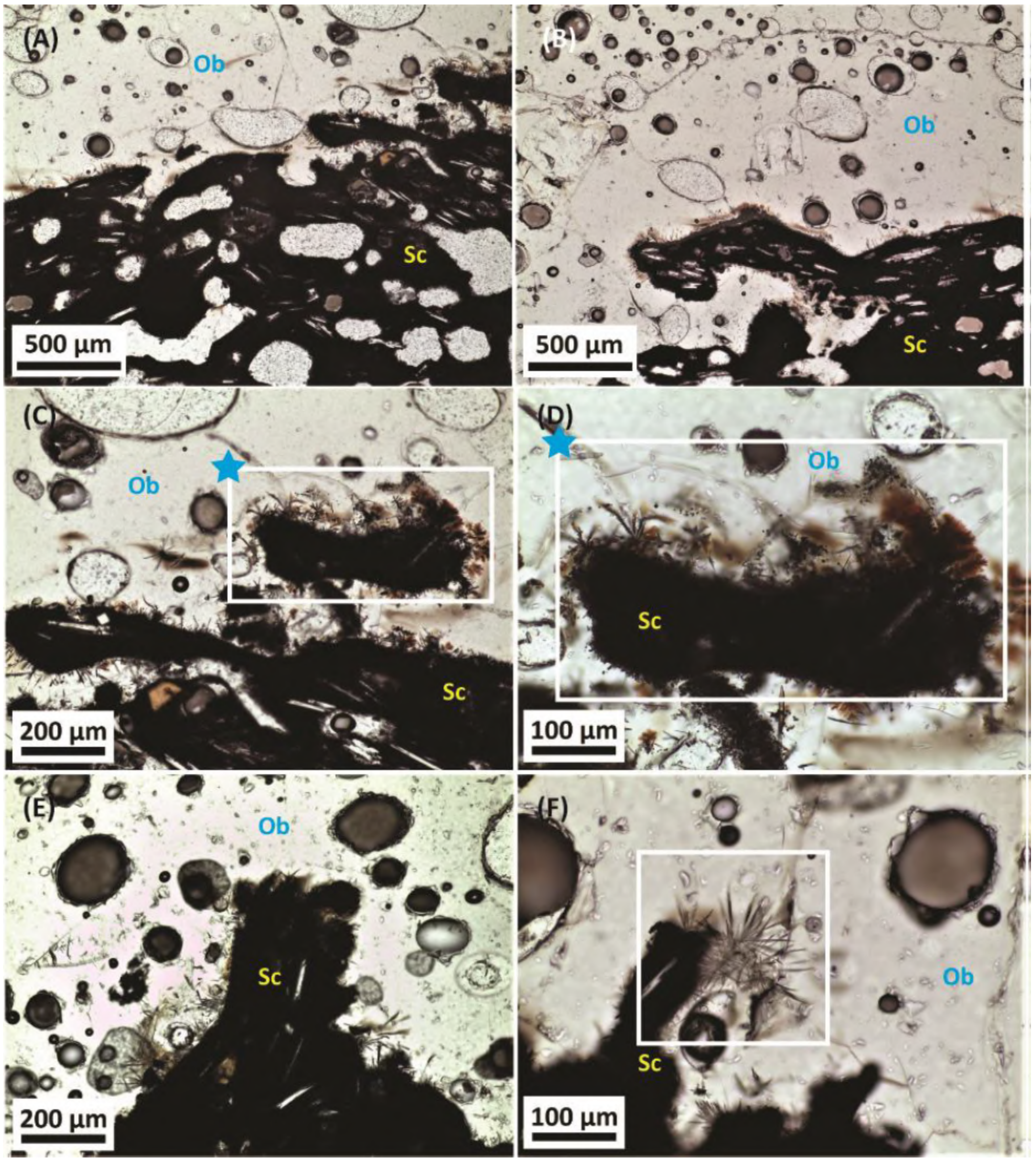

Figure 35: Microphotographs of scoria in contact with obsidian, taken in PPL. Red, feathery radial growths occur at the margins of the scoria. (A) Contact between obsidian (pale yellow) and scoria (balck to brown). (B) Contact between scoria and obsidian. (C & D) Radial growths occur all around the entrained scoria clast. It appears to be overprinted with red oxidation. (F) White box highlights crystal growth which resembles a spherulites.

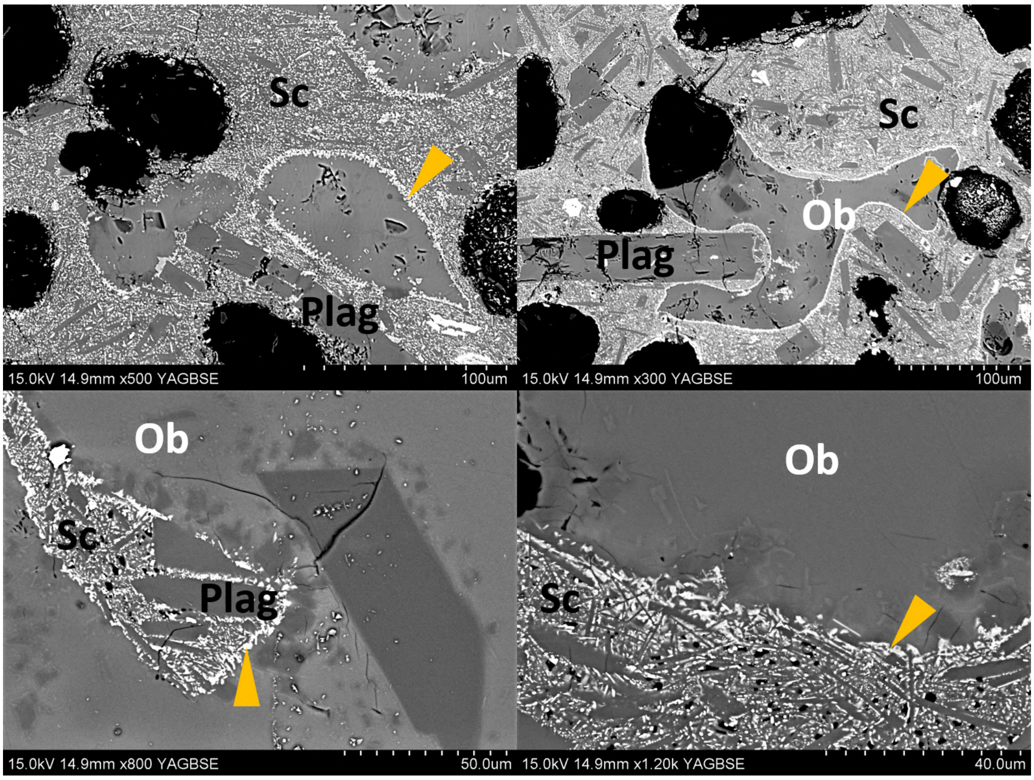

Figure 36: BSE images of the scoria and obsidian contact. The contact typically has a thin (<<10 μm) chain of bright oxides at the edge of the scoria clasts. Black arrow points to oxides. Top BSE images show a bright rim at the contact, which is especially noticable next to plagioclase crystals which appear as a similar shade of grey in BSE.

3.4 Geochemistry

The obsidian pyroclasts plot within the trachyte and rhyolite fields (69 - 73 wt.% SiO_2) although data points dominantly cluster in the rhyolitic field between 71-73 wt.% SiO_2 (figure 37). Sodium and potassium content are moderately high, between 10 and 12 wt.%. In thin section the glass shows little to no alteration suggesting that they are relatively fresh and young samples.The scoria glass is trachy-andesite in composition (55.5-58.8 wt.% SiO_2). Scoria glass and obsidian do not form a continuous compositional trend indicating they are not linked by simple fractionation (figure 41).

BSE microscopy and in-situ geochemistry analysis shows that the obsidian is mostly homogeneous in texture and composition. Some samples have patchy altered glass with heterogeneities in the distribution of feldspar, glass and Fe-Ti oxides. This is further shown by a traverse plot of obsidian and scoria glass (figure 38), as the SiO_2 is compositionally homogeneous across the obsidian, but decreases rapidly at the scoria/obsidian boundary.

FeO, CaO concentrations are higher in the scoria but then decrease at the contact and remain

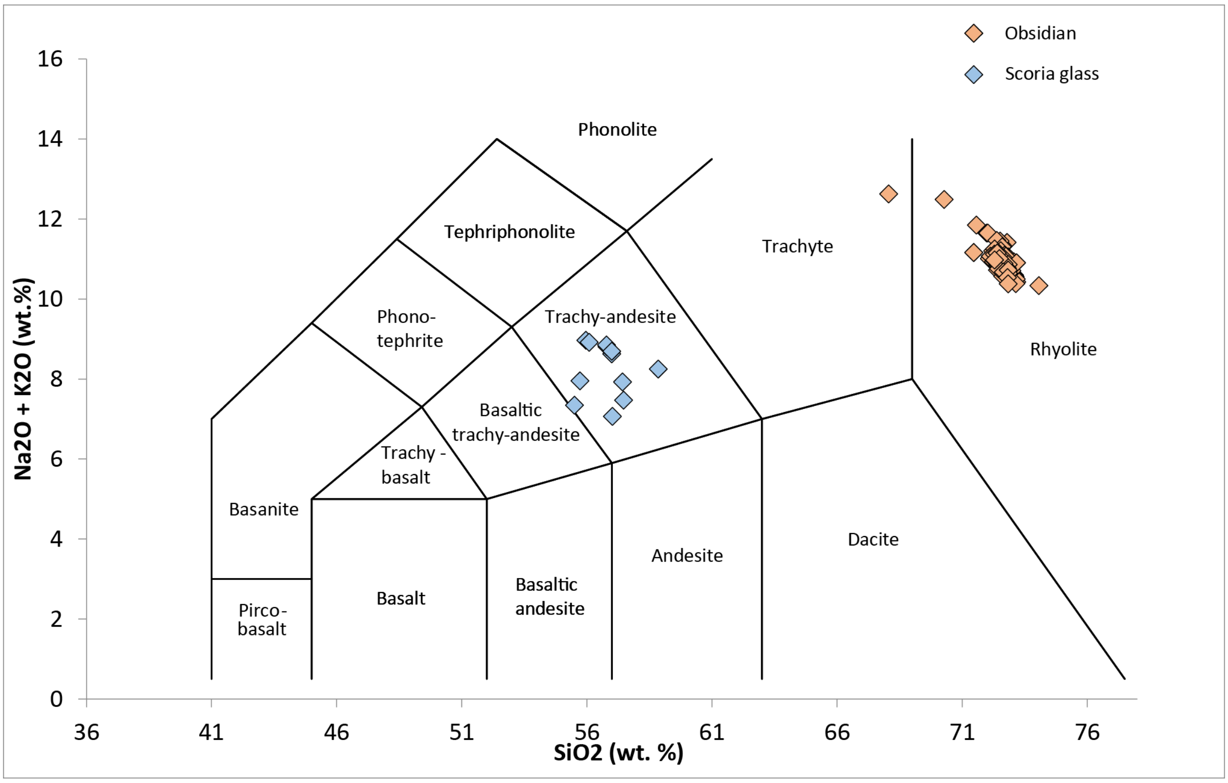

Figure 37: Total alkali vs. silica plot of obsidian and scoria glass.

at consistent compositions in the obsidian. K_2O remains at similar concentrations in the scoria and obsidian, however K_2O decreases at the contact. Al_2O_3 also decreases at the scoria and obsidian contact, but the obsidian has lower Al_2O_3 concentrations.

MgO, FeO, CaO, TiO_2 and P_2O_5 are depleted with increasing SiO_2 in the obsidian. Obsidian has higher amounts of K_2O than scoria but Na_2O concentrations of the obsidian plot within the range on Na_2O concentrations in the scoria. The scoria has a wide range of FeO concentrations (~7.0-9.0 wt.%), CaO concentrations (2.0-7.0 wt.%), MgO concentrations (1.0-3.0 wt.%) and Al_2O_3 (11-19 wt.%) (figure). The scoria and obsidian plot distinctly from one another, with no intermediate SiO_2 data. Al_2O_3 and Na_2O decreases with increasing SiO_2 in the obsidian due to the crystallisation of alkali feldspar. No significant major element variation is recorded in the obsidian and scoria. However the scoria glass data within the harker plots show a wider range, suggesting compositional variance, whereas the obsidian data appears homogeneous through clustering (figure 41).

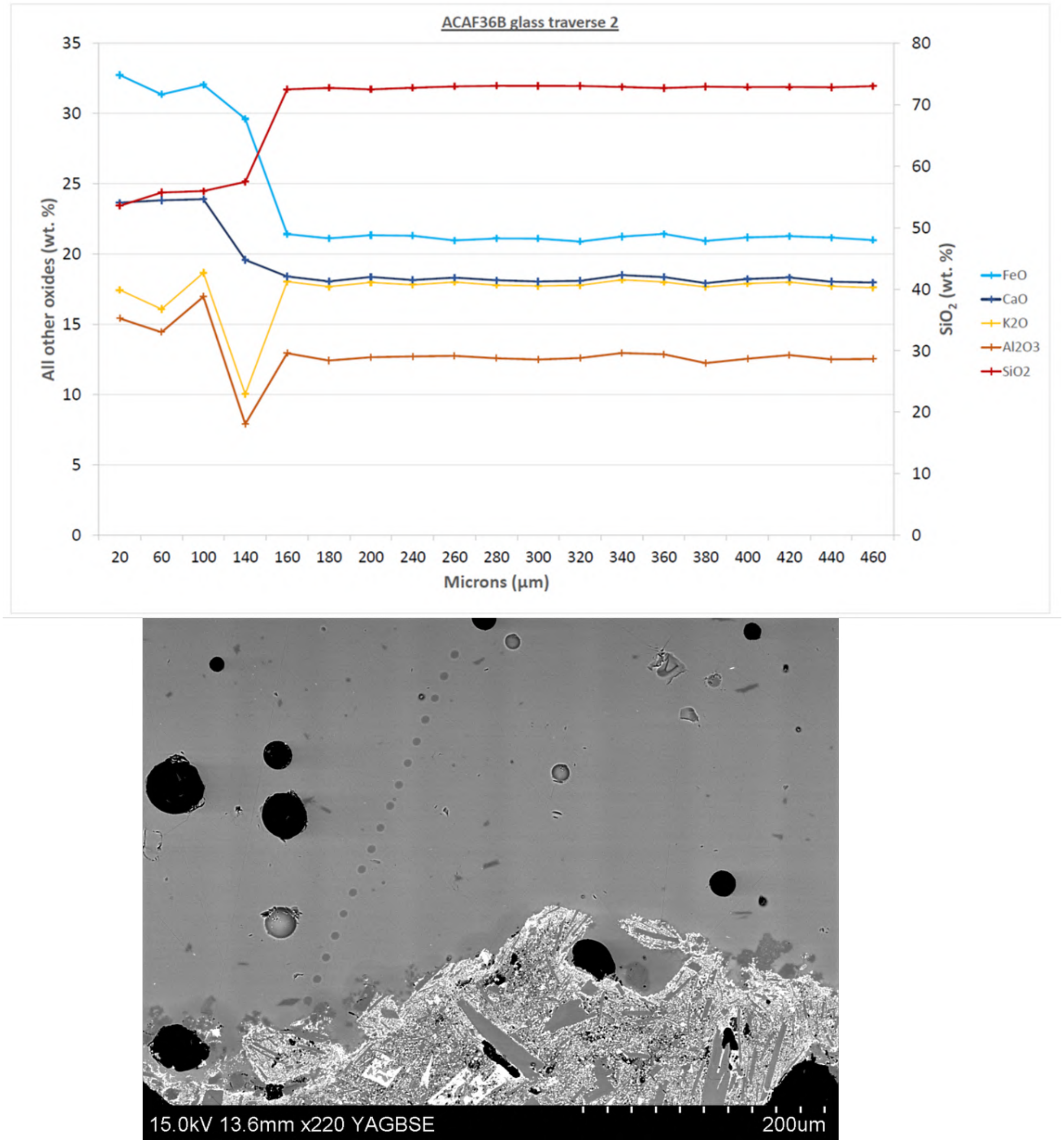

Figure 38: Plot showing elemental changes across a traverse from the scoria contact (A) to further within the obsidian (A). BSE image shows the points measured by EMPA.

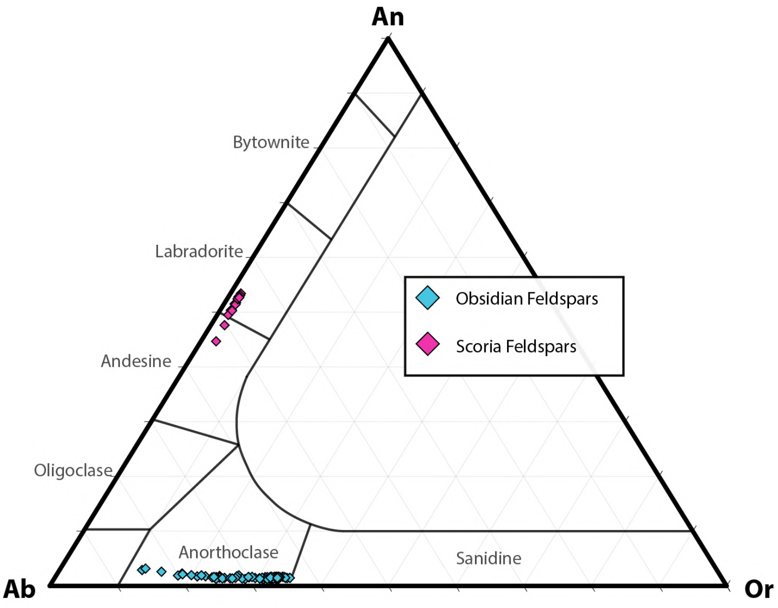

Figure 39: Ternary feldspar compositional plot. Plotted using a tri-plot spreadsheet from David Graham (Loughborough University) and Nicholas Midgley (Liverpool John Moores University).

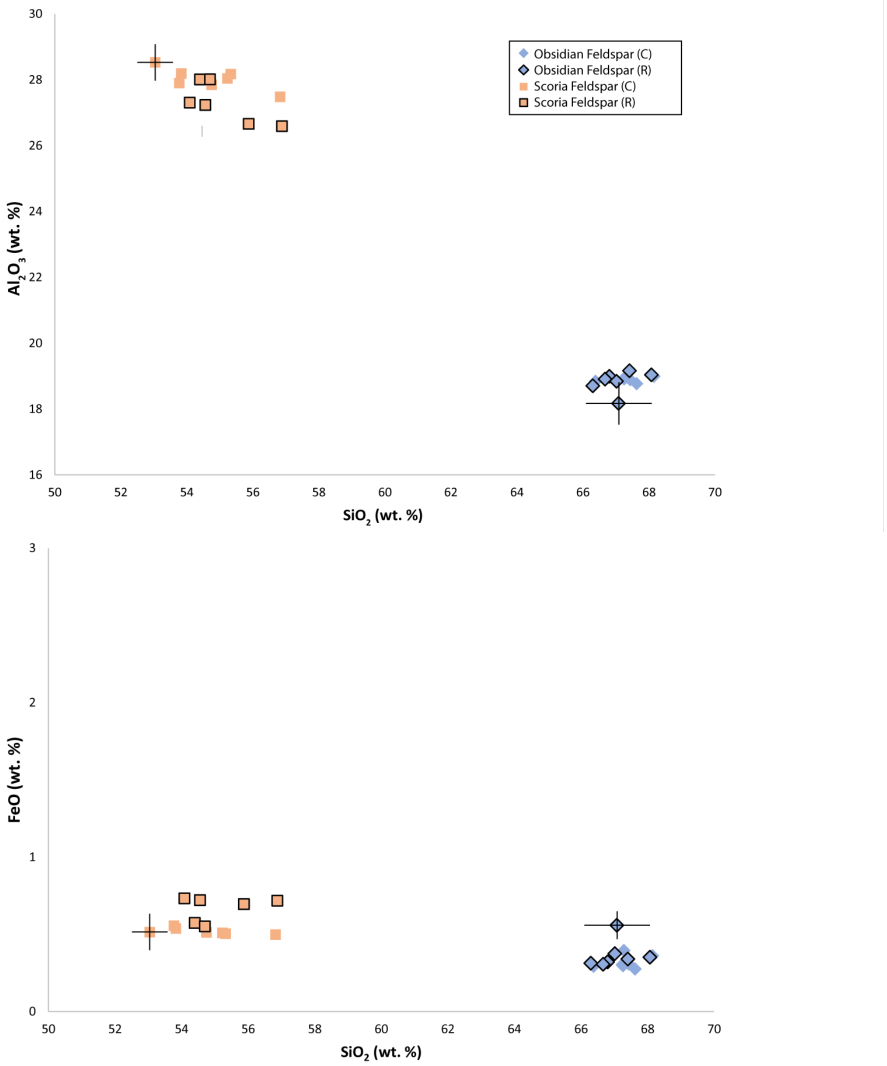

Figure 40: Variation diagrams of feldspars in scoria and obsidian with core and rims distinguished.

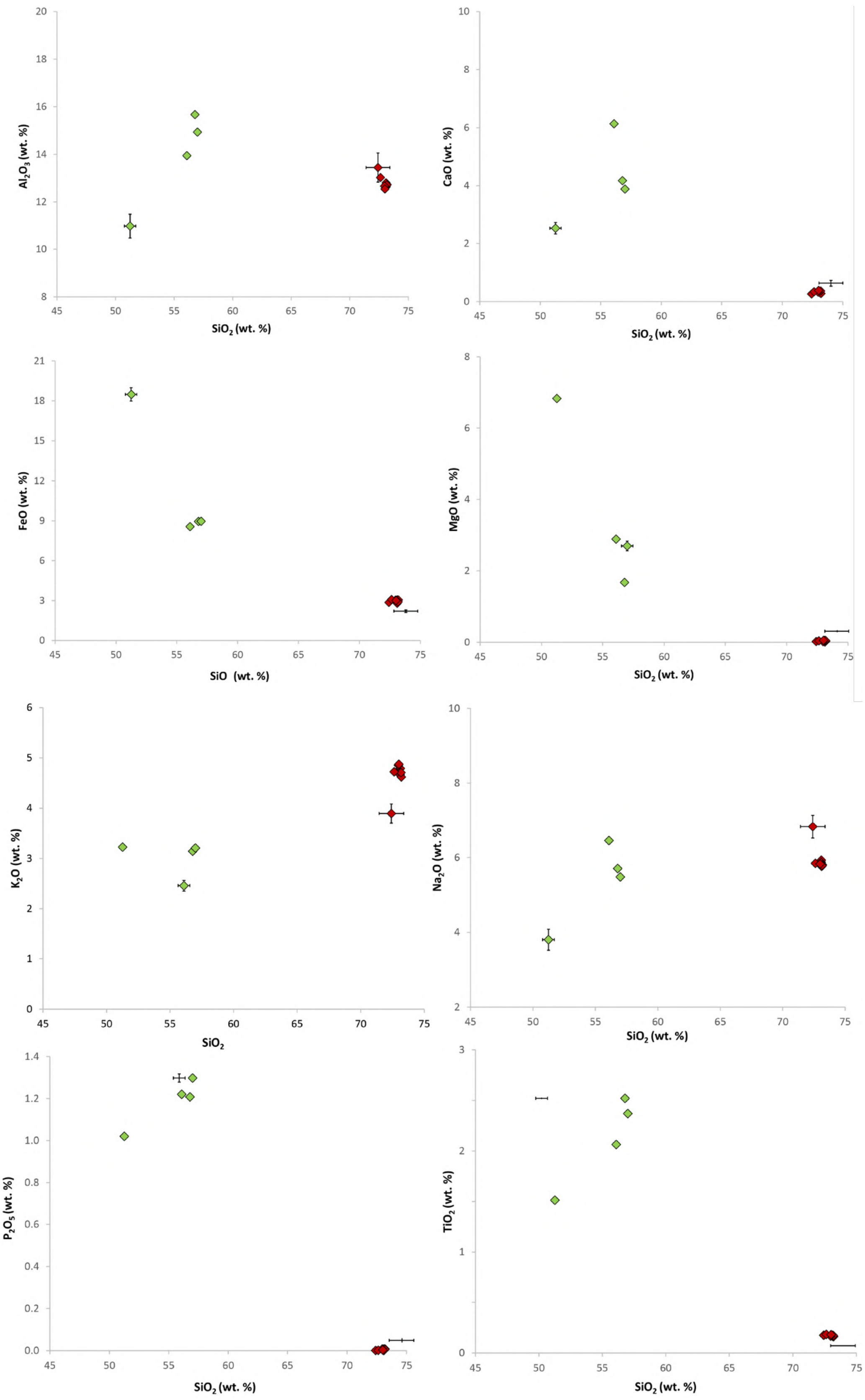

Figure 41: Major element variation diagrams from glass (obsidian) and scoria groundmass glass samples. Analytical uncertainties are showed by bars on each component. Error bars indicate a 2 σ based on reproducibility of SX100 EMPA analyses. TiO_2 error bars are too small to be visible, see appendix for uncertainty.

3.4.1 Mineralogy

Obsidian phenocrysts

Translucent white to pale pink anorthoclase phenocrysts are present in all obsidian hand samples. Anorthoclase is the most abundant phenocryst species which has a compositional range of $Ab_{64\text{-}85}$, $Or_{13\text{-}35}$, $An_{<12}$ (figure 39). The anorthoclase phenocrysts exhibit no systematic differences between the core and rims (figure 40). They occur as euhedral to anhedral phenocrysts, $\sim$ 300 μm to 5 mm in size. The majority of the phenocrysts exhibit simple twinning (figure 43h), although rarely they display visible cross-hatched lamellae (figure 43 b). The anorthoclase is skeletal in shape, but some examples are tabular. Phenocrysts show evidence of breakdown through intense fracturing (figure 47). Anorthoclase phenocrysts regularly occur as glomerocrysts (figure 44). The contacts between crystals are embedded (lying within each other, see figure 44d & e) or by point contacts (joined by one edge of the crystal, see figure 44a). In larger examples, the glomerocryst can be termed closed as there are no voids between individual crystals (figure 44c) (Bennett et al., 2019).

The majority of the phenocrysts (>75%) are externally resorbed, whole phenocrysts can appear to be partially resorbed (figure 42f) or in some cases just one edge of the crystal is resorbed (figure 42b, e, g,& h). In some rarer cases, crystals are internally resorbed (figure 47). The anorthoclase phenocrysts are randomly orientated in relation to the groundmass (figure 43). Anorthoclase phenocrysts are highly fractured (as seen in figure 47). Disaggregated textures are seen in the core of the phenocrysts in BSE (figure 47).

The anorthoclase phenocrysts do not show any chemical zoning and have minimal variations in Al_2O_3, Na_2O and only a small increase in K_2O concentrations within the core of the phenocrysts. However, microphotographs of anorthoclase in cross polarised light show slight reverse zoning (figure 42a, c, f & h) with an increase of An% towards the rim, however the increase is only minimal (2.5 %). The anorthoclase show growth inclusions that are typically aligned along the fractures within the crystal. Mineral inclusions occur along fractures and sometimes the edge of the phenocryst, defining its shape.

There are a few phenocrysts in the obsidian where the rims have a nucleated overgrowth, suggesting they were not stable within the glass. The texture is graphic-like (an intergrowth of two minerals resembling runic writing) with scattered Fe-Ti oxide microlites, shown by bright patches and ends with a black flower-like rim around the overgrowth (figure 45).

Throughout the sectioned obsidian clasts, patches of microlites (feldspar and Fe-Ti oxide in composition) which resemble xenocrysts are occasionally present (figure 46). However, due to their approximate tabular shape (figure 46a, b & c) they could be considered as crystal relicts of phenocrysts which have disaggregated.

Minor amounts of clinopyroxene microphenocrysts are present, however they were too small to identify during EMPA analyses. Clinopyroxene is present as small subhedral phenocrysts (<1 mm) and as discrete, subhedral microphenocrysts (figure 42 i-l). In plane polarised light (PPL) a brown halo is seen within the glass immediately surrounding the clinopyroxene (figure 42l). Poorly developed spherulites are rarely visible (figure 44f).

Scoria mineralogy

Phenocrysts in the scoria show a continuum between labradorite to andesine (An_{36-53}, Ab_{45-57}, $Or_{1.5-5}$), ranging between 200 and 700 μm in diameter (figure 39). They show preferential orientation to vesicles.

Microlites

Microlites (<100 μm) in the groundmass of the obsidian are acicular to narrow lath-shaped crystals. The microlites were too small to obtain in-situ major and minor element analyses but appear similar to phenocrysts, therefore may be alkali feldspars. The microlites are frequently aligned in the same orientation of elongated bubbles or around the edges of phenocrysts. Obsidian microlites are less abundant and distinct than microlites found in the scoria (figure 15, 42, 43, 44). Plagioclase microlites in the scoria have a homogeneous compositional range of $An_{41}Ab_{56}Or_3$ to $An_{46}Ab_{52}Or_2$ comparable to the phenocrysts (figure 39). They show no preferential alignment in the scoria.

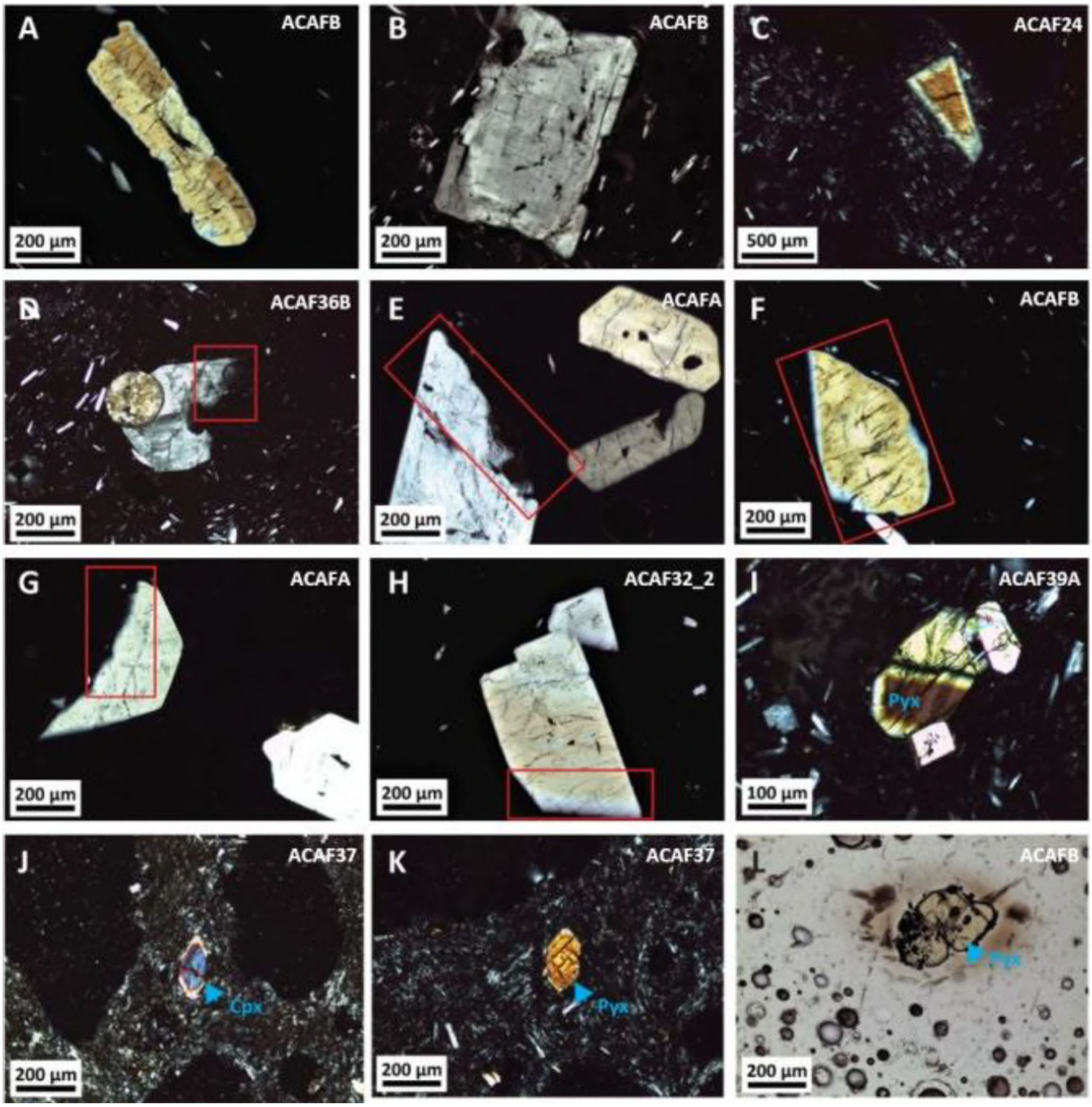

Figure 42: Microphotograph of phenocrysts in obsidian (A-K taken in cross polarised light, XPL, L taken in plane polarised light, PPL). Sample number can be found in the top right corner of each microphotograph. (A) Twinned anorthoclase phenocryst. The edges are slightly resorbed. (B) Subhedral anorthoclase phenocryst with visible cross-hatched lamellae. (C) Reverse zoning in the anorthoclase phenocrysts. (D-H) Anorthoclase phenocrysts with resorbed edges. (F & H) Show slight reverse zoning. (I-K) Euhedral clinopyroxene microphenocrysts. (L) Clinopyroxene phenocryst with a brown halo surrounding the crystal in the obsidian.

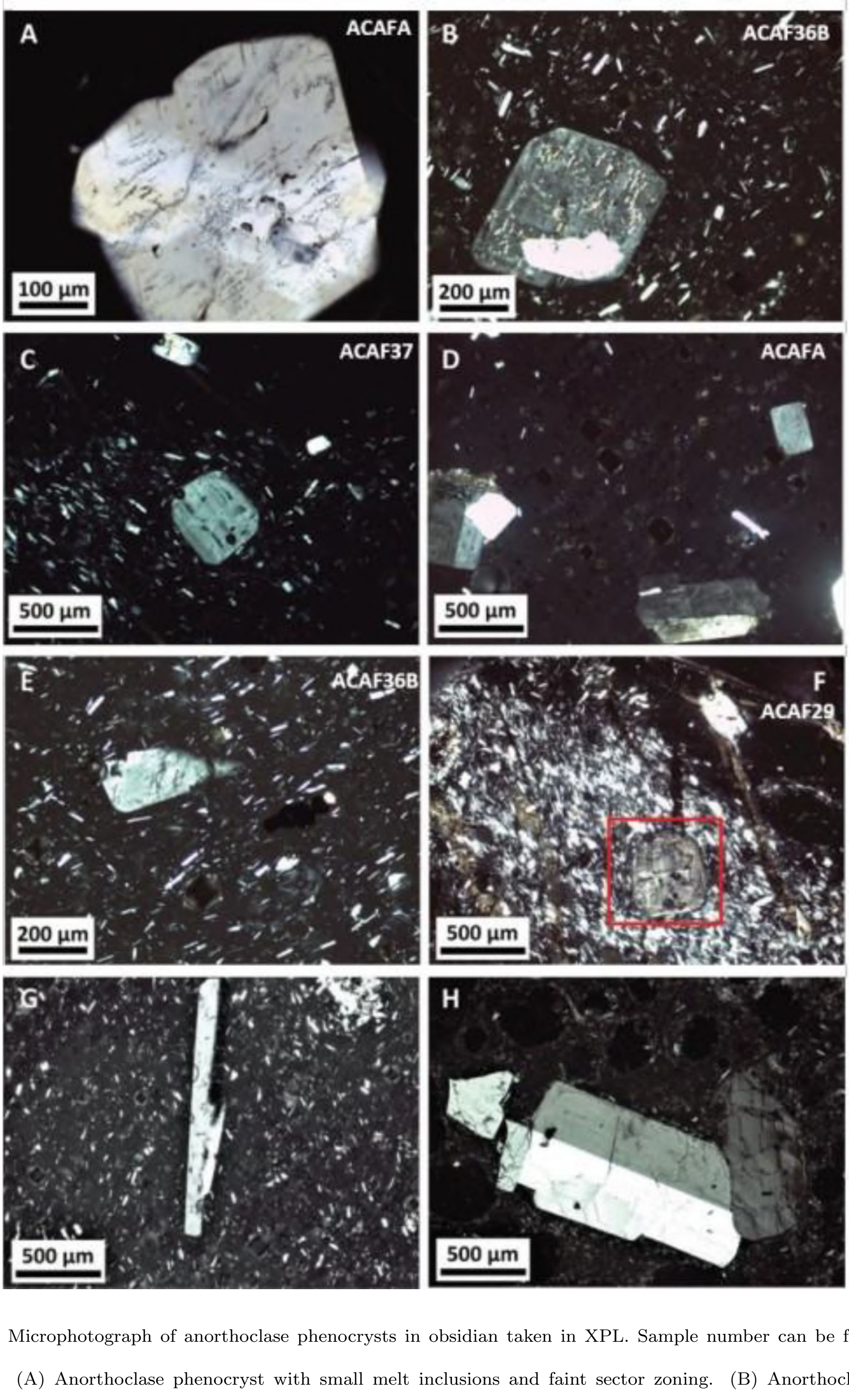

Figure 43: Microphotograph of anorthoclase phenocrysts in obsidian taken in XPL. Sample number can be found in the top right corner. (A) Anorthoclase phenocryst with small melt inclusions and faint sector zoning. (B) Anorthoclase phenocrysts with parallel mineral inclusion. (C) Subhedral anorthoclase phenocrysts with microlites aligned around the crystal edges. (D) Anorthoclase phenocrysts. (E) Resorbed anorthoclase phenocryst. (F) Anorthoclase with visible cross-hatched lamellae in altered glass. (G) Skeletal anorthoclase phenocryst. (H) Anorthoclase phenocryst showing simple twinning.

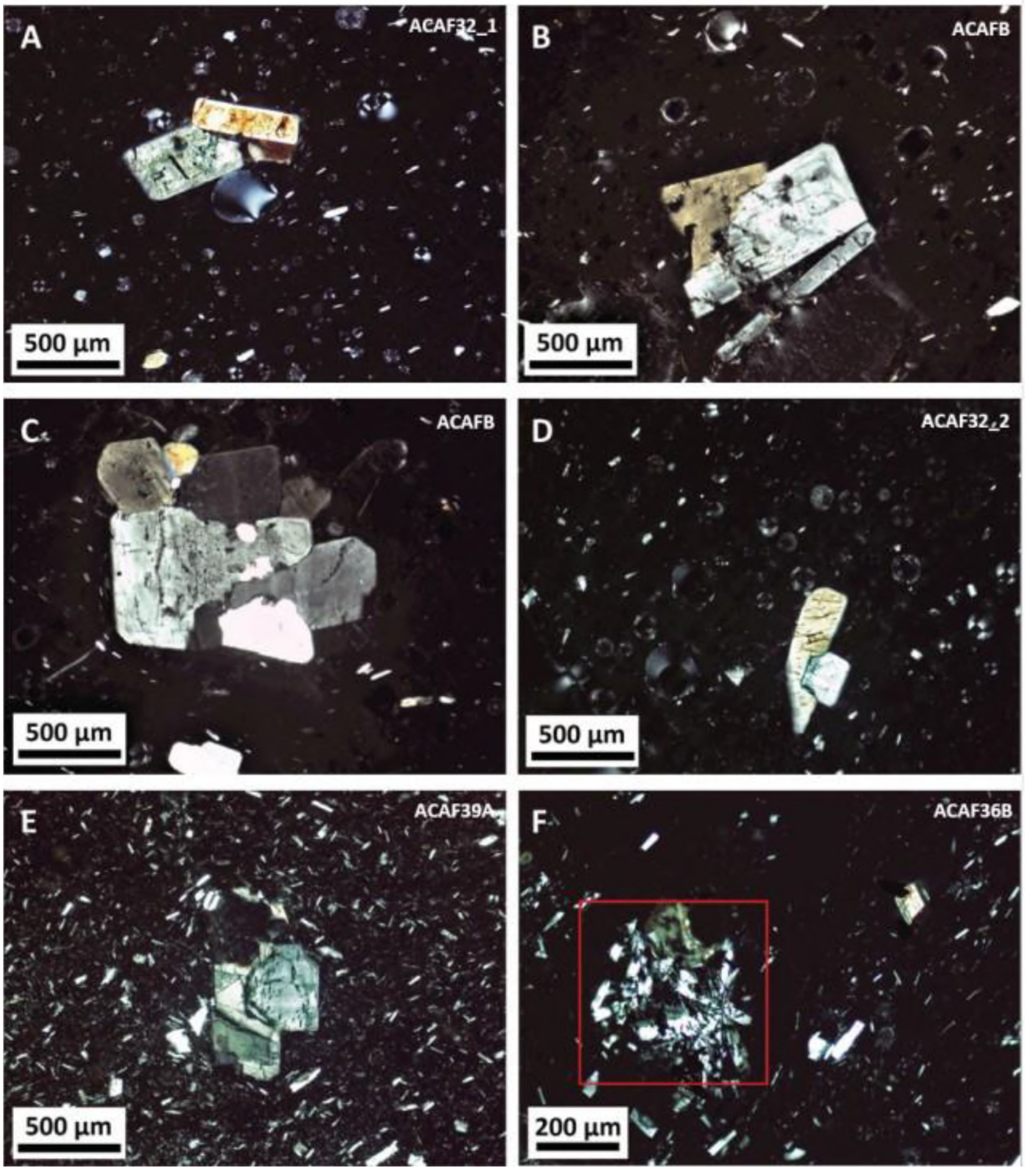

Figure 44: Microphotographs of glomerocrysts taken in XPL. Sample number can be found in top right corner. (A) Glomerocryst of anorthoclase crystals in point contact. (B) Glomerocryst with a fractured anorthoclase phenocryst. (C) Large glomerocryst which shows no voids between the crystals. (D & E) Glomerocryst of anorthoclase with embedded contact. (F) Radial plagioclase crystal resembling a spherulite (red box).

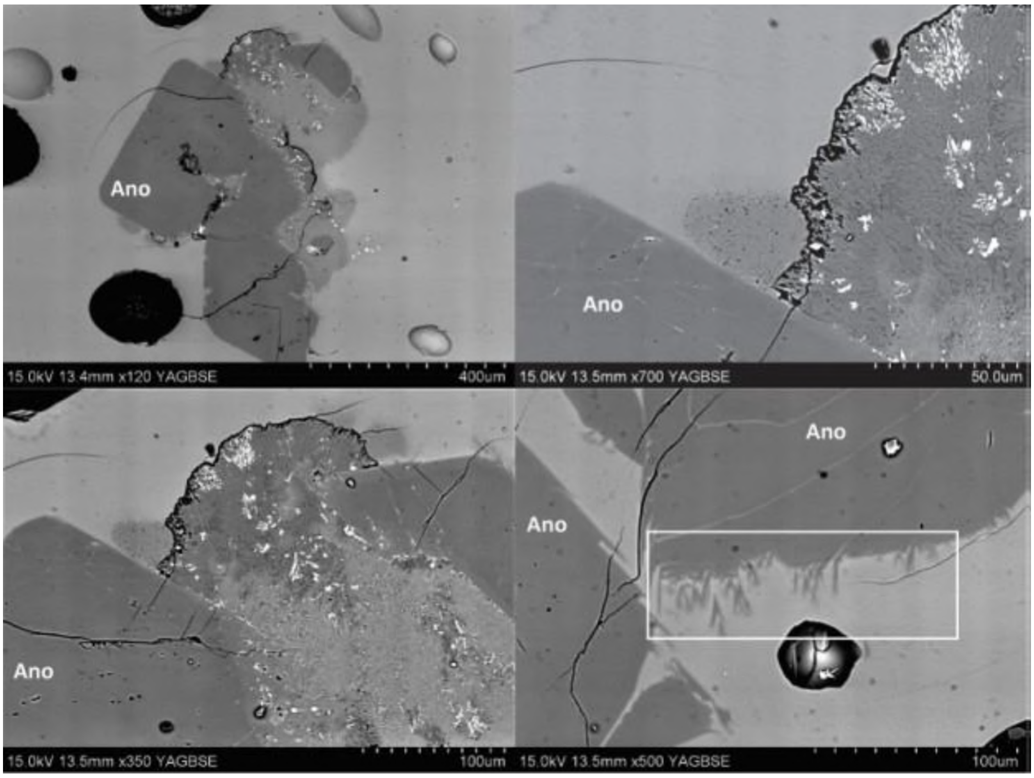

Figure 45: BSE images showing anorthoclase phenocrysts in disequilibrium. (A, B & C) Graphic-like texture radiating from the edge of an anorthoclase phenocryst. (D) Radial feather-like crystals radiating from the edge of an anorthoclase phenocryst (white box).

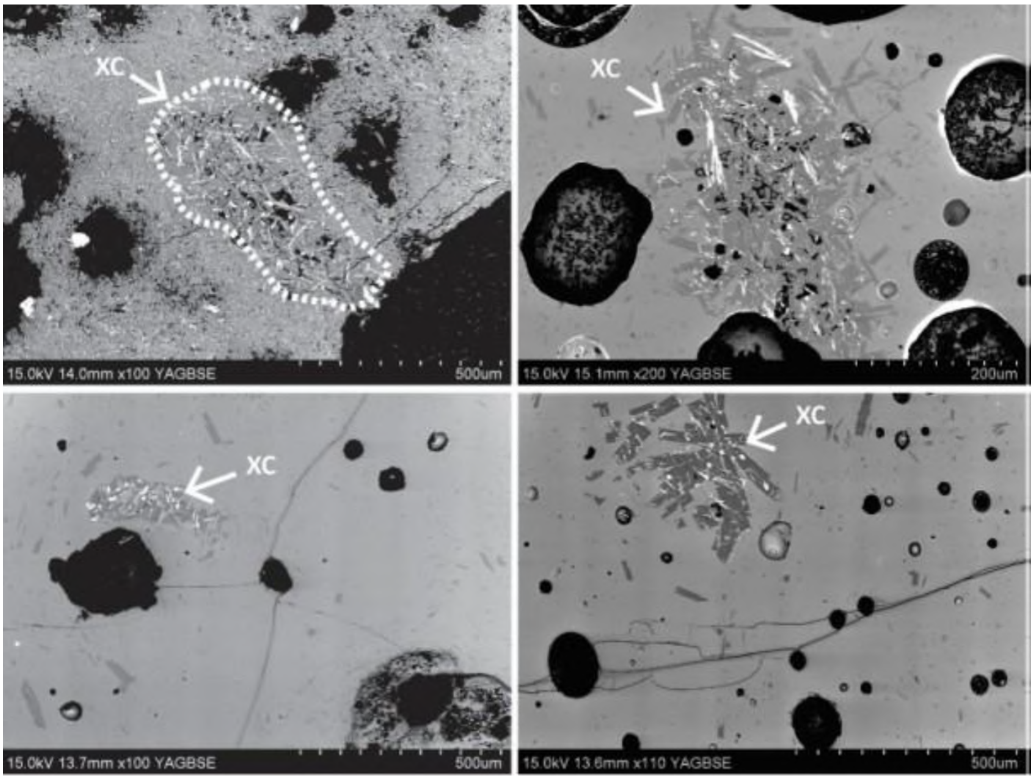

Figure 46: BSE images of potential xenocrysts found in the obsidian or crystal relicts of broken-down phenocrysts. They are composed of Fe-Ti microlites (white, elongate crystals in BSE) and feldspar microlites.

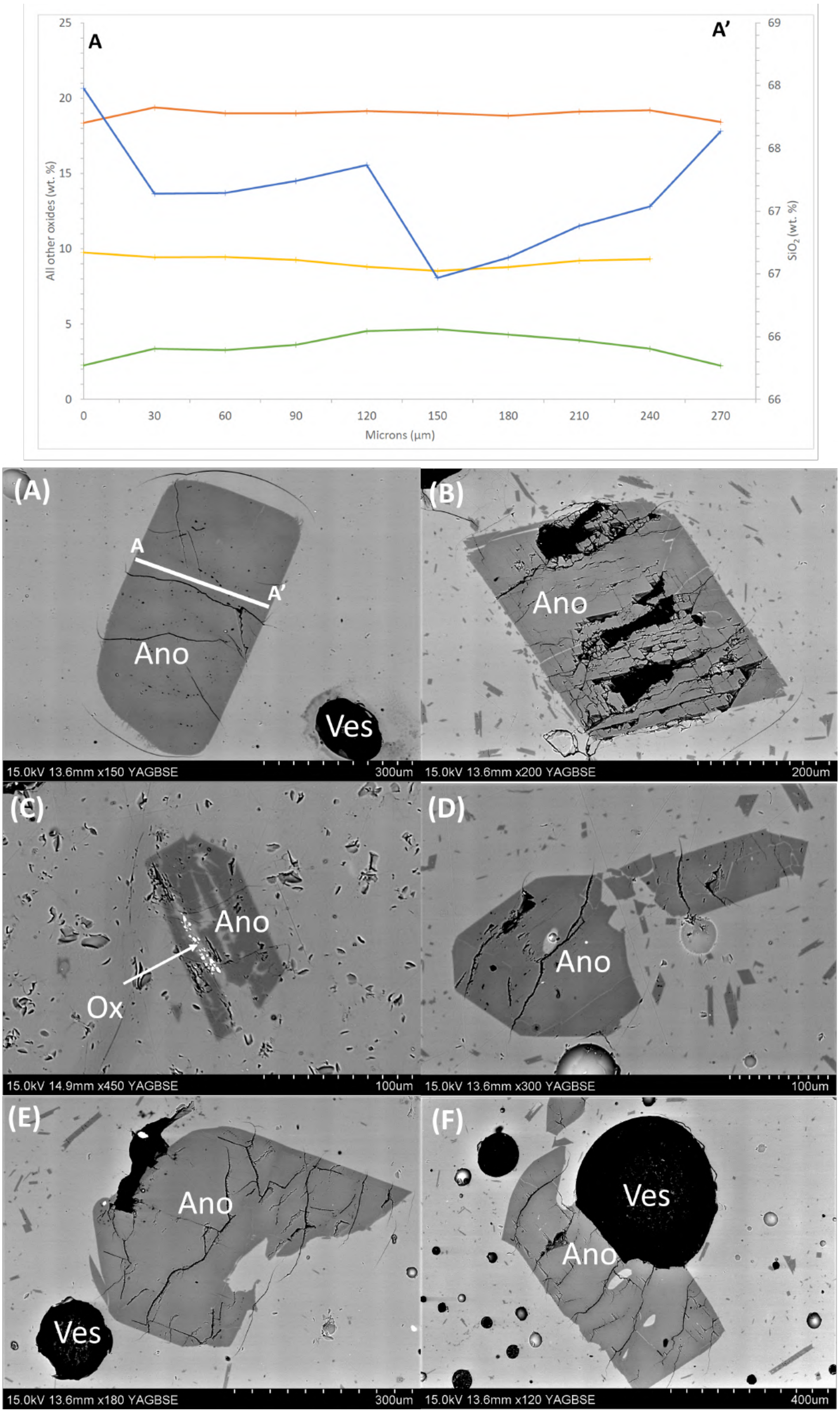

Figure 47: BSE images of anorthoclase phenocrysts. (A) Subhedral anorthoclase phenocryst. A-A’ represents probed path of major and minor trace elements during EMPA analyses. (B) Phenocrysts which show breakdown through intense fracturing. (C) Anorthoclase phenocryst with internal resorption. Cluster of oxides (shown by bright white) have formed in a resorbed region of the phenocryst. (D) Highly fractured anorthoclase crystal. (E) Resorbed edge anorthoclase phenocryst. (F) Nucleated phenocryst on a bubble. Ano: Anorthoclase. Ves: Vesicle.

Iron-titanium oxides

Rare magnetite and ilmenite occur as small (<1mm) microphenocrysts in the obsidian. Unexsolved magnetite oxides have a homogeneous composition of 23 wt.% TiO_2, 0.02 wt.% Cr_2O_3, 66 wt.% FeO, and homogeneous ilmenite oxides have a composition of 46 wt.% TiO_2, 0.01 wt.% Cr_2O_3, and 44.0 wt.% FeO (see appendix).

4 Interpretation

4.1 The fissure eruption

A small-volume, monogenetic fissure resulted in the co-eruption of two distinct magmas. The total erupted volume was approximately <0.001 km^3 with the obsidian pyroclasts accounting for only <<0.005% (<0.0007 km^3) of the deposits. The low erupted volume of the obsidian suggests that the obsidian pyroclasts are from a limited magmatic source or are not efficiently incorporated into the eruption column. Due to the accumulation of scoria into ramparts, it is inferred that the eruption was a weak Hawaiian fire-fountaining event.

4.2 Stratigraphy

The ramparts overlie a rhyolitic lava breccia which is interpreted as an explosion breccia. The orange weathered surface on the rhyolitic lava indicates a hiatus between felsic volcanism and mafic fissure (figure 13). The fissure cuts through the underlying felsic lavas and has erupted a small volcanic sequence of welded to non-welded scoria, spatter and scattered, co-erupted obsidian. Lithic lapilli and blocks of rhyolitic lava are scattered throughout the ramparts. They are found externally adhered or entrained within scoria and obsidian pyroclasts (figure14c; figure 17). Lithic fragments were likely ripped up from the conduit walls during the eruption and then mechanically incorporated into the erupting lava.

4.3 Pyroclasts

4.3.1 Scoria

The scoria clasts formed ramparts which line the fissure. The scoria clasts are angular and vesicular suggesting a gas-rich eruption and explosive fragmentation of basaltic-intermediate magma. Labradorite and andesine phenocrysts in the scoria do not show physical breakdown, chemical zonation or resorption (figure 15) implying they were in equilibrium within the melt in which they formed and remained in equilibrium during ascent.

4.3.2 Obsidian pyroclasts (AOPs)

The Ascension obsidian pyroclasts (AOPs) were erupted hot and ductile, and landed within the scoria fall deposit. Irregular, fluidal morphologies result from the percolation and pooling in pore spaces within the underlying scoria, implying that the obsidian had unusually low melt viscosities on eruption, which were sufficient to induce ductile deformation post-deposition. Typically, low viscosities are associated with low silica content, high temperatures (1000-1200°C [Taddeucci et al., 2015]) and are basaltic (Sumner et al., 2005). However, here the obsidian is rhyolitic (figure 37) despite having fluidal textures which are comparable to low viscosity basaltic lava (i.e. pahoehoe lava: figure 26). The structural relaxation time of any given melt is a function of its viscosity; low viscosities result in longer relaxation times before reaching the glass transition temperature, where they become solids (Clarke et al., 2019). The viscosity of the obsidian pyroclasts on eruption was low enough to prolong structural relaxation times, and resulted in levelled out tops of obsidian clasts with the scoria ramparts (figure 22). Low viscosity rhyolitic pyroclasts observed at the Main Ethiopian Rift (figure 48) often have a chilled exterior (Clarke et al., 2019), which is glassy and less vesiculated (i.e. bread-crust) than their interiors. AOPs do not have chilled rind. However, surface folds and ropes on their exterior suggests that the surface has begun to slightly quench before the interior. Further, morphologies seen within the AOPs, such as pendant drops and stretched filaments, suggest they were more fluidal (than the similar erupted clasts at the Main Ethiopian Rift) as they landed on the scoria.

Fragmentation of gas bubbles at the free surface of a vent can be recorded in pyroclasts which are usually angular, reflecting brittle breakage (Cashman and Scheu, 2015). AOPs lack any evidence of brittle breakage (with exceptions of brittle fractures which have formed after the glass solidified), therefore fragmentation had a negligible influence on the final pyroclast morphologies.

During fallout of the fountain, AOPs morphologies were governed by surface tension, friction and viscous forces. But these parameters had little influence on the final morphologies of the clasts as they continued to behave fluidly on impact, therefore they cannot be characterised as aerodynamic bombs (e.g. ribbon, rotational, spindle, fusiform and spherical bombs) or expanding bombs (e.g. bread-crust

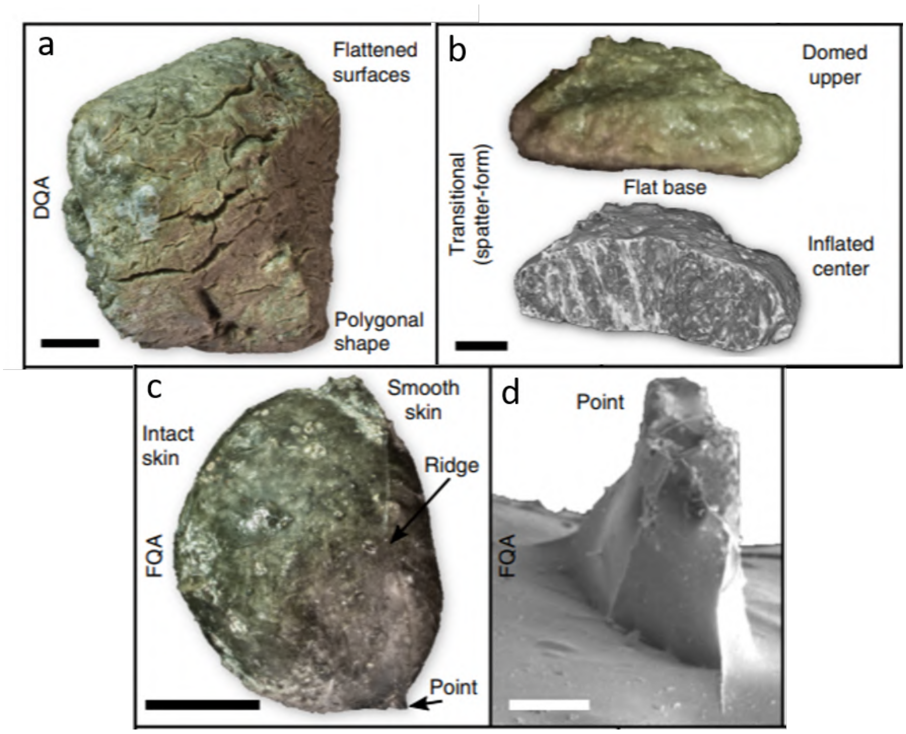

Figure 48: Fluidal pyroclasts erupted from a Caldera in the Main Ethiopian Rift. Taken from Clarke et al., 2019. The pyroclasts emulate those erupted from Ascension Island, particularly due to features such as the oblate morphology (b), smooth skin, ridges (c), and extruding points (d). Which can be seen in figures 21, 22 & 23. Scale bar is 5 mm for (a) and (c), 1 mm for (b) and 200μm for (d).

and exploding bombs), with the exception of some non-idealised clasts (figure 21) which had begun to quench in flight forming oblate shapes. Generally, two end-member regimes are seen in AOPs: (1) oblate, sub-spherical pyroclasts which lack fluidal textures and (2) irregular, polygonal pyroclasts with fluidal textures. The distinction of these two pyroclasts appears to be a result of cooling during fallout or on deposition. Those which quenched on deposition have cowpat-like bomb morphologies: i.e. they landed and spread laterally, entraining larger clasts on the base. An endmember of the pyroclasts is the cuboid-shaped clast (figure 21f & g), which lacks post depositional flow features. Fluidal bombs which deform during fallout typically become spherical (Porritt et al, 2012), however the cuboid-shape obsidian has sub-parallel sides and edges which meet at almost at 90°. Therefore, another mechanism likely formed this clast when the viscosity of the obsidian was higher, enabling the shape to form as the obsidian passed the glass transition temperature. One hypothesis is that it was formed from the fragmentation and bursting of a large gas bubble. Other bombs lacking fluidal features may indicate the effects of a longer travel-time path, resulting in a higher viscosity on deposition. AOPs final morphologies are inferred to be mostly controlled by, and restricted to, the cavities and pore spaces into which they flowed. Hence, the final pyroclast shapes are a result of viscous deformation and flow within the scoria ramparts. Some clasts have unusual rough surface textures where the obsidian has parallel ridges (figure 26). These textures, alongside the presence of frozen vesicles (figure 49) suggest that the obsidian was degassing on deposition.

Figure 49: Large frozen vesicle on the surface of an AOP. Scale bar 3 cm.

Depending on the viscosity of the pyroclastic ejecta, a number of different outcomes can occur for a clast impacting the ground. Chilled/highly viscous magma can undergo brittle fracture, or rupture of a brittle skin, while less viscous clasts undergo folding or splashing (see figure 50: Sumner et al., 2005). Through a combination of field studies, analog experiments and fluid dynamics, Sumner et al., (2005) determined the factors controlling the deformation and agglutination of spatter, a low viscosity pyroclast which often accumulates on scoria ramparts. It was concluded that spatter will undergo splashing if clasts fell from the fountain at terminal velocity, are >10 cm in diameter and have magma viscosities up to 10^5 Pa.s.

Ductile fractures are only found on larger clasts of AOPs, therefore the ductile deformation was likely due to the viscous flow of the clasts as they spread, and stretched over the scoria clasts. The glass filaments suggest that the relaxation time of the clasts was long enough for threads to form, but

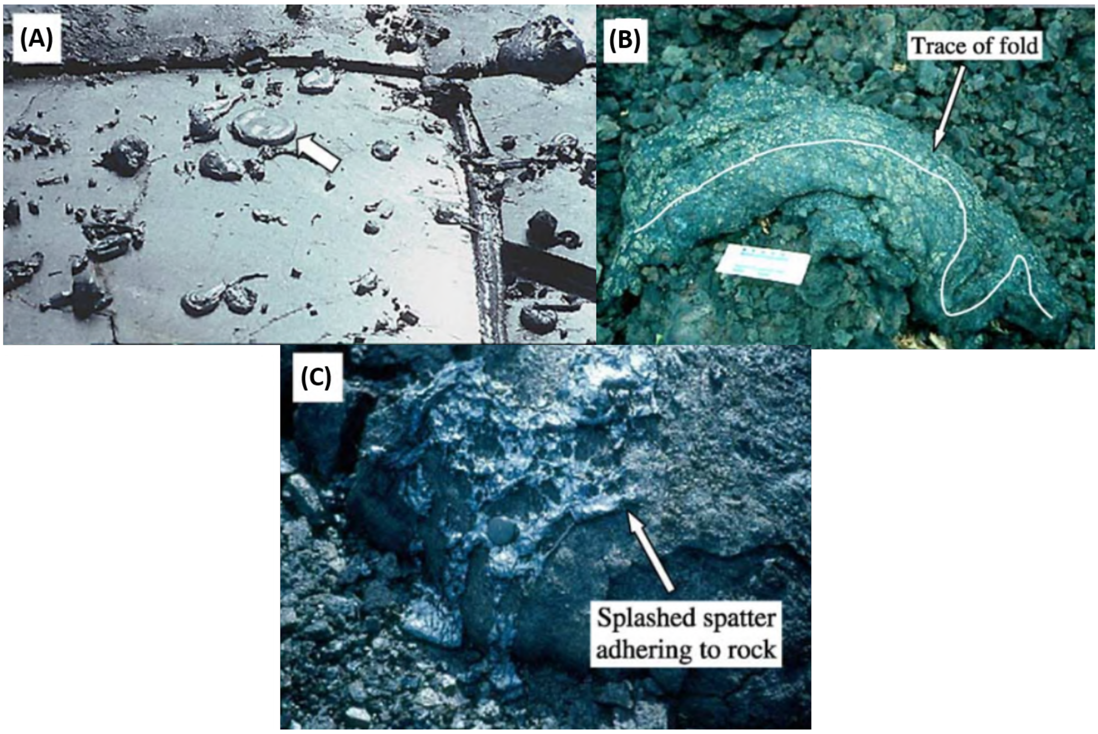

Figure 50: (A) Spatter droplets found on Kilauea (arrow pointing to a droplet approximately 10 cm in diameter). (B) Folded bomb from the 1986 eruption of Izu-Oshima, Japan. (C) Splashed spatter from Hawaii. When comparing these clasts to AOPs, it is clear that AOPs did not undergo splashing as AOPs typically appear to exhibit morphologies that show the clasts enveloping underlying scoria clasts, which reflects rim folding seen in figure 26. Therefore AOPs were either not falling at terminal velocity, had higher viscosities of 10^5 Pa.s or a combination of the two. Taken from Sumner et al. (2005).

short enough cross the glass transition temperature and freeze during stretching.

Vesicles within the AOPs show heterogeneity across samples, but are the pyroclasts are typically dense, with low vesicularities. Vesicle regions in AOPs are characterised by: (1) bubble-free obsidian, (2) by containing relatively high bubble number densities of small (<100 μm) groundmass bubbles or (3) containing large (~700 μm) and coalesced bubbles. Large bubbles frequently show elongation and are mostly found in proximity to the scoria contact. These could be late-stage bubbles which have nucleated due to impact on the scoria rampart (Rothery et al., 2007). Most bubbles within pyroclasts are a mixture of those that exsolved during ascent from depth and/or during shallow storage and those which formed during the eruption process (Sparks and Brazier, 1982; Mangan et al., 1993; Blower et al., 2002). However, bubbles may form upon impact, as the ground (scoria rampart) releases confining pressure in the bomb interior, allowing a new episode of nucleation and/or bubble growth, or the shock of impact acts as stimulus for nucleation and/or growth (Rothery et al., 2007). This is evidence by vesiculation at the scoria/obsidian contact (figure 33). Larger bubbles can sometimes show slight distortion into ellipsoids, which is likely a result of flow of the obsidian after impact. During this, quench time is short enough to prevent elongate vesicles from relaxing into spheres but long enough for suspended drops to form.

4.3.3 Achneliths

Achneliths are associated with small, subaerial, monogenetic eruptions of basaltic magma (Eaton and Murata, 1960; Richter et al., 1970; Porritt et al., 2012; Snchez et al., 2016). Spherical, to sub-spherical achneliths from Hawaiian eruptions are termed Pele's tears (Heiken, 1972; Parfitt, 1998; Moune et al., 2007; Stovall et al., 2010; Porritt et al., 2012) and result from relatively low eruption velocities (Shimozuru, 1994). Although most achneliths are basaltic in composition, Pele's tears exhibit a wide range of chemical variability, 47-98 wt. % SiO_2 (Lefvre et al., 1986). Their tendency to form spherical to sub-spherical shapes is strongly dependent on friction, surface tension and magma velocity, as well as low viscosities (Shimozuru, 1994). The achneliths found in the scoria ramparts resemble basaltic Pele's tears and spheres, therefore likely had similar viscosities (<100 Pa.s) despite being rhyolitic in compositions. Rhyolite magmas typically have viscosities between 10^{12} and 10^5 Pa.s (up to 11 orders of magnitude higher than basaltic viscosities).

Secondary fragmentation (shearing and extension of fluids, or collision and abrasion of solids reducing particle size [Cashman and Scheu, 2015]) of larger volumes of the rhyolitic melt which was entrained in the inner, hot portion of fire-fountains (Snchez et al., 2016) may have formed the sub-spherical achneliths seen on Ascension Island. Splashing of low viscosity magma can produce parent droplets and in turn, daughter droplets, or 'achneliths' (described by Sumner et al. (2005) following a series of laboratory and analog experiments). Splashing can generate droplets by numerous mechanisms (see figure 51, d-f). However, as AOPs viscosities are likely not low enough to provoke splashing (see figure 50), they must have undergone simple deposition (figure 51, a-c), which is reflected in figures 20, 21, 26. Further, it can be inferred that there was not enough time for the spheres to attain spherical shapes before impact. Therefore the achneliths seen throughout the Ascension fissure deposits were likely a result of fragmention within the fire-fountain (figure 52).

The respective size difference between the large obsidian clasts and achneliths result in distinct temperature-time path post eruption, therefore are can be subdivided into flight-quenched and deposit-quenched pyroclasts. There is however, an overlap between these, as some small achneliths have not fully quenched in flight, forming sub-spherical obsidian drops that deformed slightly on the scoria.

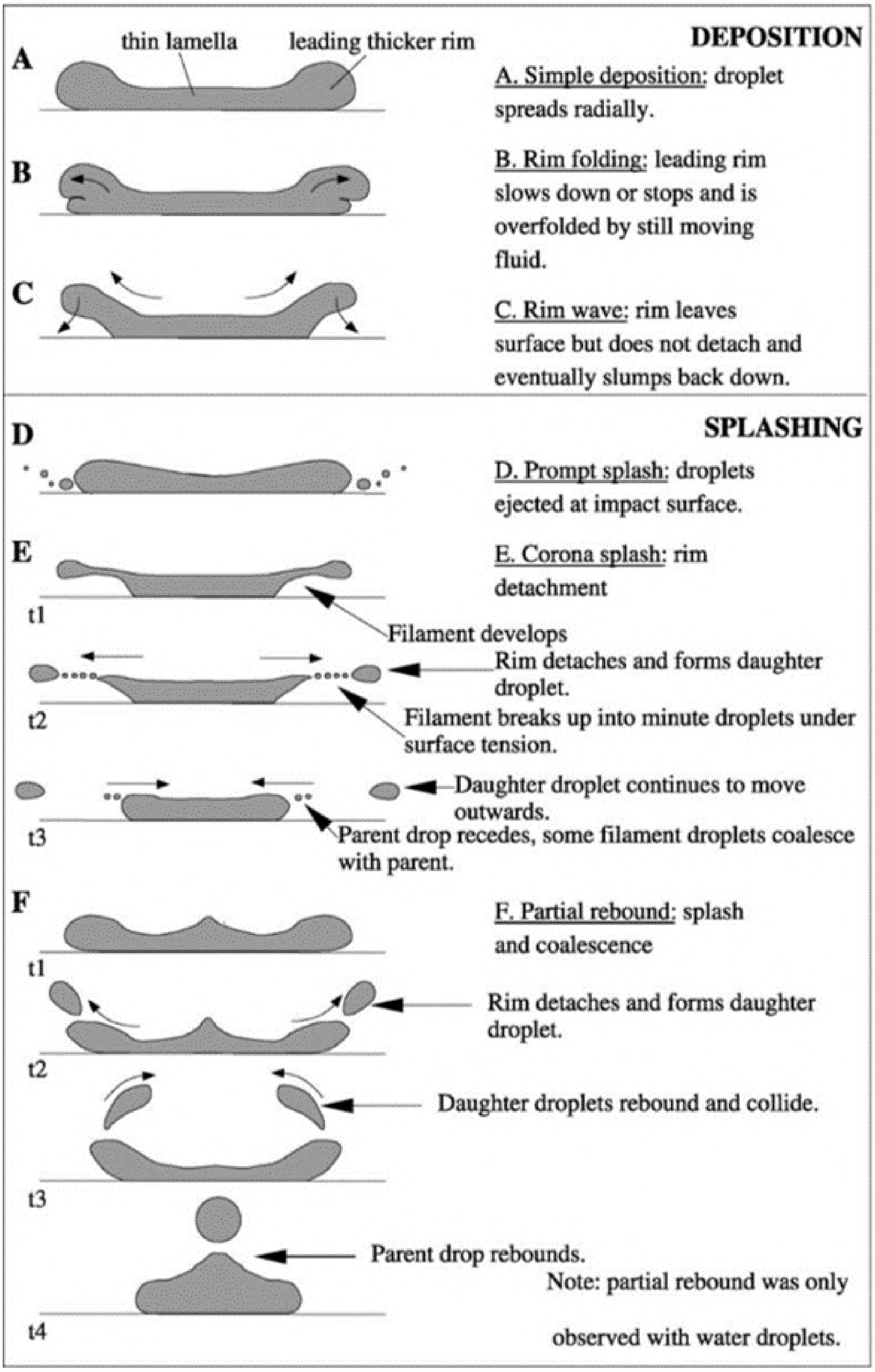

Figure 51: Taken from Sumner et al., (2015). Summary of observed rim perturbations of low viscosity magma seen during laboratory and computational modelling. Simple deposition leads to no secondary fragmentation of the magma (a-c). During splashing, small droplets are detached from the rims of low viscosity magmas (d-f).

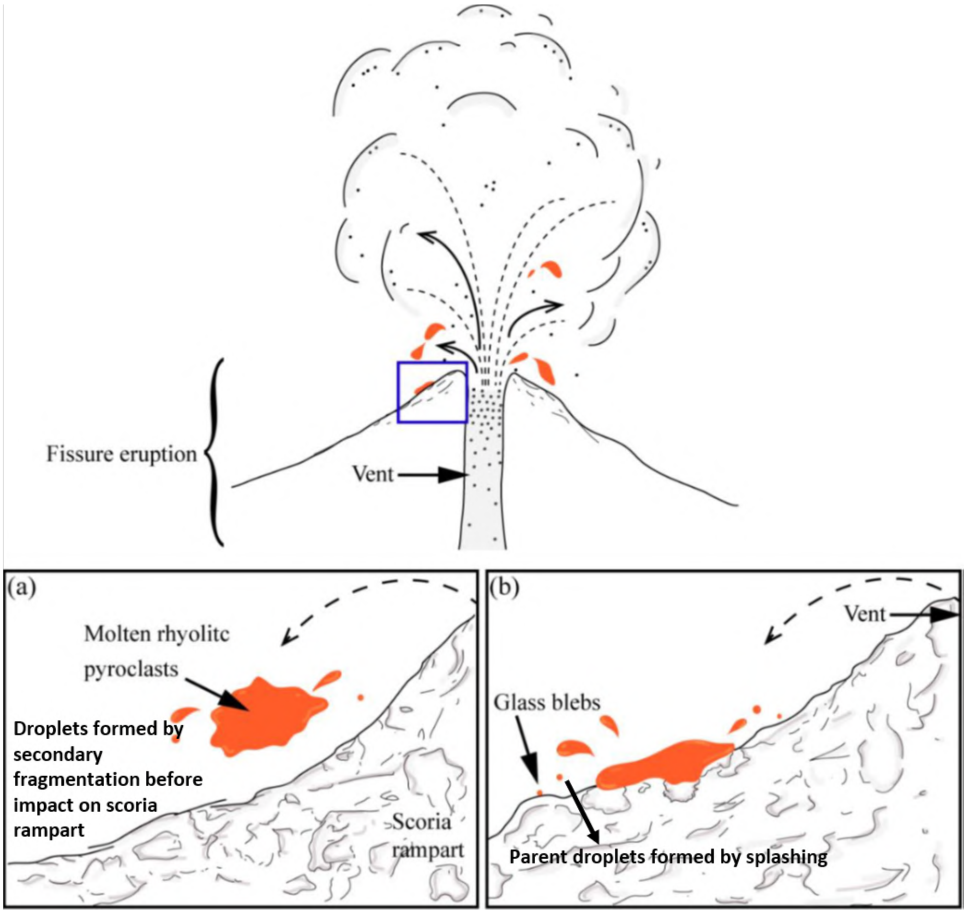

Figure 52: Schematic diagram showing (A) achneliths forming through secondary fragmentation of larger volume AOPs and (B) achneliths forming by splashing of low viscosity pyroclasts on impact. A is the preferred hypothesis of formation as larger AOPs reflect folded rims which are seen when low viscosity magmas undergo simple deposition (see figure 51)

4.4 Contact relations

The contact between the scoria and obsidian pyroclasts are macroscopically consistent across all 41 samples. There is a general lack of evidence for magma mixing on Ascension Island indicating that magmas typically do not encounter other melts during ascent through the crust (Chamberlain et al., 2019). Pore spaces at the contact between the scoria and obsidian are mostly infilled, implying the viscosity of the obsidian was low enough to seep into the small (<1 mm) spaces. Additionally, it confirms that the scoria clasts were quenched before coming into contact with the hot obsidian. Most contacts are sharp and lined by microlites of oxides, which may represent a sintered interface (Owen et al., 2018). The radial growths from the scoria are on micron-scale and may be the only thermal response from the interaction of the chilled scoria and hot obsidian. There are a few phenocrysts in the obsidian where the rims have a nucleated overgrowth feature and appear to not be stable within the glass. Textures on crystal rims of anorthoclase, visible in figure 45, may indicate rapid cooling/quenching (bright patches of scattered Fe-Ti oxide microlites and black flower-like rims around the overgrowth).

4.5 In-situ glass geochemistry

In-situ geochemical analyses on obsidian and scoria glass reveals two distinct magma types. Obsidian compositions range from trachy-andesite to rhyolitic. However, most data points plot within the rhyolitic field on figure 37, clustering between 71.0-74.0 wt.% SiO_2. Other felsic lavas with a glassy matrix in the vicinity of Letterbox contain SiO_2 concentrations between 71.2-74.0 wt.% (Chamberlain et al., 2019), which conforms with the range seen within these more unusual pyroclasts. Typical Ascension felsic products are depleted in Ti, Sr, Ba, whilst mafic products are depleted in MgO, Na_2O, and K_2O. Mafic products are typically more enriched in MgO, CaO, and TiO_2 (Chamberlain et al., 2019). Major and minor element traverses (from EMPA data) supports that the obsidian is homogeneous in composition. No intermediate compositions are found between the two distinct magmas (figure 37) therefore despite erupting coevally, they are not co-magmatic in origin.

5 Discussion

This study has revealed that a monogenetic, basaltic fissure eruption co-erupted dominantly trachy-andesite scoria along with small volumes of rhyolite obsidian pyroclasts and lithic clasts. The eruption is unusual as the fluidal obsidian clasts, which mechanically adhered to scoria post-deposition, do not exhibit textures that would indicate mingling with the trachy-andesite magma prior to the eruption. AOPs are also unique as they represent ductile, visco-elastic clasts found in a deposit of dominantly brittley fragmented pyroclasts.

5.1 Viscosity

The highly fluidal textures of AOPs remain ambiguous. For a magma to form fluidal textures on deposition, it has to have low viscosities. Phenomenological evidence for this is that most fluidal clasts are observed in basaltic eruptive products and rarely in silicic magmas as they are erupted at much higher viscosities (Lesher and Spera, 2015). For comparison, while the viscosity estimate for rhyolites at storage conditions in the Earths crust might be similar at $\sim 10^4$ Pa.s to basaltic eruptive viscosities (calculated using the viscosity model from Hess and Dingwell, 1996, input water concentrations from 120 MPa storage pressure (Castro and Dingwell, 2009) and the solubility of water taken from Liu et al. 2005), during ascent and degassing, all rhyolites on Earth are expected to lose water. Degassing of pre-eruptive water drives the viscosity up significantly, resulting in a degassed viscosity range around 10^9-10^{12} Pa.s (Wadsworth et al. 2018), far from the window required for fluidal clasts (see figure 53, arrow 1, which starts at storage conditions of $\sim 10^5$ Pa.s).

Further, peralkaline (molar $Na_2O + K_2O/Al_2O_3 > 1$) fluidal clasts described by Clarke et al., (2019) (see figure 48) containing 2.5-5 wt.% H_2O prior to eruption have calculated pre-eruptive viscosities in the range of 10^2-10^4 Pa s. Eruptive degassing leads to erupted viscosities of 10^6-10^8 Pa.s. These viscosities produced pumiceous fluidal clasts which resemble bread-crust bombs (i.e. brittle surface cracks and in-situ inflation on deposition) and cowpat bombs. The viscosities calculated here are much lower than typical erupted (non-peralkaline rhyolites) which are in the range of $\sim 10^9$-10^{12} Pa.s at low water contents (figure 53). Comparing the viscosities of hydrous peralkaline obsidian (which are typically much lower than rhyolitic obsidian observed in this study) shows the likely extremity and unusual nature of the fluidal textures of the AOPs. It can be inferred that AOPs eruptive viscosities are much lower than those which produced the peralkaline pyroclasts ($<10^6$ Pa.s). Typical erupted viscosities of rhyolite are at magnitudes in the range of pitch and higher (figure 53). Pitch is highly viscous and would not produce fluidal textures seen in AOPs.

The rhyolite studied here is co-erupted with basalt during a dominantly basaltic eruption of Hawaiian style. This generally implies a high eruption temperature compared to eruptions temperatures for rhyolites (e.g. 1100-1200°C; Taddeucci et al., 2015). Therefore, it is likely that the rhyolite was heated to temperatures approaching this range, representing superheating compared with typical rhyolite conditions (see figure 53). In figure 53, viscosity as a function of temperature is shown for a range of water concentrations dissolved in a rhyolitic melt (calculated after Hess & Dingwell, 1996, using model 4 from the paper). It is clear that while degassing will result in a viscosity increase of many orders of magnitude, the effect of superheating (likely to have occurred in the case studies here) is approximately sufficient to reduce the viscosity during degassing back to the range that would have been typical of un-degassed pre-eruptive rhyolite (see figure 53, arrow 2). This offers a simple explanation for why degassed rhyolite can form textures typical of low-viscosity basaltic clasts, and provides constraints on the degree of heating that occurred during eruption.

5.2 Generation of two magmas

The geochemical glass compositions of the two magmas are distinct and there is no linear trend between the in major and minor trace elements (figure 41) and feldspar phenocrysts (figure 39). This suggests that the melts are distinct of each other. Groundmass glass composition of the scoria samples is trachy-andesite (55.5-58.8 wt. % SiO_2), whilst the composition of the obsidian is rhyolitic. The two magmas lack mingling textures, evidenced by sharp contacts. The generation and storage conditions of coeval, bimodal magmas that erupted from the vent is enigmatic.

Ascension Island exhibits a wide range of magma compositions; olivine basalt - hawaiite - mugearite

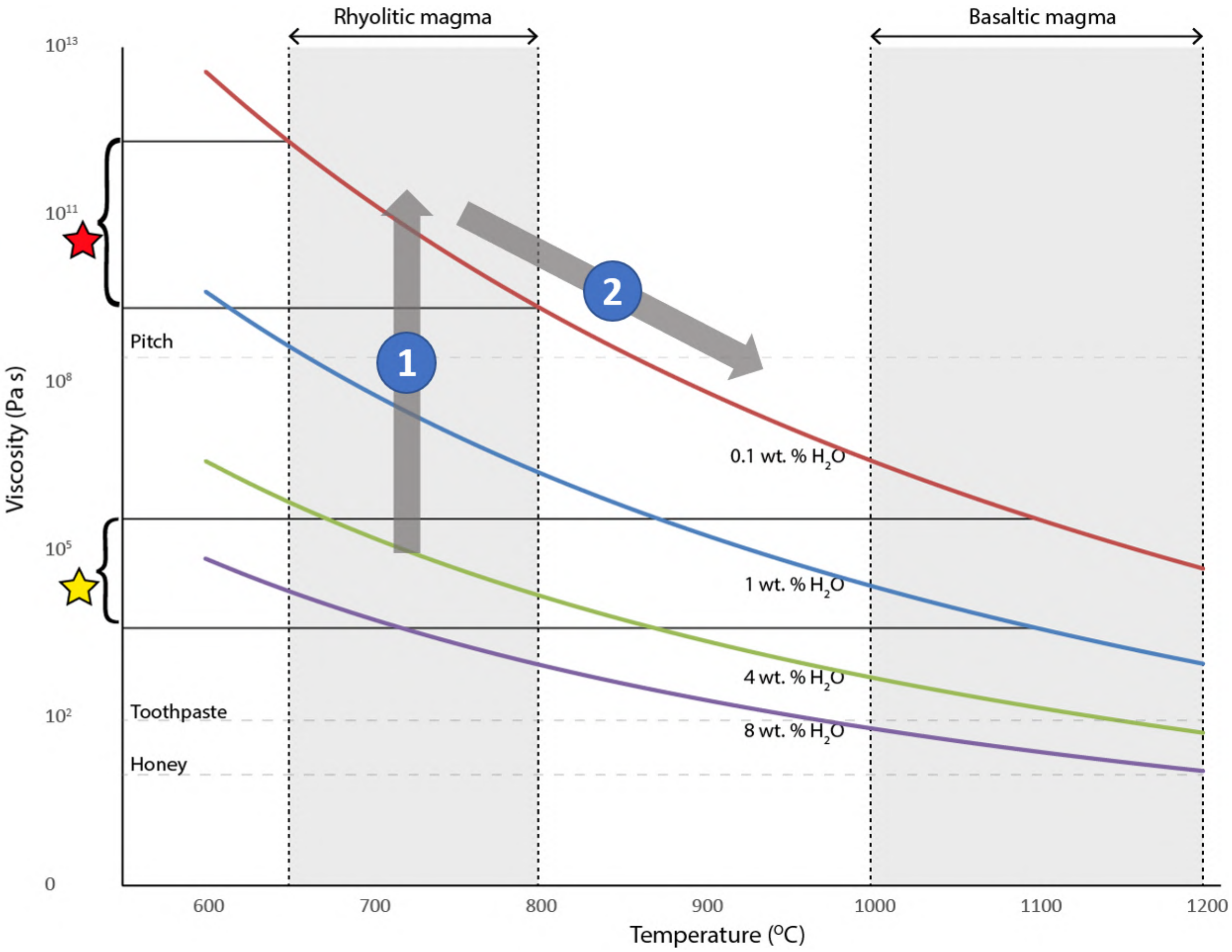

Figure 53: Viscosity as a function of temperature for only rhyolitic magma calculated using Hess and Dingwell (1996) VFT equation. The equation used for the construction of this graph can be found in Hess and Dingwell (1996), where the parameters were taken from table 1, model 4, which are true for all hydrous rhyolitic melts. Light grey, dashed-line boxes highlight the typical range for temperatures for basaltic and rhyolitic magma. Yellow and red star represents the typical window of viscosity for basaltic and rhyolitic magma respectively. As a batch of rhyolitic magma rises within the conduit, it degasses and loses water, increasing its viscosity (arrow 1). Re-heating of the magma to basaltic temperature would decrease the viscosity of the rhyolitic melt providing it lost exsolved volatiles by outgassing (otherwise, it would likely follow a trend similar to arrow 1 again). Therefore volatile-poor obsidian would have re-heating path similar to arrow 2. This also accounts for the low vesicularity seen within AOPs.

- benmoreite - trachyte - rhyolite (Daly, 1925; Weaver et al., 1996; Jicha et al., 2013; Preece et al., 2018). Fractional crystallisation is the proposed dominant mechanism for producing evolved melts on Ascension Island, as evidenced by the continuous trend in major and minor trace elements (Harris, 1983; Kar et al., 1998; Jicha et al., 2013; Chamberlain et al., 2016: 2019). Minor amounts of assimilation and contamination are thought to be partially responsible for the radiogenic Sr isotope composition of more felsic melts (Kar et al., 1998). Mafic magma on Ascension Island has been attributed to partial melting of a consistent source, or different mantle regions (Chamberlain et al., 2019). Partial melting of mafic material at other hotspot volcanic islands has been shown to be a significant driver for the production of evolved magmas, often resulting in bimodal compositions and few erupted magmas of intermediate compositions (e.g. Charlier et al., 2013; Meade et al., 2014 [Chamberlain et al., 2019]). However, partial melting of a constant source is not considered as a mechanism for felsic melt generation on Ascension Island as there is no evidence in isotopic ratios between the mafic and felsic melts (Kar et al., 1998) and major and trace elements vary co-linearly (Kar et al., 1998; Jicha et al., 2013).

Magma mixing between felsic and mafic magmas to produce intermediate magmas could be responsible for the continuum in whole rock composition, yet non-linear variations in major and trace elements in both whole rocks and crystal phases suggest that this is unlikely (Chamberlain et al., 2019). Petrographic data shows no evidence for magma mixing, indicating that while a wide range of magma compositions are erupted across a ~12 km diameter island, they do not encounter other melts during their transport through the crust (figure 3).

Rhyolitic magmas on Ascension Island are mostly generated through closed system fractional crystallisation. AOPs and the scoria show no evidence for chemical equilibrium and plot separately on bivariate plots (figures 37; 39; 40; 41). Morphology of feldspar is controlled by changes in temperature, pressure, melt composition (including water) and growth, dissolution and nucleation kinetics (Bennett et al., 2019). Pre-existing crystals can resorb due to superheating which can be caused by magma mixing (Bennet et al., 2019). Magma mixing causes periods of disequilibrium, however there is little to no chemical variance seen within macrocrysts suggesting this phenomena, unlike zoned crystals which record geochemical variances in an evolving magma. Some phenocrysts show evidence of breakdown and are highly fractured (figure 47). The physical breakdown of the anorthoclase crystals is likely due to a change in temperature or pressure. Some crystal relics of anorthoclase are highly broken down into Fe-Ti microlites and feldspar. However, the obsidian phenocrysts show no systematic differences in the core and rim, chemical zonation or overgrowth textures, suggesting the phenocrysts were in equilibrium within the rhyolitic melt, and physical breakdown of anorthoclase macrocrysts was likely a result of re-heating during the eruption. This further exemplifies the lack of mixing.

Field relationships indicate that the two magmas in this study could not have been co-erupted from a density stratified chamber as the rhyolite is scattered throughout the scoria ramparts, rather than appearing gradually within the outcrop (as seen in the zoned deposit [Sparks et al., 1984; Blake and Ivey, 1986; Blake and Campbell., 1986; Chamberlain et al., 2016]). Additionally, the erupted volume of the rhyolitic magma is small therefore the two magmas are unlikely to be derived from a zoned magma chamber. However, this assumes that an erupted density stratified magma chamber will erupt similar quantities of bimodal compositions and there was potential for the magma to be completely drawn out of the magma chamber. But the lack of magma mixing corresponds to the wider Ascension picture which also sees a lack of magma mixing.

Similar-looking obsidian pyroclasts occur within the Dòmadalshraun lava flow, Iceland (McGarvie, 1985) as they show co-erupted scoria with entrained, fluidal obsidian. Textural differences observed show that the Iceland obsidian has a noticeably greater vesicularity (seen by larger vesicles, and a higher population of vesicles), due to foaming during heating. Additionally, the basalt and rhyolite clasts in Iceland have mingled, shown by sheared threads of completely re-melted rhyolite found as thin (approximately <2 mm) laminated layers surrounding a larger (∼9 cm) clast of obsidian, which is enclosed within basalt (figure 54). This has resulted in a less sharply defined contact compared to those of the AOPs, and indicates syn-eruptive mingling. Perhaps, given additional time within the conduit, AOPs and the co-erupted scoria could have mingled to the same extent shown by these pyroclasts found on Iceland.

In addition, similar clasts were erupted from Tarawera volcano (see figure 55), New Zealand, 1886

Figure 54: Hand sample of a similar pyroclast found in the Dòmadalshraun lava, Iceland. Vesicular obsidian (centre) is entrained within scoria. This pyroclast is also found at another lava flow, Hàölduhraun, Iceland. Collected by Dave McGarvie.

(Nairn 1979; Simmons et al., 1993; Rosseel et al., 2006; Carey et al., 2007; Schauroth et al., 2016). Rhyolitic clasts were co-erupted with basalt in a basaltic fissure-fed eruption which cut across a pre-existing rhyolite dome complex (Nairn 1979; Simmons et al., 1993; Carey et al., 2007). Tarawera was an explosive, basaltic, Plinian fissure eruption whilst Ascension Island was small-volume Hawaiian fire-fountaining fissure eruption. Tarawera pyroclasts consist of: (1) basaltic cored bombs, with rhyolitic lithic clasts found at the core, (2) cauliflower textured bombs with adhered rhyolitic fragments, and (3) wall-rock fragments of re-melted, vesiculated rhyolite rinds on basaltic clasts. The rhyolite clasts range from ragged to fluidal in morphology (Rosseel et al., 2007; Carey et al., 2007).

Both scoria and obsidian components within the Tarawera pyroclasts and the AOPs lack welding, sintering or mingling textures. Although Tarawera pyroclasts exhibit fluidal textures, many larger rhyolitic inclusions show no evidence of softening or melting (Rosseel et al., 2007). Clasts of this nature helped to hypothesise that the fluidal rhyolitic clasts were re-heated and re-melted pre-erupted felsic country rock as they provide a potential origin. The cored and welded Tarawera basalt and rhyolite bombs were likely generated by the recycling of lithic clasts within the subsurface of the conduit, resulting in the accretion of rhyolitic and basaltic magma (Rosseel et al., (2007). Further, Schauroth et al., (2016) proposed that the rhyolite clasts were reheated by shearing along the conduit margin. The Ascension Island fissure lacks evidence for non-melted clasts, however due to their similarities in textures with Tarawera pyroclasts, AOPs may have a similar origin.

5.2.1 Melting of country rock

An alternative mechanism to generate magma is that of reheating country rock. The proposed origin of the Tarawera pyroclasts is assimilation of underlying country rock at the conduit margins at shallow depths (<10 m) of the fissure. The basaltic magma re-incorporated felsic clasts and reheated them. The fissure eruption on Ascension cut through lavas of the Eastern Felsic Complex. This is similar to the Tarawera, therefore it is feasible that the AOPs were generated by melting of country rocks by the basaltic magma (figure 56).

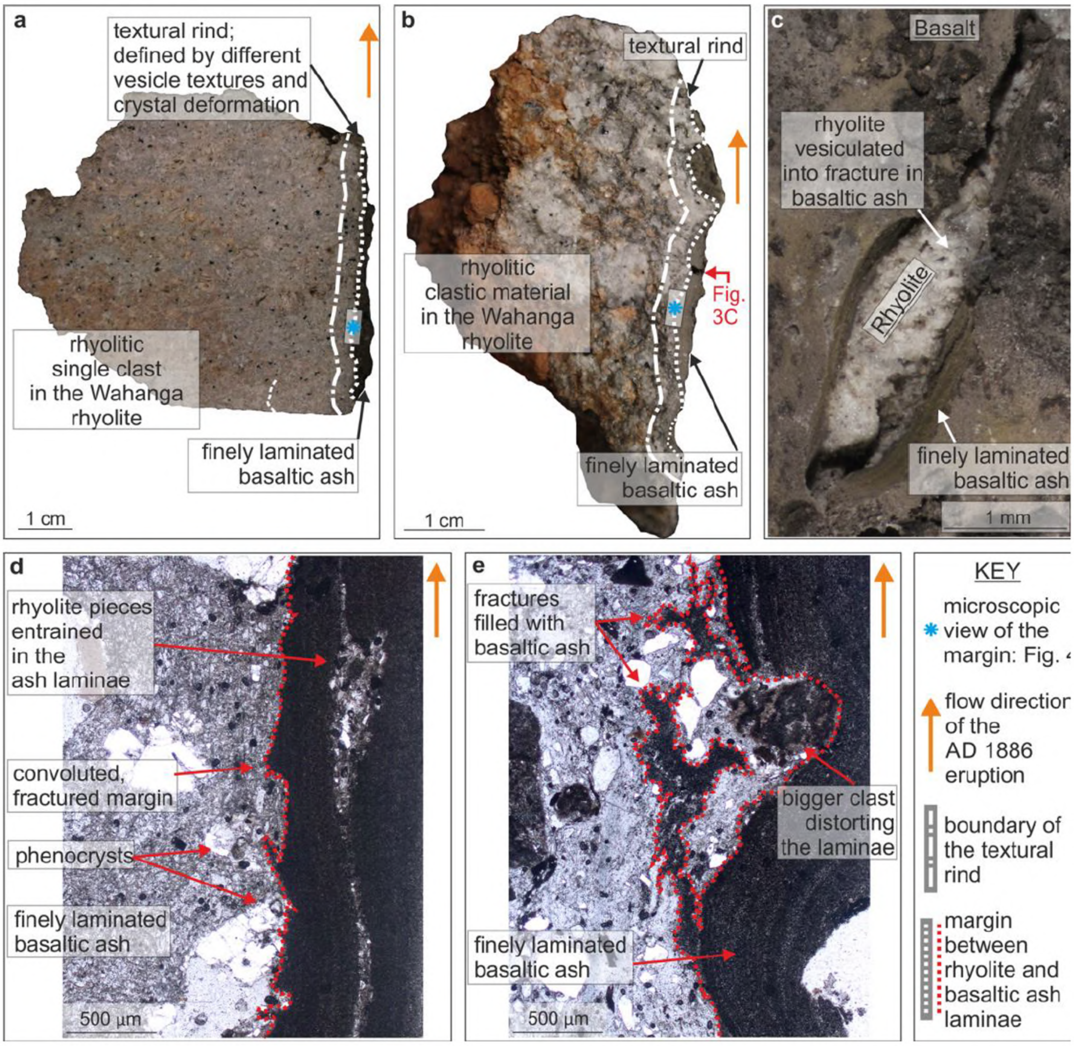

Figure 55: Taken from Schauroth et al., (2016). Photographs of the contacts between basaltic and rhyolitic clasts. (A) Photograph of a single rhyolitic clast in contact with finely laminated ash. (B) Clastic rhyolite in contact with the feeder dyke margin. (C) Close up of (B). (D E) Photomicrograph of rhyolite and basaltic ash.

To remobilise pre-erupted, glassy rhyolitic country rock, temperatures must surpass the glass transition temperature resulting in ductile deformation so there is the 'softening' to provide fluidal textures. Country rock at Tarawera is proposed to have been reheated by the basaltic magma to temperatures between 1000°-1200°C (Taddeucci et al., 2015). Schauroth et al., (2016) calculated that glass transition-temperatures of (Tarawera) rhyolite (at a viscosity of $10^{11.4}$ Pa.s) with 0.01 and 0.1 wt.% dissolved water are 865 and 740°C, respectively (using the Hess and Dingwell [1996] viscosity model). Schauroth et al., (2016) suggested that if the reheated clasts at Tarawera have a high proportion of glassy groundmass, the initial solid phase thermally is susceptible to 'softening' and viscous deformation as the glass transition-temperature is exceeded (Dingwell and Webb, 1990), further facilitating re-mobilisation and heating (see figure 57 for schematic eruption timeline). Evidence within Tarawera pyroclasts for remelting includes brittle and crystal-plastic deformation within biotite crystals. Melting is also evidenced by the glassy margins of rhyolitic clasts (figure 55).

Macrocrysts in the AOPs show physical breakdown (figure 47) indicating a degree of disequilibrium, but not as extensively as those found at Tarawera. The feldspar phenocrysts in the AOPs do not show significant amounts of chemical alteration (zoning), indicating that the timescale of the eruption was not long enough to invoke significant chemical alterations. In contrast to Tarawera pyroclasts, the AOPs show more fluidal textures, which implies they were heated for either a longer duration or to higher temperatures, or that the AOPs had lower water concentrations. A key difference is that the AOPs do not show the cored textures of the Tarawera clasts or evidence for partial melting from mafic magma.

The way this was written previously made it sound like a crystalline rhyolite was being wholesale melted, rather than what is actually my interpretation, which is that a glassy rhyolite was being softened. With this clarification, there need by no significant alteration of the pre-existing phenocrysts/microlites in the rhyolite and in fact the temperature in the rhyolite may never have reached the solidus for any individual phase at all. The constraint is simply that the temperature did exceed the glass transition temperature of the rhyolite. Therefore I propose that the rhyolite crystal population is not as diagnostic of the heating or subsequent cooling as suggested here.

Other obsidian clasts on Ascension Island has been previously attributed to the eruption of water-poor felsic magma residing in the crust, which evolved through fractional crystallisation of less-evolved mafic magma (Sheppard and Harris, 1985). AOPs formation is inconsistent with erupting from a residing magma within the crust, as it does not offer an explanation for the bimodal glass compositions in the obsidian and scoria, lack of chemical zoning in individual macrocrysts in the obsidian, mingled textures, viscosity contrasts and low volume of obsidian. However, as the basaltic fissure overlies a felsic lava, re-melting of previously erupted, glassy rhyolite clasts to basaltic temperatures provides a feasible explanation for the low eruption volume of the obsidian and fluidal textures. This explains the lack of significant alteration of the pre-existing phenocrysts/microlites in the rhyolite (as evidenced by lack of zoning), and suggests that the temperatures in the rhyolite may never have reached the solidus for any individual phase change. Re-heating pre-erupted, glassy clasts also accounts for the general low vesicularity of AOPs as they would have mostly degassed during the previous felsic eruption. Further, it provides reasoning for the two magmas viscosity differences and lack of intermediate magma composition as there was no time for homogenisation, therefore it is currently the preferred hypothesis. However, AOPs are different from Tarawera pyroclasts as AOPs are not as extensively mingled and lack any examples of partially melted rhyolite country rock. Further work is needed to understand their genesis.

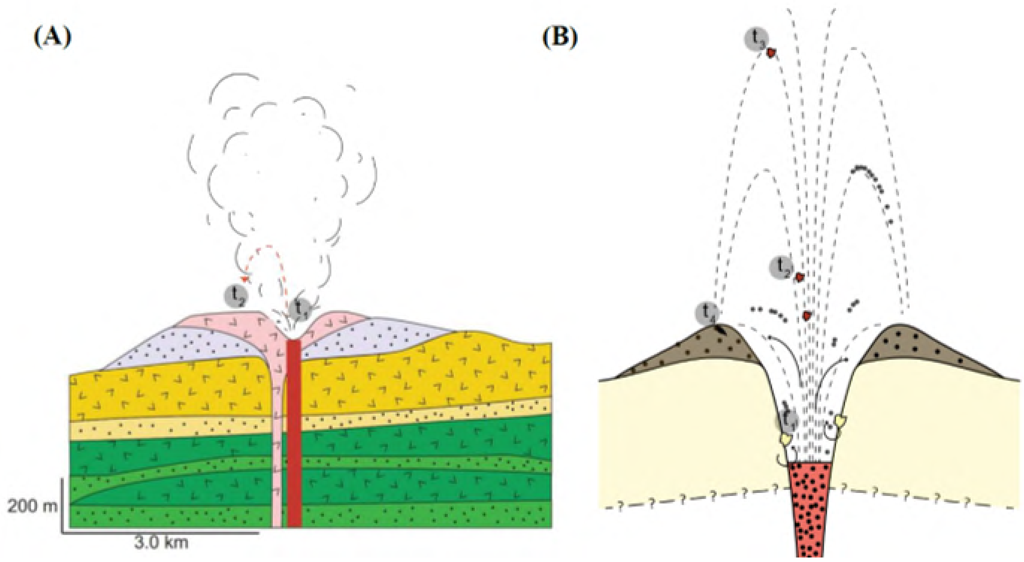

Figure 56: (A) Tarawera figure modified from Carey et al., (2007). The fissure (red) cuts through a series of dome complexes. The mingled basalt and rhyolite pyroclasts are hypothesised to be a result of re-heating of rhyolitic clasts on the conduit walls. (B) Schematic diagram of fissure through felsic lavas (yellow) on Ascension Island. The rhyolite pyroclast from Tarawera do not exhibit fluidal textures as extensive as AOPs and have a higher relative porosity. T1, T2, T3 T4 are represented on figure 57, highlighting the stages of temperature, porosity and water content differences between AOPs and Tarawera pyroclasts.

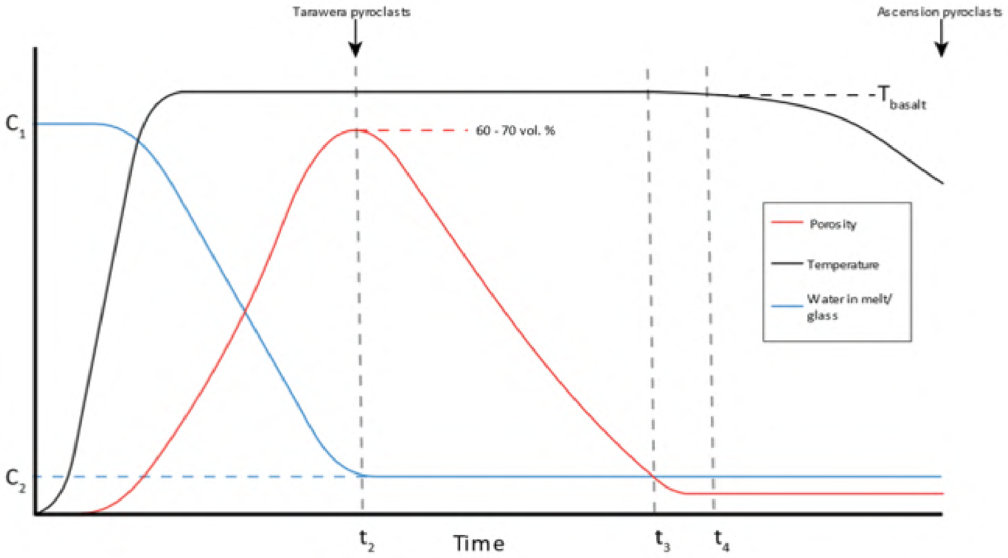

Figure 57: Schematic graph showing the variations in porosity, temperature and water in melt/glass through the timescale of the eruption. C_1 Initial water content in melt (wt. %). C_2 final water content in glass (wt. %). Tarawera pyroclasts exhibit porosities of around 60-70 vol.% (Carey et al., 2007), whereas AOPs have very low porosities. To preserve fluidal textures seen in AOPs, it is likely that AOPs were heated more extensively than Tarawera pyroclasts. T_2 recorded porosity, water content and erupted temperatures of Tarawera bombs. T_3 Outgassed magma. T_4 temperature, and inferred water content/porosity of the magma upon deposition, where the pyroclasts underwent ductile deformation, before finally relaxing as they surpassed the glass transition temperature.

6 Conclusions

1. A small-volume (<0.001 km3) monogenetic fissure co-erupted fluidal obsidian pyroclasts in a dominantly basaltic Hawaiian fountaining episode on the east side of Ascension Island. The basaltic scoria and spatter formed largely non-welded ramparts which also consist of spatter lapilli and bombs and scattered obsidian clasts. The ramparts overlie porous, brecciated rhyolite lava which has a thin, orange-weathered surface, inferring a hiatus between felsic and mafic volcanism.
2. Obsidian pyroclasts range from coarse ash to spatter bombs. They landed hot and ductile, deforming over scoria clasts and through pore spaces resulting in complex, polygonal morphologies, such as suspended drops, large outflows, flat tops and irregular tongue-like shapes. The fluidal morphologies infer low melt viscosities on eruption.
3. The contact between the obsidian, scoria and lithics is ubiquitously sharp, indicating the clasts mechanically adhered post-eruption without mingling. Feathery, spherulite-like, overgrowths on the scoria are seen in BSE images indicating a thermal diffusion profile (hot obsidian landed on chilled scoria).
4. The obsidian pyroclasts account for 0.0007 km^3 (0.005%) of the total erupted volume, implying the obsidian clasts are either derived from a source of limited volume or are not efficiently incorporated into the eruption column.
5. In-situ geochemical analyses on glass (obsidian and scoria groundmass glass) confirms two distinct magmas. Obsidian is rhyolitic (~73.0 wt.% SiO2) and the scoria is trachy-andesite (55.5-58.8 wt.% SiO_2). Macrocrysts in the scoria and obsidian are different feldspar species. Obsidian contains anorthoclase ($Ab_{64\text{-}85}$, $Or_{13\text{-}35}$, $An_{<1\text{-}2}$), whereas scoria contains a continuum between labradorite to andesine ($An_{36\text{-}53}$, $Ab_{45\text{-}57}$, $Or_{1.5\text{-}5}$).
6. Anorthoclase macrocrysts in the obsidian clasts are commonly externally resorbed and show evidence for physical breakdown (highly fractured), but lack any evidence for chemical disequilibrium. Phenocrysts in the scoria also lack chemical disequilibrium but show no signs of physical

breakdown/resorption. The absence of a clear geochemical relationship across both the scoria and obsidian implies the two magmas are not related or co-magmatic.

7. The lack of compositional zoning in phenocrysts, mingling textures, mixing and intermediate magma compositions strongly suggests that the magmas did not reside together within the crust (i.e. we can discount a compositionally stratified magma chamber).
8. Similar pyroclasts observed at Tarawera, New Zealand, are interpreted to be re-melted wall-rock fragments from the conduit margins during a basaltic Plinian eruption. The felsic rock were re-mobilised as temperatures exceeded the glass transition temperature. Re-heating, re-melting and reaming out of ductile country rock proximal to the conduit walls is an alternative mechanism of generating magma, therefore Ascension obsidian pyroclasts may be a result of re-heated rhyolitic clasts on the fissure margins. This provides a feasible explanation for the low erupted volume of the obsidian clasts, and heating clasts to basaltic temperatures would lead to fluidal textures. However, Ascension lacks any examples of a partially melted clasts, unlike Tarawera which provided conclusive field evidence that the conduit margins were re-heated.
9. The unusual nature of these pyroclasts show evidence for non-uniform, complex conduit dynamics. But both fractional crystallisation and re-melting of country rock are unsatisfactory mechanisms for producing the obsidian clasts, therefore further work is needed to understand their genesis.

7 Further Work

The research presented in this thesis has provided insight into the obsidian pyroclasts, with the preferred hypothesis concluded as the fluidal obsidian clasts are re-melted and re-heated felsic country rock which has been reamed out of the fissure margins. The remaining questions which regard the unusual nature of AOPs include: (1) why do AOPs have low vesicularities? and (2) did AOPs extensively degas? Further questions, which encompass the wider picture include: (3) what temperatures and storage pressures did the scoria and obsidian form? and (4) what are the eruptive temperatures of the obsidian and scoria?

Further work for (1) and (2):

Fourier-transform infrared spectroscopy (FTIR) is an in-situ analytical technique used to qualitatively and quantitatively measure elements (Wysoczanski and Tani, 2006). This technique obtains an average water species content (OH^- and H_2O) for the area analysed. Analysis of water content in volcanic rocks provides insights into magmatic processes (melting, crystallisation and assimilation). If the AOPs have lower initial water concentrations than the typical concentrations of stored rhyolitic magma (4-6 wt.%), perhaps these concentrations could explain low vesicularities seen within the clast. However, this data has not been presented in this thesis as it belongs to someone within the collaborative Ascension group.

The Vogel-Fulcher-Tammann (VFT) equation (Hess and Dingwell, 1996) relies on the composition (EMPA data) and water concentrations (FTIR data) in order to calculate the eruptive viscosity of the rhyolitic magma. This technique can utilise data previously collected and provide quantitative data on the viscosity, potentially leading to conclusive viscosities responsible for AOPs highly fluidal textures.

Further work for (3) and (4):

There are a wide range of geothermometry and geobarometry methods available to deduced pressure/temperature conditions of magmas. For example, Waters and Lange (2015) deduced a plagioclase-liquid hygrometer and thermometer for plagioclase crystals in a rhyolitic melt which is based on the exchange reaction of anorthite between plagioclase and liquid. Through obtained EMPA data, pre-erupted temperatures can be calculated for the scoria and obsidian. However, this is dependent on the crystals present within the magmas. Therefore the most reliable method, which is applicable for any composition, is to form a suite of petrology experiments. Castro and Dingwell, (2009) assessed storage conditions of magmas by taking juvenile clasts and subjecting them to range of P_{H_2O}-T. Samples of known whole rock composition and mineral chemistry were placed within water-pressurized Waspaloy cold-seal vessels with nickel filler rods to return them to high temperatures and pressures. Following this, samples where decompressed at 5 MPa intervals with a hand-operated pressure intensifier. The samples were then analysed using SEM and EMPA to see which retained the correct mineral assemblage and composition of the minerals themselves. This provided a window of pressure and temperature conditions that these minerals could be collectively stable at. Further, the pressures can be corresponded to depths within the crust. When applying this to AOPs, replicating the physical breakdown of anorthoclase macrocrysts and re-producing the general lack of crystals within the obsidian would likely give a range of pressure/temperature conditions for the obsidian. This would also provide further insight into the storage pressure and depth of the trachy-andesite magma which resulted in the fissure eruption, allowing a more general association with the wider Ascension plumbing system.

7.1 Note Added After Submission

A field excursion to Ascension Island in January 2020 uncovered a clast which showed a gradational contact between flow banded country rock and fluidal obsidian (figure 58). This provides conclusive evidence for the re-melted country rock hypothesis; therefore we can discount the two magma hypothesis. Country rock has been collected for future laboratory experiments which will involve re-heating the country rock to basaltic temperatures. This would enable viscosity to be directly measured and provide a record of vesiculation and whether the clasts densify.

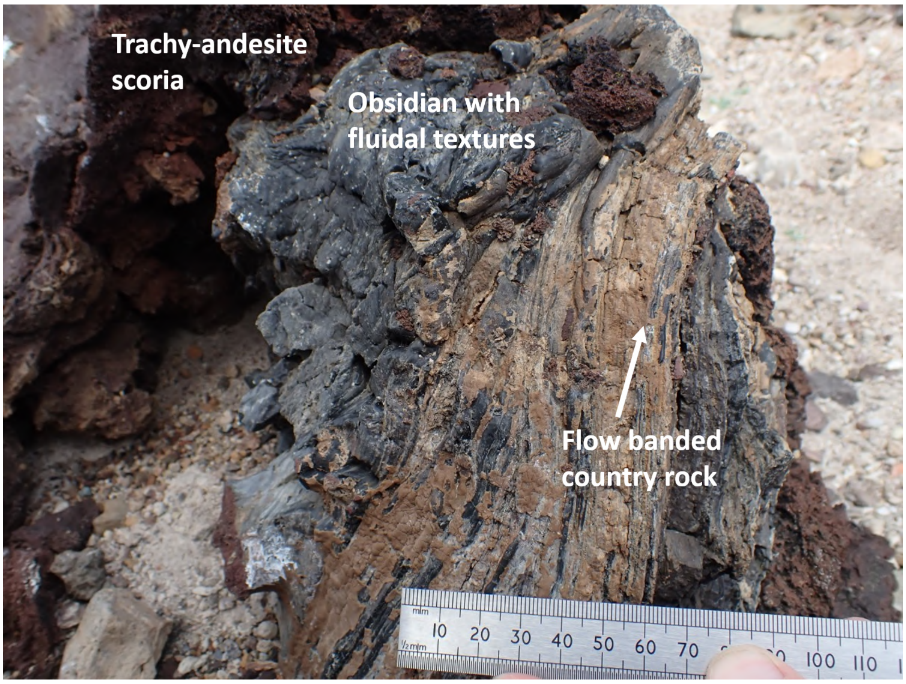

Figure 58: Partially molten clast found a field excursion to Ascension Island, 2020. The clasts has a gradational contact between flow-banded country rock, to fluidal obsidian textures.

References

Atkins, F. B., Baker, P., Bell, J. D., and Smith, G. (1964). Oxford expedition to ascension. *Nature*, 204(4960):722–724.

Bennett, E. Lissenberg, C. and Cashman, K. (2019). The significance of plagioclase textures in mid-ocean ridge basalt (gakkel ridge, arctic ocean). *Contributions to Mineralogy and Petrology*, 174(6).

Best, M. (2013). Igneous and metamorphic petrology. *Malden, MA: Blackwell Publishers.*

Blake, S. and Campbell, I. (1986). The dynamics of magma-mixing during flow in volcanic conduits. *Contributions to Mineralogy and Petrology*, 91(1):72–81.

Blake, S. and Fink, J. H. (1987). The dynamics of magma withdrawal from a density stratified dyke. *Earth and Planetary Science Letters*, 85(4):516–524.

Blower, J. D., Keating, J. P., Mader, H. M., and Philipps, J. C. (2002). The evolution of bubble size distributions in volcanic eruptions. *Journal of volcanology and Geothermal Research*, 120:1–23.

Browne, B. and Szramek, L. (2015). *Rates of Magma Ascent and Storage.* Elsevier Inc., second edition.

Burgisser, A. and Degruyter, W. (2015). Magma Ascent and Degassing at Shallow Levels. *The Encyclopedia of Volcanoes*, pages 225–236.

Campbell, I. H. and Turner, J. S. (1985). Turbulent mixing between fluids with different viscosities. *Nature*, 313(5997):39–42.

Cannata, C. B., De Rosa, R., Donato, P., Donato, S., Lanzafame, G., Mancini, L., and Houghton, B. F. (2019). First 3D imaging characterization of Pele's hair from Kilauea volcano (Hawaii). *Scientific Reports*, 9(1):1–13.

Carey, R. Houghton, B., Sable, J., and Wilson, C. (2007). Contrasting grain size and componentry in complex proximal deposits of the 1886 tarawera basaltic plinian eruption. *Nature*, 69(8):903–926.

Carracedo-Sánchez, M., Sarrionandia, F., Arostegui, J., Errandonea-Martin, J., and Gil-Ibarguchi, J. I. (2016). Petrography and geochemistry of achnelithic tephra from Las Herrerías Volcano (Calatrava volcanic field, Spain): Formation of nephelinitic achneliths and post-depositional glass alteration. *Journal of Volcanology and Geothermal Research*, 327:484–502.

Cashman, K. V. (2004). Volatile controls on magma ascent and eruption. *Geophysical Monograph Series*, 150:109–124.

Cashman, K. V. and Scheu, B. (2015). *Magmatic Fragmentation*. Elsevier Inc., second edition edition.

Cashman, K. V., Stephen, R., and Sparks, J. (2013). How volcanoes work: A 25 year perspective. *Bulletin of the Geological Society of America*, 125(5-6):664–690.

Cassidy, M., Castro, J. M., Helo, C., Troll, V. R., Deegan, F. M., Muir, D., Neave, D. A., and Mueller, S. P. (2016). Volatile dilution during magma injections and implications for volcano explosivity. *Geology*, 44(12):1027–1030.

Cassidy, M., Manga, M., Cashman, K., and Bachmann, O. (2018). Controls on explosive-effusive volcanic eruption styles. *Nature Communications*, 9(1).

Castro, J. M. and Dingwell, D. B. (2009). Rapid ascent of rhyolitic magma at Chaitén volcano, Chile. *Nature*, 461(7265):780–783.

Chamberlain, K. J., Barclay, J., Preece, K., Brown, R. J., and Davidson, J. P. (2016). Origin and evolution of silicic magmas at ocean islands: Perspectives from a zoned fall deposit on Ascension Island, South Atlantic. *Journal of Volcanology and Geothermal Research*, 327:349–360.

Chamberlain, K. J., Barclay, J., Preece, K. J., Brown, R. J., and Davidson, J. P. (2019). Lower Crustal Heterogeneity and Fractional Crystallization Control Evolution of Small-volume Magma Batches at Ocean Island Volcanoes (Ascension Island, South Atlantic). *Journal of Petrology*, 60(8):1489–1522.

Charlier, B., Namur, O., and Grove, T. L. (2013). Compositional and kinetic controls on liquid immiscibility in ferrobasalt-rhyolite volcanic and plutonic series. *Geochimica et Cosmochimica Acta*, 113:79–93.

Clarke, B., Calder, E. S., Dessalegn, F., Fontijn, K., Cortés, J. A., Naylor, M., Butler, I., Hutchison, W., and Yirgu, G. (2019). Fluidal pyroclasts reveal the intensity of peralkaline rhyolite pumice cone eruptions. *Nature Communications*, 10(1):1–10.

Coltelli, M., Del Carlo, P., and Vezzoli, L. (1998). Discovery of a Plinian basaltic eruption of Roman age at Etna volcano, Italy. *Geology*, 26(12):1095–1098.

Daly, R. (1925). The Geology of Ascension Island. *Proceedings of the American Academy of Arts and Sciences*, 60(1):3–80.

Davì, M., De Rosa, R., Donato, P., and Sulpizio, R. (2011). The Lami pyroclastic succession (Lipari, Aeolian Islands): A clue for unravelling the eruptive dynamics of the Monte Pilato rhyolitic pumice cone. *Journal of Volcanology and Geothermal Research*, 201(1-4):285–300.

Dingwell, D. B. (1996). Volcanic dilemma–flow or blow? *Science*, 273(5278):1054–1055.

Dingwell, D. B. (1998). The glass transition in hydrous granitic melts. *Physics of the Earth and Planetary Interiors*, 107(1-3):1–8.

Dingwell, D. B. and Wedbb, S. L. (1989). Relaxation in silicate melts. *European Journal of Mineralogy*, 42(3):427–449.

Duncan, A. and Guest, J. (1982). Mount Etna: Variations in its internal plumbing. *Geophysical Surveys*, 5(3):213–227.

Eaton, J. and Murata, K. (1960). How Volcanoes Grow. *Science*, 132(3432):925–938.

Eichelberger, J., Carrigan, C., and Westrich, H. (1986). Non-explosive silicic volcanism. *Nature*, 2(323):598–602.

Eichelberger, J. C. (1980). Vesiculation of mafic magma during replenishment of silicic magma reservoirs. *Nature*, 288(5790):446–450.

Francis, P. and Oppenheimer, C. (2005). *Volcanoes*. Oxford University Press.

Freundt, A. and Tait, S. R. (1986). The entrainment of high-viscosity magma into low-viscosity magma in eruption conduits. *Bulletin of Volcanology*, 48(6):325–339.

Giordano, D., Russell, J. K., and Dingwell, D. B. (2008). Viscosity of magmatic liquids: A model. *Earth and Planetary Science Letters*, 271(1-4):123–134.

Gottsmann, J. and Dingwell, D. B. (2001). Cooling dynamics of spatter-fed phonolite obsidian flows on Tenerife, Canary Islands. *Journal of Volcanology and Geothermal Research*, 105(4):323–342.

Grove, T. L., Baker, M. B., and Kinzler, R. J. (1984). Coupled CaAl-NaSi diffusion in plagioclase feldspar: Experiments and applications to cooling rate speedometry. *Geochimica et Cosmochimica Acta*, 48(10):2113–2121.

H, S. (2000). Volcanic episodes and rates of volcanism. *Encyclopedia of volcanoes*, Academic Press:271–279.

Harris, C. (1983). Petrology of lavas and associated plutonic inclusions of Ascension Island. *Journal of Petrology*, 24(4):424–470.

Harris, C., Bell, J. D., and Atkins, F. B. (1983). Isotopic composition of lead and strontium in lavas and coarse-grained blocks from Ascension Island, South Atlantican addendum. *Earth and Planetary Science Letters*, 63(1):139–141.

Hay, R. L., Hildreth, W., and Lambe, R. N. (1979). Globule ignimbrite of Mount Suswa, Kenya. *Geological Society of America*, (180):167–176.

Head, J. W. and Wilson, L. (1989). Basaltic pyroclastic eruptions: Influence of gas-release patterns and volume fluxes on fountain structure, and the formation of cinder cones, spatter cones, rootless flows, lava ponds and lava flows. *Journal of Volcanology and Geothermal Research*, 37(3-4):261–271.

Heiken, G. and Wohletz, K. (1985). *Volcanic ash.* Berkeley, Calif.: Univ. of California Pr.

Hess, K. U. and Dingwell, D. B. (1996). Viscosities of hydrous leucogranitic melts: a non-Arrhenian model. *American Mineralogist*, 81(9-10):1297–1300.

Houghton, B. F., Wilson, C. J., Del Carlo, P., Coltelli, M., Sable, J. E., and Carey, R. (2004). The influence of conduit processes on changes in style of basaltic Plinian eruptions: Tarawera 1886 and Etna 122 BC. *Journal of Volcanology and Geothermal Research*, 137(1-3 SPEC. ISS.):1–14.

Huppert, H. E., Sparks, R. S. J., and Turner, J. S. (1982). Effects of volatiles on mixing in calc-alkaline magma systems. *Nature*, 297(5867):554–557.

Huppert, H. E., Sparks, R. S. J., and Turner, J. S. (1984). Some Effects of Viscosity on the Dynamics of Replenished Magma Chambers. *Journal of Geophysical Research*, 89(B8):6857–6877.

Huppert, H. E., Sparks, R. S. J., Whitehead, J. A., and Hallworth, M. A. (1986). Replenishment of magma chambers by light inputs. *Journal of Geophysical Research*, 91(B6):6113.

Ida, Y. and Kumazawa, M. (1986). Ascent of magma in a deformable vent. *Journal of Geophysical Research*, 91(B9):9297.

Jicha, B. R., Singer, B. S., and Valentine, M. J. (2013). 40Ar/39 Ar geochronology of subaerial ascension island and a Re-evaluation of the temporal progression of basaltic to rhyolitic volcanism. *Journal of Petrology*, 54(12):2581–2596.

Jones, T. J., Houghton, B. F., Llewellin, E. W., Parcheta, C. E., and Höltgen, L. (2018). Spatter matters-distinguishing primary (eruptive) and secondary (non-eruptive) spatter deposits. *Scientific Reports*, 8(1):1–12.

Kar, A. (1997). *Unpublished Ph.D. dissertation.*, page 260.

Kar, A., Weaver, B., Davidson, J., and Colucci, M. (1998). Origin of differentiated volcanic and plutonic rocks from Ascension Island, South Atlantic Ocean. *Journal of Petrology*, 39(5):1009–1024.

Klingelhöfer, F., Minshull, T. A., Blackman, D. K., Harben, P., and Childers, V. (2001). Crustal structure of Ascension Island from wide-angle seismic data: Implications for the formation of near-ridge volcanic islands. *Earth and Planetary Science Letters*, 190(1-2):41–56.

Koyaguchi, T. (1985). Letter Section Magma mixing in a conduit. *Journal of Volcanology and Geothermal Research*, 25:365–369.

Koyaguchi, T. and Blake, S. (1989). The dynamics of magma mixing in a rising magma batch. *Bulletin Of Volcanology*, 52(2):127–137.

Lefèvre, R., Gaudichet, A., and Billon-Galland, M. (1986). Silicate microspherules intercepted in the plume of Etna volcano. *Nature*, 322(6082):817–820.

Lesher, C. E. and Spera, F. J. (2015). *Thermodynamic and Transport Properties of Silicate Melts and Magma*. Elsevier Inc., second edition edition.

Liu, Y. and Zhang, Y. (2000). Bubble growth in rhyolitic melt. *Earth and Planetary Science Letters*, 181(1-2):251–264.

Liu, Y., Zhang, Y., and Behrens, H. (2005). Solubility of H_2O in rhyolitic melts at low pressures and a new empirical model for mixed H_2O-CO_2 solubility in rhyolitic melts. *Journal of Volcanology and Geothermal Research*, 143(1-3):219–235.

Mangan, M. T., Cashman, K. V., and Newman, S. (1993). Vesiculation of basaltic magma during eruption. *Geology*, 21(2):157–160.

McGarvie, D. (1985). Unpublished PhD thesis.

Meade, F. C., Troll, V. R., Ellam, R. M., Freda, C., Font, L., Donaldson, C. H., and Klonowska, I. (2014). Bimodal magmatism produced by progressively inhibited crustal assimilation. *Nature Communications*, 5.

Morse, S. (1984). Cation diffusion in plagioclase feldspar. *Science*, 225(4661):504–505.

Moune, S., Faure, F., Gauthier, P. J., and Sims, K. W. (2007). Pele's hairs and tears: Natural probe of volcanic plume. *Journal of Volcanology and Geothermal Research*, 164(4):244–253.

Nairn, I. A. (1979). RotomahanaWaimangu eruption, 1886: Base surge and basalt magma. *New Zealand Journal of Geology and Geophysics*, 22(3):363–378.

Nielson, D. L. and Sibbett, B. S. (1996). Geology of Ascension Island, South Atlantic Ocean. *Geothermics*, 25(4-5):427–448.

Papale, P. (1999). Strain-induced magma fragmentation in explosive eruptions. *Nature*, 397(6718):425–428.

Parfitt, E. A. (1998). A study of clast size distribution, ash deposition and fragmentation in a Hawaiian-style volcanic eruption. *Journal of Volcanology and Geothermal Research*, 84(3-4):197–208.

Patrick, M. R., Harris, A. J., Ripepe, M., Dehn, J., Rothery, D. A., and Calvari, S. (2007). Strombolian explosive styles and source conditions: Insights from thermal (FLIR) video. *Bulletin of Volcanology*, 69(7):769–784.

Paulick, H., Münker, C., and Schuth, S. (2010). The influence of small-scale mantle heterogeneities on Mid-Ocean Ridge volcanism: Evidence from the southern Mid-Atlantic Ridge (730'S to 1130'S) and Ascension Island. *Earth and Planetary Science Letters*, 296(3-4):299–310.

Porritt, L. A., Russell, J. K., and Quane, S. L. (2012). Pele's tears and spheres: Examples from Kilauea Iki. *Earth and Planetary Science Letters*, 333-334:171–180.

Preece, K., Mark, D. F., Barclay, J., Cohen, B. E., Chamberlain, K. J., Jowitt, C., Vye-Brown, C., Brown, R. J., and Hamilton, S. (2018). Bridging the gap: 40Ar/39Ar dating of volcanic eruptions from the 'Age of Discovery'. *Geology*, 46(12):1035–1038.

Ritcher, D. H., Eaton, J. P., Murata, K. J., Ault, W. U., and Krivoy, H. I. (1970). . Chronological narrative of the 1959-60 eruption of Kilauea Volcano, Hawaii. *U.S. Geol. Survey*, 150:73.

Rosseel, J. B., White, J. D., and Houghton, B. F. (2006). Complex bombs of phreatomagmatic eruptions: Role of agglomeration and welding in vents of the 1886 Rotomahana eruption, Tarawera, New Zealand. *Journal of Geophysical Research: Solid Earth*, 111(12):1–24.

Rothery, D. A., Sumner, J. M., Spieler, O., and Dingwell, D. B. (2007). Impact vesiculation ndash; a new trigger for volcanic bubble growth and degassing. *eEarth Discussions*, 2(4):151–167.

Ruprecht, P. and Bachmann, O. (2010). Pre-eruptive reheating during magma mixing at Quizapu volcano and the implications for the explosiveness of silicic arc volcanoes. *Geology*, 38(10):919–922.

Sable, J. E., Houghton, B. F., Del Carlo, P., and Coltelli, M. (2006). Changing conditions of magma ascent and fragmentation during the Etna 122 BC basaltic Plinian eruption: Evidence from clast microtextures. *Journal of Volcanology and Geothermal Research*, 158(3-4):333–354.

Schauroth, J., Wadsworth, F., Kennedy, B., von Aulock, F., Lavalle, Y., Damby, D., Vasseur, J., Scheu, B., and Dingwell, D. (2016). Conduit margin heating and deformation during the AD 1886 basaltic Plinian eruption at Tarawera volcano, New Zealand. *Bulletin of Volcanology*, 78(2):1–14.

Schmincke, H. (2004). *Volcanism*. Springer.

Schmincke, H. U. (1974). Volcanological aspects of peralkaline silicic welded ash-flow tuffs. *Bulletin Volcanologique*, 38(2):594–636.

Schumm, S. A. and Khan, H. R. (1972). Morphology and Petrography of Volcanic Ashes. *Geological Society of America Bulletin*, 83(7):1961.

Scott, D. and Stevenson, D. (1986). Magma ascent by porous flow. *Journal of Geophysical Research*, 91(5):9283–9296.

Sheppard, S. and Harris, C. (1985). Hydrogen and oxygen isotope geochemistry of Ascension Island lavas and granites: variation with crystal fractionation and interaction with sea water. *Contributions to Mineralogy and Petrology*, 91(1):74–81.

Shimozuru, D. (1994). Physical parameters governing the formation of Pele's hair and tears. *Bulletin of Volcanology*, 56(3):217–219.

Simmons, S. F., Keywood, M., Scott, B. J., and Keam, R. F. (1993). Irreversible change of the Rotomahana-Waimangu hydrothermal system (New Zealand) as a consequence of a volcanic eruption. *Geology*, 21(7):643–646.

Sparks, R. (1976). Journal of volcanology and geothermal research. *Physics of the Earth and Planetary Interiors*, 13(2):161.

Sparks, R. S. and Brazier, S. (1982). New evidence for degassing processes during explosive eruptions. *Nature*, 295(5846):218–220.

Sparks, S. and Huppert, H. (1984). Old magma chambers replenished by new ideas. *Nature (London)*, 312:1984.

Spera, F. J., Yuen, D. A., Greer, J. C., and Sewell, G. (1986). Dynamics of magma withdrawal from stratified magma chambers. *Geology*, 14(9):723–726.

Stasiuk, M. V., Barclay, J., Carroll, M. R., Jaupart, C., Ratté, J. C., Sparks, R. S., and Tait, S. R. (1996). Degassing during magma ascent in the Mule Creek vent (USA). *Bulletin of Volcanology*, 58(2-3):117–130.

Stovall, W. K., Houghton, B. F., Gonnermann, H., Fagents, S. A., and Swanson, D. A. (2011). Eruption dynamics of Hawaiian-style fountains: The case study of episode 1 of the Kilauea Iki 1959 eruption. *Bulletin of Volcanology*, 73(5):511–529.

Sumner, J. M., Blake, S., Matela, R. J., and Wolff, J. A. (2005). Spatter. *Journal of Volcanology and Geothermal Research*, 142(1-2):49–65.

Taddeucci, J., Edmonds, M., Houghton, B., James, M. R., and Vergniolle, S. (2015). *Hawaiian and Strombolian Eruptions.* Elsevier Inc., second edition.

Tait, S., Jaupart, C., and Vergniolle, S. (1989). Pressure, gas content and eruption periodicity of a shallow, crystallising magma chamber. *Earth and Planetary Science Letters*, 92(1):107–123.

Tuffen, H., Dingwell, B. D., and Pinkerton, H. (2003). Repeated fracture and healing of silicic magma generate flow banding and earthquakes? *Geology*, 31(12):1089–1092.

Tuffen, H. and Dingwell, D. (2005). Fault textures in volcanic conduits: Evidence for seismic trigger mechanisms during silicic eruptions. *Bulletin of Volcanology*, 67(4):370–387.

Turner, J. S. and Campbell, I. H. (1986). Convection and mixing in magma chambers. *Earth Science Reviews*, 23(4):255–352.

Valentine, G. A. and Connor, C. B. (2015). *Basaltic Volcanic Fields*. Elsevier Inc., second edition edition.

Valentine, G. A. and Gregg, T. K. (2008). Continental basaltic volcanoes - Processes and problems. *Journal of Volcanology and Geothermal Research*, 177(4):857–873.

Wadsworth, F. B., Vasseur, J., Scheu, B., Kendrick, J. E., Lavallée, Y., and Dingwell, D. B. (2016). Universal scaling of fluid permeability during volcanic welding and sediment diagenesis. *Geology*, 44(3):219–222.

Wadsworth, F. B., Vasseur, J., von Aulock, F. W., Hess, K.-U., Scheu, B., Lavalle, Y., and Dingwell, D. B. (2014). Nonisothermal viscous sintering of volcanic ash. *Journal of Geophysical Research: Solid Earth*, 119(12):8792–8804.

Walker, G. P. L. and Croasdale, R. (1971). Characteristics of some basaltic pyroclastics.

Wallace, P. J., Plank, T., Edmonds, M., and Hauri, H. (2015). *Volatiles in magmas*. Elsevier Inc., second edi edition.

Waters, L. and Lange, R. (2015). An updated calibration of the plagioclase-liquid hygrometer-thermometer applicable to basalts through rhyolites. *American Mineralogist*, 100(10):2172–2184.

Weaver, B., Kar, A., Davidsont, J. O. N., and Colucci, M. (1996). Geochemical characteristics of volcanic rocks from Ascension Island, South Atlantic Ocean. *Geothermics*, 25(4):449–470.

Wehrmann, H., Bonadonna, C., Freundt, A., Houghton, B. F., and Kutterolf, S. (2006). Fontana Tephra: A basaltic Plinian eruption in Nicaragua. *Special Paper of the Geological Society of America*, 412(412):209–223.

Weis, D. (1983). Pb isotopes in Ascension Island rocks: oceanic origin for the gabbroic to granitic plutonic xenoliths. *Earth and Planetary Science Letters*, 62(2):273–282.

Westrich, H. R. and Eichelberger, J. C. (1994). Gas transport and bubble collapse in rhyolitic magma: an experimental approach. *Bulletin of Volcanology*, 56(6-7):447–458.

Wysoczanski, R. and Tani, K. (2006). Spectroscopic FTIR imaging of water species in silicic volcanic glasses and melt inclusions: An example from the Izu-Bonin arc. *Journal of Volcanology and Geothermal Research*, 156(3-4):302–314.